Fakultät für Physik und Astronomie
Ruprecht-Karls-Universität Heidelberg

Master Thesis
in Physics

submitted by

Dorothea Fonnesu
from Villacidro - Sardinia (IT)

2016

Development and first tests of a new detector setup to study the de-excitation process of ^{163}Dy after electron capture in ^{163}Ho

This Master thesis was completed by Dorothea Fonnesu on

December 29, 2016

Kirchhoff-Institut für Physik

under the supervision of

J. Prof. Dr. L. Gastaldo

At a percent m_{ν_e} level, the present models still do not describe accurately the experimental ^{163}Ho electron capture calorimetric spectrum. Hence, different experiments to investigate the de-excitation processes in ^{163}Dy are needed. This thesis reports the study and experimental development of a new technique for the simultaneous and distinct measurement of the radiative (fluorescence, internal Bremsstrahlung) and non-radiative (Auger, Coster-Kronig transitions) components of the calorimetric energy spectrum of ^{163}Ho nuclear electron capture decay within the ECHo experiment. A 13-days long measurement of the partially calorimetric energy spectrum was performed via the read-out of an ^{163}Ho-implanted MMC pixel operated at 15 mK, which showed an activity of 0.5 Bq. An attempt to a radiative/non-radiative event coincidence measurement was made using, in addition to the implanted detector, the maXs-30, a 64 MMC pixel matrix designed to measure X-rays having energies up to 30 keV. The separate X-ray spectrum could not be measured due to the low-activity of the ^{163}Ho source, but the measurement of the spectrum of the embedded source proves the feasibility of such a measurement. The characterization of the spectrum shows the expected difference between the data and the full calorimetric spectrum predicted by the theory. Furthermore, due to very good detector resolution, the OII line is visible. Although the ^{163}Ho-implanted detector showed a satisfactory performance, a source with at least an activity of 10 Bq would be required for a successful coincidence measurement. However, the running of the whole experimental setup suggested this method is a promising way to investigate the radiative component of the ^{163}Ho calorimetric spectrum.

Entwicklung und erste Tests eines neuen Detektoraufbaus, um die Abregungsprozesse von ^{163}Dy nach Elektroneneinfang in ^{163}Ho zu untersuchen

In der vorliegenden Arbeit wurde im Rahmen des ECHo-Experiments der Elektron-Einfang-Prozess des Isotops ^{163}Ho hinsichtlich seiner radiativen (Röntgen-Floureszent und Interne Bremsstrahlung) und nicht-radiativen Anteile (Auger- und Coster-Kronig-Übergänge) hin untersucht. Hiefür wurde für 13 Tage das Spektrum der Energieeinträge in einem magnetischen Mikrokalorimeters aufgezeichnet, das bei 15 Milli-Kelvin betrieben wurde, und so an einer Oberfläche mit Atomen des Isotops ^{163}Ho mit einer Aktivität von 0.5 Bq implantiert war, dass nach jedem EC-Zerfall nur Fluoreszenzphotonen mit Energien zwischen 1.3 keV and 2 keV eine nennenswerte Wahrscheinlichkeit für ein Entkommen besitzen. Zusätzlich wurde versucht, die entkommenden Fluoreszezsphotonen mit einem großflächigen Detektor vom Typ maXs-30, einem 8x8-Pixel-Array von magnetischen Kalorimetern für den Nachweis von Photonen bis 30 keV, koinzident nachzuweisen. Im diskutierten Experiment konnte die prinzipielle Machbarkeit eines solchen Koinzidenz-Experiments gezeigt werden, wenn auch der koinzidente Nachweis entkommender Fluoreszenzphotonen wegen der geringen Rate, ausfallender maXs-30 Detektorkanäle und

schlechtem Signal-zu-Rauschen-Verhältnis nicht möglich war. Die Detektoren mit implantiertem ^{163}Ho zeigten im Gegensatz hierzu sehr gutes Signal-zu-Rauschen-Verhältnis. Ein Energieeintragsspektrum mit $\sim$ 50000 Ereignissen wird diskutiert. Zum ersten Mal konnte hierbei auch die niederenergetische OII-Linie mit einer Energie von nur 20 eV in einem kalorimetrischen Experiment beobachtet werden. Für eine zukünftige erfolgreiche Koinzidenzmessung sind eine ^{163}Ho-Aktivität von mehr als 10 Bq und eine größere Zahl gut funktionierender externer Röntgendetektorpixel empfehlenswert.

Contents

Introduction

Neutrinos are elementary particles and appear in the Standard Model (SM) of particle physics as the electrically neutral partners of the charged leptons e, μ and τ. Despite being included in the SM as massless particles, the discovery of their flavor oscillations by Super-Kamiokande [1] and SNO [2] collaborations implies a non-zero mass. This fact makes neutrinos a probe for new physics. However, if on one hand the observation of neutrino oscillations reveals their massive nature, on the other hand it does not provide any knowledge about the absolute scale of their masses, for which a different approach is needed. On this side, a lively research activity is in progress and focused on what are nowadays considered the most promising techniques to access information about neutrino masses: the study of the cosmic microwave background, large scale structures and type-Ia supernovae, the search for neutrinoless double-β-decay as well as neutrino time-of-flight measurements and the study of the kinematics of weak decays involving the emission of a neutrino, such as the β-decay or the nuclear electron capture (EC).

In particular, the study of the energy spectra of the β-decay and of the nuclear EC is considered a "model independent" method, as it allows a direct measurement of the effects related to a finite neutrino mass via the basic application of energy and momentum conservation. This effect is particularly evident when the energy of the emitted neutrino is minimal, as in this case, at the end-point region of the measured decay energy, the maximum value achieved would be reduced with respect to the Q-value by the energy needed to create the neutrino minus the neutrino mass.

The ECHo experiment will be performed in several phases. The first phase, ECHo-1k, is characterized by the use of 1 kBq ^{163}Ho source. Within one year of measuring time it will be possible to improve the present limit of the neutrino mass $m_\nu < 225\,\mathrm{eV}$ [3] by more than one order of magnitude. This experiment will be performed using ^{163}Ho-implanted metallic magnetic calorimeters (MMCs). The aim of ECHo-1k is also to prove the scalability of the whole experiment into its larger second phase, ECHo-1M, which would allow to reach a sensitivity to the electron neutrino mass in the sub-eV range

using a source activity of 1 MBq.
Among all the requirements needed to reach such a sensitivity, a precise understanding of the structures appearing in the calorimetrically measured spectrum of ^{163}Ho is of utmost importance. In fact, after EC occurs in ^{163}Ho, the daughter atom ^{163}Dy is left in an excited state and de-excites to its ground state via a number of radiative and non-radiative transitions, generating a spectrum which is the result of the measurement of all these contributions. An experiment in which the radiative and non-radiative components of the ^{163}Dy de-excitation spectrum can be measured (separately and simultaneously) could significantly help understanding the way these two components affect the energy spectrum.
This thesis is made in the context of the ECHo experiment and discusses for the first time a new experimental approach to study the decay modes of the excited ^{163}Dy. The method studied in this work is based on the synchronized measurement of the energy deposited in a suitable ^{163}Ho source (mainly Auger and Coster-Kronig electrons) and the energy escaping the detector (X-rays). A new experimental setup was designed and assembled. First experimental tests were performed showing the feasibility on such an experiment.
Chapter 1 gives an historical overview on neutrinos, and outlines the techniques for the measurement of their mass, with particular emphasis to the case of nuclear electron capture in ^{163}Ho. Chapter 2 introduces the ECHo experiment and gives an overview of the theoretical and experimental challenges. A summary of the measurements of the X-ray spectrum performed in the past by other collaborations is also given here, followed by an introduction to the measurement principle studied and developed within this work. Chapter 4 describes the first experimental tests. As source, 4 implanted MMC pixels with ^{163}Ho present at the surface were used. As a large area detector a 8×8 pixel array MaXs-30 [4], covering a $4 \times 4\,\mathrm{mm}^2$ surface, was positioned in a way that the source was located at a distance of 1.2 mm and in correspondence to the center of the 2D array. For this thesis a 13-day long data acquisition was performed during which one of the source pixels was characterized. A very precise spectrum showing an energy resolution of the line NI $\Delta E_{FWHM} = 9\,\mathrm{eV}$ was required. For the first time the line OII was resolved in a calorimetric measurement. Since not all the energy released in the detector could be stopped, a study of the deviations of the spectrum with respect to a fully calorimetric measurement was performed. Finally, a summary of the results and some indications for the future experiments are given in the Conclusions.

Chapter 1

Introduction to neutrinos

1.1 Historical overview

Neutrinos are elementary particles of the Standard Model of fundamental interactions. They are neutral fermions with half-integer spin, obey the Fermi-Dirac statistics and interact only via weak interaction and gravity. Since they have been theorised for the first time, the study of neutrinos represented one of the most challenging and engaging fields of fundamental physics. In fact, due to their low mass and neutral charge, neutrinos usually travel through matter undetected and unimpeded.

The existence of neutrinos was proposed in 1930 for the first time by W. Pauli, in an open letter to his colleagues who were attending a physics conference in Tübingen. He discussed a still not completely developed idea about the existence of an electrically neutral and weakly interacting fermion, whose mass could be in the order of the one of the electron or smaller, which could have solved the issues with the not expected continuous spectrum in β-decay [5]. He named this particle *neutron*. It was later in 1932, when the neutron as we know it nowadays was discovered by J. Chadwick [6], that Fermi renamed as *neutrino* the particle proposed by Pauli. After one year, in 1933, Fermi [7] and Perrin [8] argued, one independently from the other, that neutrinos could be massless.

In the following years, a QED-like theory of the weak interactions was developed starting from the Fermi theory of the β-decay [9, 10]. Only in 1956, with the observation of the anti-neutrino, the first detection of neutrinos was achieved [11]. The existence of three neutrino families was only proved experimentally later in 1989 at LEP by the ALEPH collaboration at CERN [12], when the building blocks of the SM with three generations were completed. The effort to describe the weak interaction culminated with the formulation

of the Glashow-Weinberg-Salam Standard Model (SM) [13, 14] in 1967, based on an $SU(2) \times U(1)$ model, which predicted the existence of weak neutral currents and the Z-boson, and enclosed the *Higgs mechanism* for mass generation discovered in 1964 by P. W. Higgs [15], F. Englert and R. Brout [16]. In 2015 T. Kajita from the Super-Kamiokande collaboration and A. B. McDonald from the SNO collaboration were awarded the Nobel prize *"for the discovery of neutrinos oscillations, which shows that neutrinos have mass"*.

1.2 Neutrinos and the Standard Model

Thanks to neutrino oscillations, we know that neutrinos are massive and flavour-mixed, even though this is not expected in the SM framework. Neutrinos can then be considered as an open passage leading from the well effective yet incomplete SM theory to the new physics beyond the SM which would possibly explain their masses and mixing mechanism.
In 1998 the Super-Kamiokande experiment clearly showed the effect of neutrino flavor oscillations by measuring neutrinos created in the Earth's atmosphere by the interaction of cosmic rays with the atmosphere itself [17]. Neutrino oscillations were also the solution to the so called *solar neutrino problem*, for which the detected solar neutrino flux was smaller than the one predicted by the solar models [18]. The SNO experiment demonstrated that the measured total solar neutrino flux was indeed the expected one and that about 1/3 of just the electron neutrino component was missing. Differently from the previous experiments, which were only capable of the detection of electron neutrinos, SNO could instead detect all three types of neutrinos and electron neutrinos separately, and showed that a strong component of non-e-flavored neutrinos appeared in the flux [19, 20]. The explanation for this event was found in the fact that neutrinos can change flavor in their travel from the Sun to the Earth, this happening inside the Sun because of the Mikheev-Smirnov-Wolfenstein (MSW) resonance conversion effect [21, 22, 23].

1.2.1 Massive neutrinos

The main assumption is that the 3 orthogonal neutrino flavor (or weakly interacting) eigenstates ν_α included in the SM[1], with $\alpha = e, \mu, \tau$, do not

[1] A variety of models which take into account a larger number of possible eigenstates currently exist. Several anomalies in the measurement of reactor neutrinos fluxes and long-baseline experiments pointed out the possible existence of sterile neutrinos in the eV scale, while the observations of matter distribution in the Universe might require for the

correspond to the orthogonal neutrino mass eigenstates ν_i, with $i = 1, 2, 3$, but they are related through a unitary matrix U which, in Natural Units ($\hbar = c = 1$), has the expression:

$$|\nu_\alpha\rangle = \sum_i \mathrm{U}_{\alpha i} \, |\nu_i\rangle \, . \tag{1.1}$$

The U matrix contains the fundamental parameters of neutrino mixing, and reads explicitly:

$$\begin{aligned} \mathrm{U} = & \begin{bmatrix} c_{12}c_{13} & s_{12}c_{13} & s_{13}e^{-i\delta} \\ -s_{12}c_{23} - c_{12}s_{23}s_{13}e^{i\delta} & c_{12}c_{23} - s_{12}s_{23}s_{13}e^{i\delta} & s_{23}c_{13} \\ s_{12}s_{23} - c_{12}c_{23}s_{13}e^{i\delta} & -c_{12}s_{23} - s_{12}c_{23}s_{13}e^{i\delta} & c_{23}c_{13} \end{bmatrix} \\ & \times \mathrm{diag}\left(1, e^{i\frac{\alpha_{21}}{2}}, e^{i\frac{\alpha_{31}}{2}}\right) \end{aligned} \tag{1.2}$$

where $c_{ij} = \cos\theta_{ij}$, $s_{ij} = \sin\theta_{ij}$, $\theta_{ij} = [0,\pi/2]$, $\delta = [0,2\pi]$ is the Dirac CP-violating phase while α_{21}, α_{31} are the Majorana CP-violating phases, only present if neutrinos are Majorana particles.
Schrödinger's equation gives the time evolution of the state $|\nu_\alpha\rangle$:

$$|\nu_\alpha(x,t)\rangle = \sum_i \mathrm{U}_{\alpha i} \, \mathrm{e}^{i\mathrm{p}_i x} \, \mathrm{e}^{-i\mathrm{E}_i t} \, |\nu_i\rangle \tag{1.3}$$

where x, p_i and E_i are the position, momentum and energy of the neutrino respectively. Assuming a relativistic energy

$$\mathrm{E}_i = \sqrt{\mathrm{m}_i^2 + \mathrm{p}_i^2} \simeq \mathrm{p}_i + \frac{\mathrm{m}_i^2}{2\mathrm{p}_i} \simeq \mathrm{E} + \frac{\mathrm{m}_i^2}{2\mathrm{E}}, \tag{1.4}$$

a neutrino emitted at $x = 0$ and using the inverse of eq. 1.1, for $\mathrm{p}_i >> \mathrm{m}_i$ and so $\mathrm{E} \approx \mathrm{p}_i$ as neutrino energy, and defining $\mathrm{L} = x = t$ as the distance between the neutrino source and the detector, eq. 1.3 becomes:

$$\begin{aligned} |\nu_\alpha(x,t)\rangle &= \sum_{i,\beta} \mathrm{U}_{\alpha i} \, \mathrm{U}^*_{\beta i} \, \mathrm{e}^{i\mathrm{p}_i x} \, \mathrm{e}^{-i\mathrm{E}_i t} \, |\nu_\beta\rangle \\ &= \sum_{i,\beta} \mathrm{U}_{\alpha i} \, \mathrm{U}^*_{\beta i} \, \mathrm{e}^{-i\frac{\mathrm{m}_i^2}{2}\frac{\mathrm{L}}{\mathrm{E}}} \, |\nu_\beta\rangle \, . \end{aligned} \tag{1.5}$$

existence of warm dark matter, for which a good candidate would be a keV-scale sterile neutrino. Sterile neutrinos could be included in the minimal extension of the SM [24, 25].

It is possible now to calculate the probability for the transition from the state ν_α to the state ν_β:

$$\begin{aligned} \mathrm{P}(\alpha \to \beta) &= |\, \langle \nu_\beta | \nu_\alpha(x,t) \rangle \,|^2 \\ &= \sum_i \sum_j \mathrm{U}_{\alpha i}\, \mathrm{U}^*_{\alpha j}\, \mathrm{U}^*_{\beta i}\, \mathrm{U}_{\beta j} \exp\left(-i \frac{\Delta \mathrm{m}^2_{ij}}{2} \frac{\mathrm{L}}{\mathrm{E}} \right), \end{aligned} \tag{1.6}$$

which shows that the probability for a neutrino in the state α to undergo a transition into the flavor state β does not only depend on its energy E and traveled distance L, but also on the squared mass difference $\Delta \mathrm{m}^2_{ij}$ between the two eigenstates i,j and the corresponding matrix elements. Therefore, for the neutrino oscillation to be possible, it must be $\Delta \mathrm{m}^2_{ij} \neq 0$ for at least one of the possible i,j combinations, which means that only one neutrino can be massless.
Table 1.1 shows the current best-fit values for the 3-neutrino oscillation parameters, based on a global fit of the current neutrino oscillation data [26]. The values (in brackets) correspond to the mass ordering $\mathrm{m}_1 < \mathrm{m}_2 < \mathrm{m}_3$ ($\mathrm{m}_3 < \mathrm{m}_1 < \mathrm{m}_2$). The definition used for $\Delta \mathrm{m}^2$ is $\mathrm{m}^2_3 - (\mathrm{m}^2_2 + \mathrm{m}^2_1)/2$, thus

$$\Delta \mathrm{m}^2 = \begin{cases} \Delta \mathrm{m}^2_{31} - \frac{\Delta \mathrm{m}^2_{21}}{2} > 0 & \text{if} \mathrm{m}_1 < \mathrm{m}_2 < \mathrm{m}_3 \\ \Delta \mathrm{m}^2_{32} + \frac{\Delta \mathrm{m}^2_{21}}{2} < 0 & \text{if} \mathrm{m}_3 < \mathrm{m}_1 < \mathrm{m}_2 \end{cases} \tag{1.7}$$

Parameter	**Best fit**	**3σ**
$\Delta \mathrm{m}^2_{21}$ $[10^{-5}\,\mathrm{eV}^2]$	7.50	7.03 - 8.09
$\Delta \mathrm{m}^2_{3l}$ $[10^{-3}\,\mathrm{eV}^2]$	2.524	2.407 - 2.643
$\sin^2\theta_{12}$	0.306	0.271 - 0.345
$\sin^2\theta_{23}$	0.441	0.385 - 0.635
$\sin^2\theta_{13}$	0.02166	0.01934 - 0.02392
δ	261	0 - 360

Table 1.1: The best-fit values of the 3-neutrino oscillation parameters [27] for the normal mass ordering.

The determination of the nature of massive neutrinos (whether they are Dirac or Majorana particles), the "neutrino mass ordering" (i. e. understanding the sign of $\Delta \mathrm{m}^2_{31}$ or of $\Delta \mathrm{m}^2_{32}$), understanding their mass spectrum (is there a precise hierarchy? are they quasi-degenerate?), determining the status of CP violation in the lepton sector and many other aspects are still open investigation fields for the future.

The experimental observation of neutrino oscillations revealed that neutrinos have masses. So far though, it is not possible to argue about the absolute scale of their mass. Nevertheless, many experimental efforts were and still are made in order to clarify the fundamental features of the neutrino mass spectrum.
In the following, the different approaches employed up to now are discussed.

1.2.2 Cosmology

As far as we understand, neutrinos played an important role in the development of the Universe the way we know it today. For example, the number of neutrino families influenced the element composition of the Universe through the primordial nucleosynthesis [28], and later, massive neutrinos were involved in the formation of large-scale structures (LSS) in the form of hot dark matter. Anisotropies of the cosmic microwave background (CMB) are also a probe for neutrino physics and can provide a constraint on the sum of neutrino masses, defined as:

$$\mathrm{m}_{tot} = \sum_{\nu} \mathrm{m}_{\nu} \ . \tag{1.8}$$

In fact, neutrinos in the low mass range (< 1 MeV) can contribute to m_{tot} through the total energy density of the Universe, given by:

$$\rho_{\nu} = \mathrm{m}_{tot}\, \mathrm{n}_{\nu} = \frac{3}{11} \mathrm{m}_{tot}\, \mathrm{n}_{\gamma} \tag{1.9}$$

where the factor 3/11 gives the ratio of neutrino to photon number. Using the critical energy density of the Universe ρ_c and a photon number density of $\mathrm{n}_{\gamma} = 412\,\mathrm{cm}^{-3}$ we get:

$$\Omega_{\nu} h^2 = \frac{\rho_{\nu}}{\rho_c} = \frac{\mathrm{m}_{tot}}{94\,\mathrm{eV}}, \tag{1.10}$$

therefore an upper limit of $\Omega_{\nu} h^2 < 0.12$ for the matter density would constrain the sum of the neutrino masses to $\mathrm{m}_{tot} < 11$ eV [29]. A much more stringent limit is obtained through the combination of the observations of the CMB, LSS, distant type-Ia supernovae and a precise determination of the Hubble constant, which leads to an upper limit of [30]:

$$\mathrm{m}_{tot} < 0.23\,\mathrm{eV}. \tag{1.11}$$

1.2.3 Neutrinoless double beta-decay - $0\nu\beta\beta$

When an atomic nucleus decays via double β-decay, two of its neutrons simultaneously transform into two protons emitting two electrons and two electron antineutrinos. This process, as the single β-decay, usually takes place in order for the involved atom to get closer to a more stable neutron/proton ratio configuration, and when the latter is energetically forbidden. The outlined reaction is:

$$ {}^{\mathrm{A}}_{\mathrm{Z}}\mathrm{X} \rightarrow {}^{\mathrm{A}}_{\mathrm{Z+2}}\mathrm{X} + 2e^- + 2\bar{\nu}_e. \tag{1.12} $$

Examples of isotopes for which double β-decay with emission of two antineutrinos was observed are ^{48}Ca, ^{76}Ge, ^{100}Mo and ^{136}Xe, all of them having a half-life in the order of $\sim 10^{21}$y.
However, if neutrinos are their own antiparticles, as first suggested by Majorana [31], the process in eq. 1.12 can in principle happen via the exchange of a virtual neutrino, and thus without the emission of the two neutrinos. A typical spectrum for the sum of the energies of each of the two electrons is shown in fig. 1.1. The black line shows the spectrum resulting from $2\nu\beta\beta$-decay events, in which the energy available for the decay was shared between the emitted electrons and antineutrinos, which has a continuous trend up to the end-point energy $\mathrm{Q}_{\beta\beta}$ and a maximum at approximately $\mathrm{Q}_{\beta\beta}/3$. The red peak is given by the $0\nu\beta\beta$ events in which only electrons are emitted and therefore the carry the full energy $\mathrm{Q}_{\beta\beta}$ available for the process.
Apart from demonstrating that neutrinos are Majorana particles, the observation of the $0\nu\beta\beta$-decay would also allow the measurement of the Majorana mass $\langle \mathrm{m}_{\beta\beta} \rangle = |\sum_i \mathrm{U}^2_{ei}\, \mathrm{m}_i|$. This can be obtained by measuring the half-life life of the decay and thus its decay rate $\Gamma^{0\nu\beta\beta}$, given by:

$$ \Gamma^{0\nu\beta\beta} = \mathrm{G}^{0\nu\beta\beta}(\mathrm{Q}_{\beta\beta},\mathrm{Z})\, |\mathrm{M}^{0\nu\beta\beta}|^2\, \frac{\langle \mathrm{m}_{\beta\beta} \rangle}{\mathrm{m}_e^2}, \tag{1.13} $$

where m_i are the neutrino mass eigenstates, m_e is the electron mass, $\mathrm{G}^{0\nu\beta\beta}$ is the integral over the phase space of the two emitted electrons and $\mathrm{M}^{0\nu\beta\beta}$ are the nuclear matrix elements. The last ones are strongly model dependent and provide the largest uncertainty in the calculation of $\langle \mathrm{m}_{\beta\beta} \rangle$.
Presently no experiment succeeded at identifying $0\nu\beta\beta$ events, thus only upper limits for the half-life and $\mathrm{m}_{\beta\beta}$ were obtained so far. To mention the most recent results in this field, in August 2016 the KamLAND-Zen Collaboration published the results [32] of their last analysis on the search of $0\nu\beta\beta$-decay with ^{136}Xe, according to which the upper limits on the effective

Majorana neutrino mass are in the range

$$\langle m_{\beta\beta} \rangle \leq (61 - 165)\,\text{meV}. \tag{1.14}$$

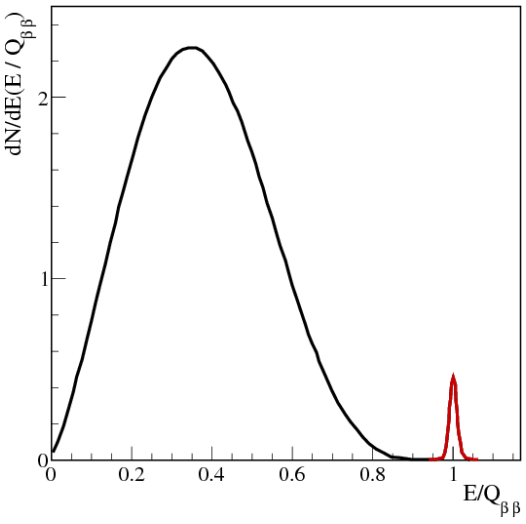

Figure 1.1: Typical energy spectrum of double β-decay. In black are shown the events in which both electrons and antineutrinos are emitted. The red peak at the end-point energy $Q_{\beta\beta}$ represents the events without emission of neutrinos. Picture source: [33].

1.2.4 Direct mass measurements

Even though they provide significant knowledge about the mass and the mass spectrum of neutrinos, the methods involving $0\nu\beta\beta$-decay and cosmological investigations, mentioned in sec. 1.2.3 and sec. 1.2.2 respectively, strongly depend on theoretical models and assumptions implemented in the analysis of the data. To have access to a more model independent measurement of the neutrino mass, in fact, it is necessary to investigate the kinematics of processes in which neutrinos are involved. In the following sections, experimental techniques concerning the measurement of the time-of-flight of neutrinos and nuclear weak decays involving the emission of neutrinos are discussed.

Time-of-Flight measurements

As a consequence of the fact that neutrinos have mass, they cannot travel at the speed of light c. This means that the distance "d" covered by a photon in a time $t_\gamma = d/c$ is traveled by neutrinos in a time $t_\nu < t_\gamma$. Based on this simple principle, one can infer the neutrino mass by observing their difference in time-of-flight with photons coming from the same source. Since the neutrino masses are very small, the detectable difference would also be very small, so that one needs to dramatically increase the sensitivity by a

careful combination of a strong neutrino source placed at a long distance and suitable detectors.
Cosmological sources as core-collapse supernovae suit this purpose. In fact, from the detection of neutrinos produced in SN1987A in the Large Magellanic Cloud it was possible to set un upper limit [34] of

$$\mathrm{m}_\nu < 5.8\,\mathrm{eV}\,(95\%\,\mathrm{C.\,L.}) \tag{1.15}$$

for the neutrino mass. Long baseline experiments on Earth might be also suitable for time-of-flight measurements, but in this case the achievable sensitivity is rather lowered by the much shorter traveled distance and because of the smaller intensity of the source. Nowadays neutrinos from supernovae seem to be the only reasonable way to perform studies on the neutrino mass, even though they are still strongly limited by the precision of the models describing supernovae explosions.

Nuclear β-decay
The β-decay of an atomic nucleus is a process driven by the weak interaction for which a neutron transforms into a proton via the emission of an electron and an electron antineutrino[2], according to the reaction:

$${}^{\mathrm{A}}_{\mathrm{Z}}\mathrm{X} \rightarrow {}^{\mathrm{A}}_{\mathrm{Z-1}}\mathrm{X} + e^- + \bar{\nu}_e. \tag{1.16}$$

The total energy Q_β released in the decay can range from a few keV up to tens of MeV depending on the nuclide, and is usually almost completely shared between the electron and the antineutrino, as the nucleus is too massive with respect to the emitted particles and its recoil energy can be neglected. Thus, a non-zero neutrino mass can be measured as missing energy in the experimentally measured spectrum of the decay, when this is compared to the expected spectrum one would obtain in case of massless neutrinos.
The energy spectrum of β-decay is given by the Fermi's golden rule, as follows[3]:

$$\frac{\mathrm{dN}^2}{\mathrm{d}t\mathrm{dE}_e} = \mathrm{a\,F\,p}_e\,(\mathrm{E}_e + \mathrm{m}_e)(\mathrm{Q}_\beta - \mathrm{E}_e)\sum_i |\mathrm{U}_{ei}|^2\sqrt{(\mathrm{Q}_\beta - \mathrm{E}_e)^2 - \mathrm{m}^2_{\nu_i}} \tag{1.17}$$

$$\text{with} \quad \mathrm{a} = \frac{\mathrm{G}_F^2\cos^2\theta_\mathrm{C}}{2\pi^3}|\mathrm{M}_{had}|^2 \quad \text{and} \quad \mathrm{F} = \mathrm{F}(\mathrm{E}_e,\mathrm{Z}+1), \tag{1.18}$$

[2]The β^+ decay can also occur, in which a proton transforms into a neutron via the emission of a positron and an electron neutrino.
[3]A detailed calculation is given in [35].

where p_e, E_e and m_e are the momentum, energy and mass of the emitted electron, U_{ei} are the neutrino mixing matrix elements and m_{ν_i} is the i-th neutrino mass eigenstate. The factor "a" contains the Fermi constant G_F^2, the Cabibbo angle θ_C and the nuclear matrix element M_{had}. The Fermi function F depends on the energy of the electron and the nuclear charge, and takes into account the Coulomb interaction between the emitted electron and the daughter nucleus.
Using the unitarity of the neutrino mixing matrix and defining an averaged electron antineutrino mass as the incoherent mixing of the three mass eigenstates (i. e. $m_{\bar{\nu}_e} = \sum_i |U_{ei}| m_{\nu_i}$), in case $(Q_\beta - E_e) >> m_{\nu_i}$ it is possible to apply the approximation

$$(Q_\beta - E_e) \sum_i |U_{ei}|^2 \sqrt{(Q_\beta - E_e)^2 - m_{\nu_i}^2} \approx (Q_\beta - E_e)^2 - m_{\bar{\nu}_e}^2, \qquad (1.19)$$

from which it can be seen how the effect of a non-zero neutrino mass would more strongly affect the energy region of the spectrum close to Q_β (since $(Q_\beta - E_e)^2 \approx m_{\bar{\nu}_e}^2$). For this reason, most of the experimental efforts are made with the aim of resolving the end-point of the energy spectrum, which usually covers a range of $10 - 10^2$ eV below Q_β.
In order to select the most suitable nuclide to study the effects on the β-spectrum of a finite neutrino mass, two parameters need to be considered: the decay half-life $\tau_{1/2}$ and the decay Q-value Q_β. The half-life determines the needed amount of material source to be used and also reflects the kind of transitions the nuclide undergoes, from super-allowed to third-order forbidden transitions, which in turn affect the shape of the energy spectrum. Moreover, eq. 1.17 shows that the number of events in the region of interest scales with Q_β^{-3}, which means the choice of a low Q_β is preferable.
The experiments Mainz and Troitsk, studying the β-decay of molecular tritium ($^3H_2$), could set the presently most stringent limits on the electron antineutrino mass [36, 37], given by:

$$m_{\bar{\nu}_e} \leq 2.3\,\text{eV}\,(95\%\,\text{C. L.}) \qquad m_{\bar{\nu}_e} \leq 2.12\,\text{eV}\,(95\%\,\text{C. L.}). \qquad (1.20)$$

The two groups joined the efforts for the next generation experiment KATRIN (the KArlsruhe TRItium Neutrino experiment), a new international collaboration with the aim of setting a new upper limit for the electron antineutrino mass down to 0.2 eV (90% C. L.) [38].

Nuclear electron capture

Electron capture (EC), sometimes also called "inverse β-decay", typically takes place in proton rich nuclides where one electron in the inner shells of an atom is captured by the nucleus, causing a proton to turn into a neutron with the simultaneous emission of an electron neutrino. Nuclear EC, like β-decay, is also due to weak interaction. The reaction for the process is

$$\begin{aligned} {}^{\mathrm{A}}_{\mathrm{Z}}\mathrm{X} &\rightarrow {}_{\mathrm{Z}-1}{}^{\mathrm{A}}\mathrm{X}^{*} + \nu_e \\ &\rightarrow {}_{\mathrm{Z}-1}{}^{\mathrm{A}}\mathrm{X} + \mathrm{E}_{EC}\,. \end{aligned} \tag{1.21}$$

After the EC, the daughter atom is left in an excited state. The energy Q_{EC} released in the decay is shared between the excited atom and the emitted neutrino. Therefore, if the Q_{EC} of the decay is precisely known, measuring the de-excitation energy E_{EC} released by the excited daughter atom when decaying to its ground state allows to gain information about the energy of the escaped neutrino.

The de-excitation of the daughter atom happens through a number of transitions following the EC which can be of two types: radiative and non-radiative transitions. The energy E_{EC} is given by the sum of the energies of all these transitions.

In the radiative transitions, the hole left in the atomic shell by the captured electron, at an energy E_h (compared to the continuum energy), is filled by an electron coming from one of the outer shells and having energy E_1. The energy of the transition is emitted in the form of an X-ray photon having, in fact, an energy $\mathrm{E}_\gamma = \mathrm{E}_h - \mathrm{E}_1$. However, it can also happen that a photon is emitted by the electron when this is accelerated in the Coulomb field of the atomic nucleus during the capture. This phenomenon, called Internal Bremsstrahlung (IB), takes a role in the radiative component of the de-excitation energy spectrum.

Non-radiative transitions are, instead, usually characterized by the emission of Auger electrons. When an outer electron having an energy E_1 fills the hole left after EC, the transition energy is employed for the emission of a more weakly bound electron (that is an electron having an energy $\mathrm{E}_2 < \mathrm{E}_1$), which in turn takes a kinetic energy $\mathrm{E}_e = \mathrm{E}_h - \mathrm{E}_1 - \mathrm{E}_2$. When the electron which filled the hole comes from the same shell where the hole is (but different sub-shell), the Auger transition takes the name of Coster-Kronig transition, and, in the even more special case in which the emitted electron also belongs to the same shell one has a so called super-Coster-Kronig transition. Apart from this last one, the de-excitation transitions mentioned so far have been outlined in fig. 1.2.

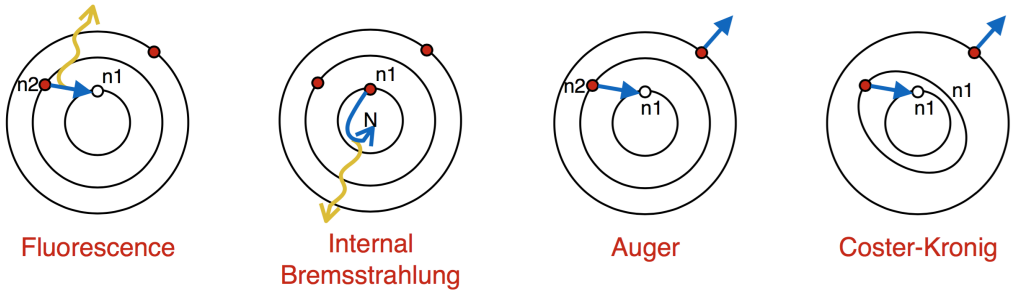

Figure 1.2: Diagram of the main possible channels via which the de-excitation of the daughter atom can take place, after the mother atom underwent electron capture. In the radiative processes (fluorescence and internal Bremsstrahlung) the yellow wavy arrow represents an emitted photon, and the hole left by the captured electron is depicted as a small, empty circle, even in the diagrams for the non-radiative processes (Auger and Coster-Kronig). The n_i indicate the involved electronic shells, and the atomic nucleus is indicated by a "N". This picture is inspired to fig. 10 in [39].

Due to these different processes, the de-excitation spectrum following EC can be measured using different techniques. Both X-rays and Auger electrons emitted by an EC source can be separately detected with standard spectroscopy methods for electrons and X-rays respectively. The main disadvantage in this case is represented by the impossibility of simultaneously detecting the whole emitted energy. The interpretation of such spectra would require a precise knowledge of the branching ratios into the different channels[4] and a precise estimation of self-absorption of the emitted radiation in the source. In 1982 A. De Rujúla and M. Lusignoli proposed to perform a calorimetric measurement of the ^{163}Ho EC spectrum in order to gain sensitivity with respect to the electron neutrino mass [41]. In fact, in such measurements the complete energy released in the de-excitation process of the daughter atom as well as the recoil of the nucleus can be measured. Besides the fact that this method removes the uncertainties due to a not precise knowledge of the radiative/non-radiative de-excitation branching ratio and to self-absorption in the source, the obtained spectrum is complementary to the ν_e spectrum and therefore can be interpreted via the conservation of energy.
In [41] the authors, considering only first order excitations where the daughter atom is left with a hole in h, present the spectral shape as a sum of Breit-

[4]The e/γ branching ratios for the M-lines for the elements ranging from calcium (Z = 20) to thorium (Z = 90) and undergoing atomic de-excitations via fluorescence and Auger/Coster-Kronig transitions are given in [40].

Wigner shaped resonances modulated by the phase-space factor[5]:

$$\begin{aligned}\frac{\mathrm{d}\Gamma}{\mathrm{dE}_{EC}} &= \kappa\,(\mathrm{Q}_{EC}-\mathrm{E}_{EC})\,\sqrt{(\mathrm{Q}_{EC}-\mathrm{E}_{EC})^2-\mathrm{m}^2_{\nu_e}} \\ &\times\sum_h \mathrm{B}_h\,\phi^2_h(0)\,\frac{\Gamma_h}{2\pi}\,\frac{1}{(\mathrm{E}_{EC}-\mathrm{E}_h)^2+\frac{\Gamma^2_h}{4}},\end{aligned} \tag{1.22}$$

From eq. 1.22 one can see that the energies of the electronic levels h of the decaying atom are centered at E_h and have natural width Γ_h for an excited atomic state in the daughter atom having a hole in h. The sum runs over the possible states from which an electron can be captured. The amplitude of the resonance is given by $\mathrm{B}_h\,\phi^2_h(0)$, where $\phi^2_h(0)$ is the squared wave function of the captured electron calculated at the nucleus position and B_h is the atomic exchange and overlap correction. The multiplicative constant κ contains the squared nuclear matrix elements and the Fermi coupling strength. The neutrino mass $\mathrm{m}_{\nu_\mathrm{e}}$ enters the decay rate in the neutrino phase space factor preceding the decay resonances, so that a non-zero mass mostly affects the end point of the spectrum, as already discussed for the case of β-decay. For similar reasons, the lower Q_{EC} the more sensitive the spectrum is to the neutrino missing energy. Furthermore, the resonance regions in the spectrum around the energies E_h contain indeed a larger number of counts, and in case the condition $\mathrm{E}_h \sim \mathrm{Q}_{EC}$ is verified this would imply a large number of counts in the region of interest just below the end-point of the spectrum. However, a nuclide with such a property has not been found yet.

Presently, the best candidate to be used in experiments aiming at measuring the electron neutrino mass via the study of the energy spectrum of its EC decay is ^{163}Ho, with a half-life [42] of

$$\tau^{\mathrm{Ho}}_{1/2} = 4570 \pm 50\,\mathrm{y} \tag{1.23}$$

and a Q-value [43] of

$$\mathrm{Q}_{EC} = (2.833 \pm 0.030^{\mathrm{stat}} \pm 0.015^{\mathrm{syst}})\,\mathrm{keV}, \tag{1.24}$$

which is the lowest among the nuclides undergoing electron capture.

[5]Here the notation and structure of the formula were slightly changed from the original ones in [41], for sake of consistency with the other contents. Also, the factor B_h was included in the theoretical expression for the spectrum only later.

1.2.5 Electron capture in ^{163}Ho

In this section the electron capture in ^{163}Ho is discussed, with a focus on the features of the energy spectrum which can mainly affect the sensitivity on the measurement of the electron neutrino mass.
As already mentioned in sec. 1.2.4, after the EC occurs, the daughter atom is left in an excited state and de-excites to its ground state via a number of radiative and/or non-radiative transitions. In the specific case of ^{163}Ho the process is described as:

$$\begin{aligned} {}^{163}_{67}\mathrm{Ho} &\rightarrow {}^{163}_{66}\mathrm{Dy}^{*} + \nu_e \\ &\rightarrow {}^{163}_{66}\mathrm{Dy} + \mathrm{E}_{EC} \end{aligned} \tag{1.25}$$

where the nuclear spin transition is given by ^{163}Ho$(7/2)^-$ to ^{163}Dy$(5/2)^-$. Because of its low Q-value, only the electrons belonging to the MI shell and outer ones can be captured and, according to the selection rules for the angular momentum, the electrons having a total angular momentum $j \geq 3/2$ cannot be captured. A list of the transitions which fulfill the energy and momentum conservation requirements is given in tab. 1.2.

Line h	**Rel. amplitude**	$\mathbf{B}_h$	$\mathbf{\Gamma}_h$ [eV]	$\mathbf{E}_h$ [eV]
MI	1	1.083	13.2	2046.9
MII	0.0526	1.031	6.0	1844.6
NI	0.233	1.151	5.4	420.4
NII	0.0119	1.108	5.3	340.6
OI	0.0345	1.248	3.7	49.9
OII	0.0115	1.224	-	26.3
PI	0.0021	-	-	-

Table 1.2: Spectral lines of ^{163}Dy following EC in ^{163}Ho , listed with their properties. The relative amplitude of the lines is normalized to the MI-line amplitude. B_h are the atomic exchange and overlap corrections, Γ_h the line widths and E_h the line energies. The X-ray notation (K, L, M, ...) is used, where e. g. the MI-line corresponds to the $^3\mathrm{S}_{1/2}$ level in spectroscopic notation.

The spectral shape for ^{163}Ho according to eq. 1.22 is shown in fig. 1.3, along with a zoom of the end-point of the spectrum showing how the shape for a massless neutrino differs from the shape calculated for a neutrino having mass of $\mathrm{m}_\nu = 10$ eV.
This spectrum was calculated using the parameters given in [44], obtained using a fully-relativistic approach for the calculation of the electron wave

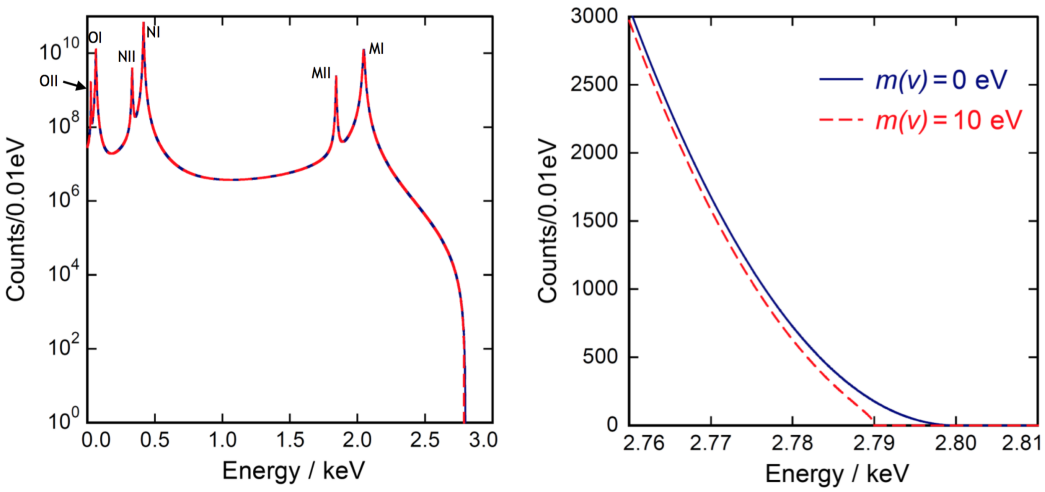

Figure 1.3: The calorimetric spectrum of ^{163}Ho electron capture decay. The full plot on the left shows the electronic resonances down to the OII-line. The plot to the right, instead, shows a zoom on the end-point of the spectrum, where it can be seen how a non-zero neutrino mass would affect the count rate in this region. A "large" neutrino mass of $m_\nu = 10$ eV was chosen intentionally, to enhance the visual effect.

functions of the electrons of the parent ^{163}Ho and daughter ^{163}Dy atoms. Currently the spectrum does not describe the data completely, as one can see from figure 1.4, where a comparison of experimental data (black line), first- (blue dashed line) and second-order theory by Fässler (pink line) in the NI region is shown.

An important aspect which still needs to be better understood, as pointed out for the first time by Robertson [45], is the contribution to the energy spectrum of the so called *shake-up* and *shake-off* processes, i.e. those events in which the capture of the electron in the nucleus causes the shake-up of another electron into an unoccupied higher level in the daughter atom (*shake-up*) or into the continuum (*shake-off*), due to the fact that the wave functions of the spectator electrons in the mother and daughter atom are not identical. At the moment, two main theories are being developed on this side, namely the studies by De Rujúla and Lusignoli [46] and the ones by Fässler and Šmikovic [44]. In both cases, the phenomenon is addressed as "two-hole contribution" to the EC energy spectrum, as in both shake-up and shake-off a second hole is created in addition to the one coming from the electron capture.

On one hand, according to De Rujúla, the two-hole contributions in the EC decay of ^{163}Ho are expected to enhance the sensitivity at the end-point of the

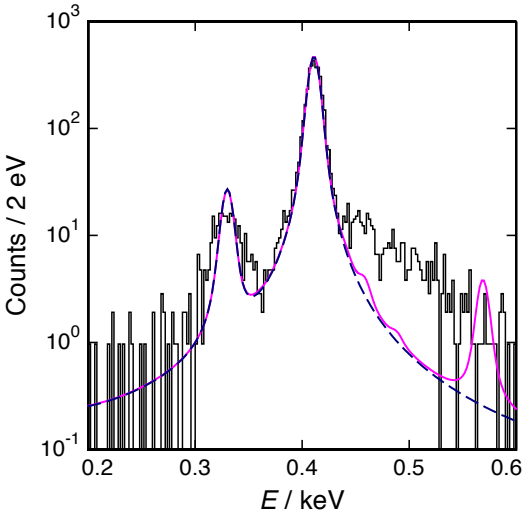

Figure 1.4: Comparison of experimental data (black line), first- (blue dashed line) and second-order theory by Fässler (pink line) in the NI region [47].

spectrum, on the other hand Fässler expects the statistics to be not strongly modified by the same processes. For the sake of clearness, one must say that the two theoretical approaches are quite different and still it is not possible to come to a common agreement on which is the most reliable one. In particular, in [46] only the electrons generating the two holes are considered as "active" electrons, while the others are seen as "spectators" and mainly taken into account in the computation of the electrical charge of the system or of the allowed/forbidden transitions. A non-relativistic, Coulombic approximation is used to describe the atomic system, in the framework of the sudden approximation, with the electronic wave functions still being "crude approximations" [sic]. In [44] instead, the ^{163}Ho and ^{163}Dy* atomic states are fully-antisymmetrically derived with a Slater determinant and a relativistic approach. In the two atoms an orthonormal set of states describes all the orbitals, meaning that the electrons in ^{163}Dy* are assumed to have had enough time to readjust to the new environment after the EC has taken place, which translates into exactly the opposite of the sudden approximation.

Moreover, the approximation that considers the intrinsic line shape of the events coming from the same ^{163}Dy excited states, in a calorimetrically measured spectrum, as a Breit-Wigner function cannot be optimal to describe the tails of the different lines. This problem was already deeply studied by Riisager in [48], where it was discussed how, for each excited state, a large number of de-excitation modes take part into the daughter atom decay to the ground state and the decay paths could be different for different captured electrons. In [48], in order to describe this effect, an energy dependent factor was introduced in the formula describing the intrinsic line shape. This additional factor introduces an asymmetry in the line shape in such a way

that the low energy tail goes to zero more rapidly, while the high energy tail shows a slightly enhanced intensity, and this approach was used to estimate the intensity of the MI line.
In the next future, high resolution and high statistics calorimetrically measured ^{163}Ho spectra with a total number of counts larger than 10^8 will provide important knowledge for theorists. However, the nature of the calorimetric measurement does not allow to study the different de-excitation modes of ^{163}Dy. The possibility to independently study the radiative and non-radiative parts of the de-excitation of ^{163}Dy would provide new ways for better understanding the ^{163}Ho EC spectrum.
In this thesis a new approach to investigate the radiative de-excitations and, to some extent, the non-radiative ones, is discussed. The method consists of the simultaneous measurement of the energy deposited in a detector whose surface is implanted with ^{163}Ho at a $\sim$ 100 nm depth and the energy seen by a large area detector positioned very close to the surface containing the ^{163}Ho. This way, the X-rays emitted in the de-excitation of the ^{163}Dy and exiting the source-detector can be measured by the large area detector in coincidence with the energy released in the source itself. The design of such experiment is discussed in sec. 3.4.

Chapter 2

The ECHo Experiment

2.1 ν-mass sensitivity of ^{163}Ho experiments

With the ^{163}Ho source enclosed in the detector, all the decay energy is measured minus the energy of the neutrino, so that the measured energy spectrum is complementary to the energy spectrum of the neutrino. The sensitivity on m_{ν_e} that can be reached depends on several parameters, in particular on the number of events occurring in a suitable energy interval below Q_{EC}, which is in turn related to the total number of events in the full spectrum. For example, in the region of the spectrum corresponding to the last eV below $Q_{EC} = 2.833$ keV, only a fraction of about 6×10^{-13} of the total decays would count. This already indicates that to reach a sub-eV sensitivity on m_{ν_e} more than 10^{14} EC decays of the ^{163}Ho source should be measured.
Anyway, having enough counts in a suitable region of the spectral end-point is not the only requirement, since the energy of each event is measured with detectors having a finite energy resolution and since events which are not related to the ^{163}Ho decay or which originate from pile-up processes could occur. For this reason, the detector energy resolution is needed to be better than 5 eV (FWHM).
In order to understand the effects of background events it is important to classify the background sources. If the ^{163}Ho source is enclosed in the detector every event is measured, leading to unresolved pile-up events due to the finite response time of the detector. In fact, two events (with energies E_1 and E_2) can happen in the same detector within a time interval Δt smaller than the finite time resolution of the detector itself so that they are seen as a single event having an energy of about the sum of the energies of the two single events $E \approx E_1 + E_2$. The contribution of the pile-up events to the total

spectrum takes the name of pile-up fraction $f_{\rm pu}$ and can be described as:

$$f_{\rm pu} := \mathcal{A}_{det}\, \tau_{rise} \tag{2.1}$$

where $\mathcal{A}$ is the activity of the single detector and τ_{rise} is the shortest time interval between two events and can be identified with the rise-time of the detector signal.
Figure 2.1 shows the ^{163}Ho spectrum calculated for 10^{14} events (blue dashed line). The pile-up spectrum (black line) is calculated convolving the calorimetric spectrum with itself for a Q-value Q_{EC} = 2.8 keV and results in a pile-up fraction of $f_{\rm pu} = 10^{-6}$. In this case, a fraction of the total spectrum of 7×10^{-10} events fall into the last 10 eV below the end-point. The sum of ^{163}Ho and pile-up spectra is also shown (red line). As one can notice, the contribution of the pile-up spectrum for energies below 2 keV is marginal. In order to estimate the background in the last eV of the ^{163}Ho spectrum, one could apply eq. 2.1 to each detector, but it is also possible to analyze the summed spectrum in the energy region above 3 keV.
The pile-up fraction at the end-point also sets the upper level for the amount of acceptable external background. This can be either due to radioactive contaminants in the detector volume (in the fabrication materials or in the embedded source), or to natural radioactivity of the contaminants in the materials surrounding the detector, or to detected muons from cosmic rays. The external background also needs to be estimated and reduced to be well below the intrinsic background.

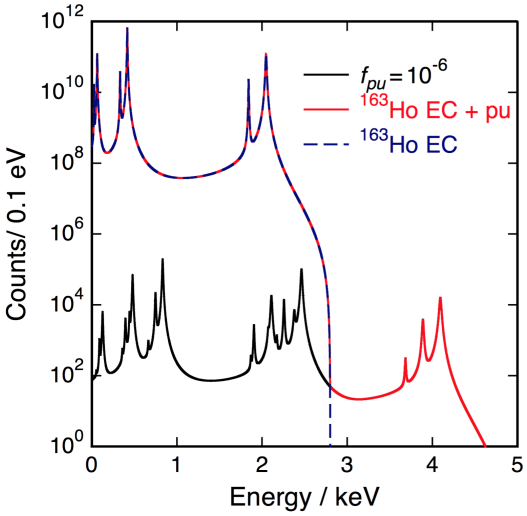

Figure 2.1: The effect of the pile-up events on the calorimetric spectrum of ^{163}Ho. The pile-up fraction here is $f_{\rm pu} = 10^{-6}$. The blue dashed line shows the EC calorimetric spectrum of ^{163}Ho without pile-up, the black line shows the pile-up contribution and the red line shows the sum of the two.

Figure 2.2 shows the simulation of the statistical sensitivity to m_{ν_e} as a function of the pile-up fraction reachable with the measurement of the calorimetric energy of the EC decay of ^{163}Ho. Several values for the detector

resolution were considered, and for the calculation the independently measured Q-value $Q_{EC} = 2.833$ keV was used. The data on the left was obtained for a collected statistics of $N_{ev} = 10^{10}$ events, while the data shown in the plot on the right was obtained for $N_{ev} = 10^{14}$. From these simulations one can see that a pile-up fraction of $f_{\rm pu} = 10^{-5}$ and a detector resolution of $\Delta E_{\rm FWHM} = 5$ eV could be already enough to fulfill the goal of 10 eV sensitivity to m_{ν_e}, while to reach the sub-eV sensitivity a pile-up fraction $f_{\rm pu} = 10^{-6}$ and a detector resolution $\Delta E_{\rm FWHM} < 3$ eV are needed.

A number of attempts of estimating m_{ν_e} with the EC of ^{163}Ho has been performed so far: a calorimetric measurement with a ion-implanted Si-detector [49], a calorimetric measurement with a proportional counter [50], a calorimetric measurement with a NTD Ge detector [51] and an IBEC (Internal Bremsstrahlung Electron Capture) spectrum measurement with a Si(Li) detector [3]. In particular, the latter measurement was able to set the lowest upper limit for the electron neutrino mass m_{ν_e} reached with this technique which is currently known, and which corresponds to

$$m_{\nu_e} \leq 225\,\text{eV}\ (95\%\,\text{C. L.}), \tag{2.2}$$

for which a Q-value of $Q_{EC} = 2.64$ keV was used [52]. A further discussion about the experiments which employed the measurement of the radiative spectrum of ^{163}Ho in the search for the electron neutrino mass can be found in sec. 2.1.3.

Despite the lively interest around the potentiality of ^{163}Ho as a mean to access the electron neutrino mass, the limited performance of the available detectors was not suitable for the purpose of such a measurement, and led to no further progress in this field until the present days. However, the recent development of high resolution cryogenic detectors is making the research of neutrino mass via the EC in ^{163}Ho a valued and competitive task again. In this context, two major collaborations were born in the last decade, namely the Electron Capture with ^{163}Ho experiment (ECHo) [53] and the Electron Capture-decay of ^{163}Ho to Measure the Electron Neutrino Mass with sub-eV Sensitivity (HOLMES) [54]. Besides this two main collaborations, an always increasing number of institutions are showing their interest in the topic in the last years, as e. g. LANL (Los Alamos National Laboratory) [55] and NIST (the american National Institute for Standards and Technology) [56, 57], which for example formed the NuMECS collaboration.

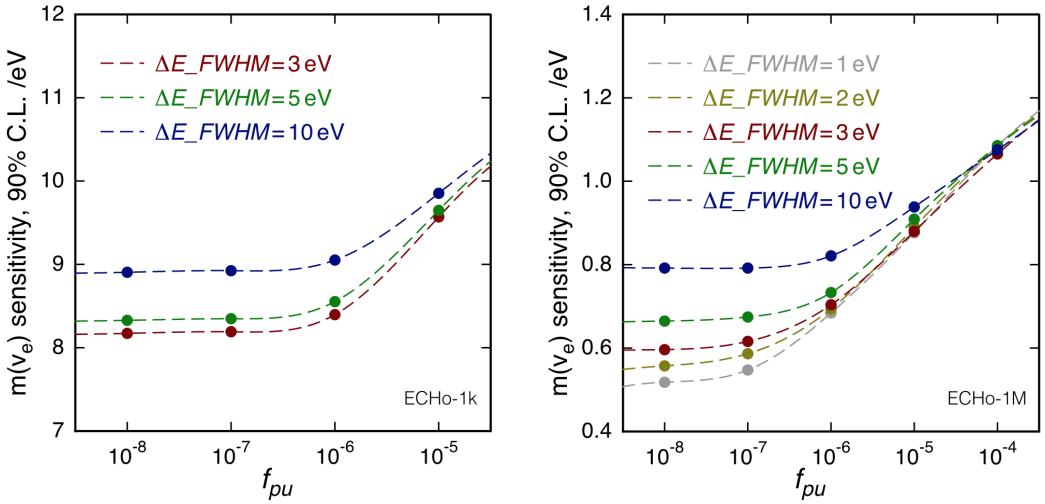

Figure 2.2: Left: statistical sensitivity to the electron neutrino mass m_{ν_e} of a ^{163}Ho electron capture-based experiment as a function of the pile-up fraction, plotted for a detector resolution ΔE_{FWHM} of 3, 5 and 10 eV and for a collected statistics of $N_{ev} = 10^{10}$. Right: statistical sensitivity to the electron neutrino mass m_{ν_e} of a ^{163}Ho electron capture-based experiment as a function of the pile-up fraction, plotted for a detector resolution ΔE_{FWHM} of 1, 2, 3, 5 and 10 eV and for a collected statistics of $N_{ev} = 10^{14}$. For both plots a Q-value $Q_{EC} = 2.8$ keV was considered.

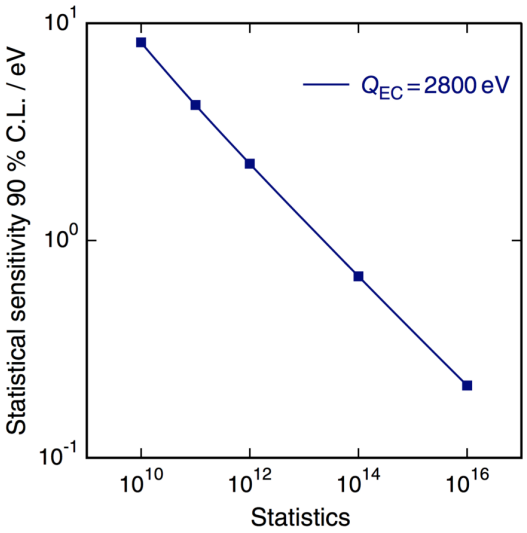

Figure 2.3: Statistical sensitivity for the measurement of m_{ν_e} as a function of the acquired statistics, for a Q-value of $Q_{EC} = 2.8$ keV, a pile-up fraction of $f_{pu} = 10^{-6}$ and a detector resolution $\Delta E_{FWHM} < 3$.

2.1.1 ECHo - Electron Capture in ^{163}Ho

The goal of the Electron Capture in ^{163}Ho experiment is to investigate the electron neutrino mass by means of a high-statistics and high-sensitivity mea-

surement of the calorimetric energy spectrum resulting from the (nuclear) electron capture decay of ^{163}Ho. For this experiment a high-purity ^{163}Ho source will be enclosed in a large number of low temperature detectors able to measure the energy released in every EC event with extremely high precision. These detectors are Metallic Magnetic Calorimeters (MMCs) [58] and will be discussed in sec. 3.1.
At its first stage, namely ECHo-1k, the project aims at improving the current electron neutrino mass upper limit given in eq. 2.2 by more than one order of magnitude. At the same time ECHo-1k will help in proving the scalability of the experiment into its second phase, ECHo-1M, with which a sub-eV sensitivity to the electron neutrino mass is aimed. ECHo-1k comes as a medium-size experiment for which a sample activity of $\mathcal{A} = 1$ kBq is planned. If each detector has an activity of $\mathcal{A}_{det} = 10$ Bq, a number $N_{det} = 100$ of detectors is needed. In order to access m_{ν_e} in the region below the 10 eV a pile-up fraction of $f_{\mathrm{pu}} < 10^{-5}$ and a detector resolution $\Delta E_{\mathrm{FWHM}} < 5$ eV are also needed. For investigating the sub-eV range an activity of $\mathcal{A} = 10^6$ Bq is planned, for a total amount of detectors of about $N_{det} = 10^5$. The required pile-up fraction and detector energy resolution would be $f_{\mathrm{pu}} < 10^{-6}$ and $\Delta E_{\mathrm{FWHM}} < 3$ eV.
To achieve the suitable conditions for the measurement of the electron neutrino mass, efforts are being made on both the theoretical and experimental sides. The optimization of the single detector pixels and of the ^{163}Ho implantation process, then the production and testing of pixel arrays and the development of a low-noise, highly sensitive low-temperature read-out are among the main tasks on the hardware side. Background studies, briefly discussed in sec. 2.1, and the theoretical and experimental parametrization of the calorimetric energy spectrum of EC in ^{163}Ho are also of major importance, and in this context a first independent measurement of the decay Q-value was already performed [43] (and more are planned [59]). Finally, cryogenics is needed to test the detectors and the readout, and, last but not least, to reach suitable temperatures for a high-precision measurement. An overview of the experiment and its recent progress can be found in [60].
The planned milestones for the first stage of the ECHo experiment, namely ECHo-1k, are summarized as follows:

- the ability to read out 100 MMCs with microwave SQUID multiplexing while preserving the single pixel performance,
- the arrangement of an experimental cryogenic platform suitable for both the ECHo-1k and the ECHo-1M phases of the experiment,
- the preparation of a high-purity ^{163}Ho source with a large activity of

10 MBq,

- the identification of the background sources and reduction of the background to a level below the unresolved pile-up spectrum,
- an improved characterization of the ^{163}Ho EC calorimetric energy spectrum, including the study of the de-excitation processes of ^{163}Dy*, for the reduction of the systematic uncertainties,
- an even more precise determination of the ^{163}Ho Q_{EC} value.

The know-how developed during this first stage will define the scalability of the developed techniques for the realization of the second-phase experiment ECHo-1M, as already mentioned above.

2.1.2 Recent results for the ECHo experiment

As explained in sec. 1.2.5, even though the higher order excitations in ^{163}Dy* occur with a much lower probability than the first-order, one-hole excitations, their contribution to the calorimetric spectrum of ^{163}Ho cannot be neglected. The theoretical calorimetric spectrum calculated for the Q-value given in eq. 1.24 is shown in fig. 2.4, for which the parameters presented in A. Fässler's work [44] have been used. The first-order transitions MI, MII, NI and NII are indicated together with the resonances due to second-hole excitations. Three-hole excitations were not included in this calculation due to their negligible contribution to the energy spectrum. For further details concerning this aspect one can refer to [61].
In fig. 2.5 the EC spectrum of ^{163}Ho measured with a first ^{163}Ho-implanted MMC detector prototype is shown [62], which had an activity per pixel of 10^{-2} Bq, an energy resolution of $\Delta E_{FWHM} \simeq 7.6$ eV at a working temperature of 30 mK, and a rise-time of about 130 ns. The same detector operated at a temperature of 20 mK, with an improved experimental setup and read-out system, performed an energy resolution of $\Delta E_{FWHM} = 2.4$ eV with an unchanged rise-time of 130 ns.
Two new chips were implanted at ISOLDE[1]-CERN in 2014. The implanted detectors were designed for high-resolution spectroscopy of X-rays with energies up to 20 keV (namely, the maXs-20 detectors fabricated in the clean room of the Kirchhoff Institute for Physics of the University of Heidelberg), arranged in an 8-channel array, each channel consisting of two pixels in a gradiometric configuration [60]. One of the two ^{163}Ho-implanted chips was used for this thesis work and is further described in sec. 3.2.1, while the

[1]Isotope Separation OnLine DEvice

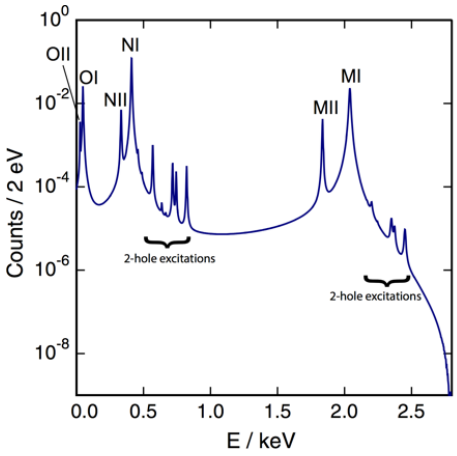

Figure 2.4: Expected calorimetrically measured ^{163}Ho spectrum including first- and second-order transitions according to [44].

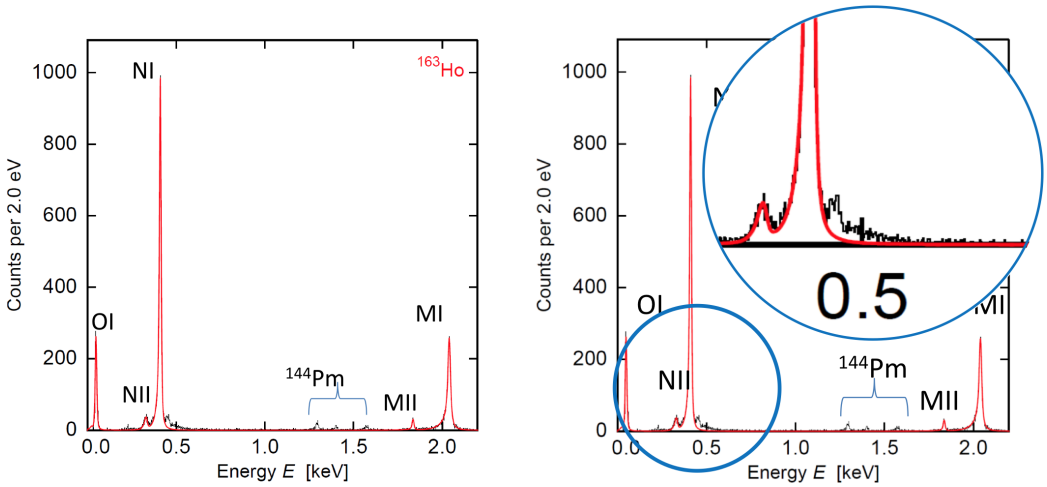

Figure 2.5: ^{163}Ho EC spectrum measured with MMC detectors. The data (black line) is fitted using the convolution of the simulated experimental detector response with the theoretically predicted spectrum (red line). The used parameters can be found in [63]. Some structures due to contamination from ^{144}Pm are also visible in the energy region around 1.4 keV. The zoomed area on the right shows some structures at the upper tail of the NI line which are still not well understood, and might depend on higher-level excitations of ^{163}Dy* or on condensed matter effects, such as the shifting of the core-level binding energy of ^{163}Dy in a gold environment.

second one was already used in several experiments. In fig. 2.6 one can see two regions of interest of the first test ^{163}Ho EC spectrum. The test was performed with two of these implanted detectors (4 pixels in total), while the full spectrum is obtained summing the data collected by two pixels in a data-taking period of about one day at the Kirchhoff Institute for Physics of the University of Heidelberg, for a total number of events of about 17500.

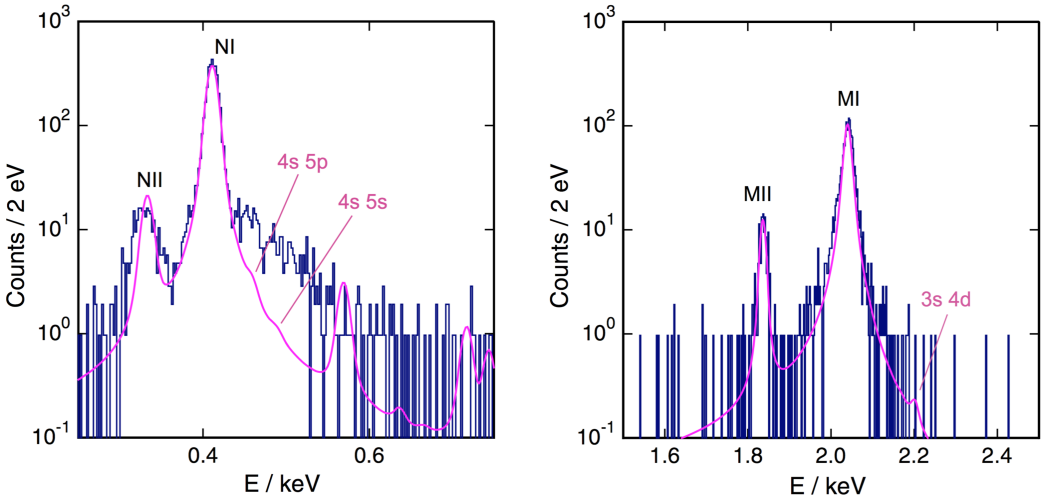

Figure 2.6: Left: ^{163}Ho EC spectrum in the energy region around 450 eV (N-lines). The data (blue line) was taken in 2015 with an activity of about 10^{-1} Bq per pixel. Right: ^{163}Ho EC spectrum in the energy region around 2000 eV (M-lines). Both data sets are compared to the convolution of the theoretical spectrum with the gaussian response of the detector, assuming a detector energy resolution ΔE_{FWHM} of 8 eV for the plot on the left and of 12 eV for the plot on the right.

Although an excess of counts is visible at the NI line, one can see there is a good agreement of the NI, NII, MI and MII amplitudes with the theory. The OI line was measured too, as shown in fig. 2.5. Nevertheless, to better understand the structures of the spectrum different and parallel experiments which allow to investigate the excited states in ^{163}Dy are required.

2.1.3 Investigation of de-excitation processes in ^{163}Dy after electron capture

In sec. 1.2.5 first- and second-order excited states in ^{163}Dy after EC were discussed. The available data shows clear disagreement with the two theories by De Rujúla [46] and Fässler [44]. A possible way to investigate the states populated in ^{163}Dy after the EC is to analyze the X-ray spectrum upon the de-excitation of the ^{163}Dy daughter atoms. In the past, several groups performed measurements of the X-rays after the EC in ^{163}Ho. The idea of using the internal Bremsstrahlung in electron capture (IBEC) for measuring the electron neutrino mass was proposed by De Rujúla and dates back to 1981 [64]. In fact, in [64] it was pointed out how the end-point of the IBEC spectrum depends on the three-body kinematics of the decay and it is sensitive to m_{ν_e} the same way as in a β-decay process. Even though the

intensity of IBEC is quite low, the research in this direction was encouraged by the fact that it is resonantly enhanced when the nuclear Q-value is close to the binding energy of one of the atomic S-states [64, 65], so that ^{163}Ho immediately became a favorite candidate for this search.
In light of this fact, three groups turned their efforts into the study of the IBEC spectrum of ^{163}Ho for the measurement of m_{ν_e}, namely a european Aarhus-CERN collaboration, the Princeton-Livermore group in the US and the Japanese group at KEK. From the european side, the partial M1-capture half-life of ^{163}Ho was measured using the EC rates and the number of active atoms in the ^{163}Ho source, along with an estimate of the Q-value based on this result. Also, a direct measurement of the Q-value was performed by nuclear reaction experiments [66]. Their results are summarized below:

$$Q_{EC} = 2.3 \pm 1.0\,\mathrm{keV} \qquad \tau_{1/2}^{\mathrm{Ho}} = (7 \pm 2) \times 10^3\,\mathrm{y} \qquad m_{\nu_e} \leq 1.3\,\mathrm{keV}\ . \quad (2.3)$$

Still on the european side, the validity of the IBEC theory proposed in [64] was proved with a ^{193}Pt experiment, and led to a limit on the electron neutrino mass of [67, 68]

$$m_{\nu_e} \leq 500\,\mathrm{eV} \quad (95\%\,\mathrm{C.L.})\ . \quad (2.4)$$

The american group started investigating m_{ν_e} by measuring the relative capture ratio from different electron orbits in ^{163}Ho [69]. They measured the ^{163}Ho M X-rays with a Si(Li) detector [66] and its half-life by isotope-dilution mass spectrometry [42], and using this last result they could also infer a Q-value for the decay, getting the results

$$\tau_{1/2}^{\mathrm{Ho}} = 4570 \pm 50\,\mathrm{y} \quad (95\%\,\mathrm{C.L.}) \qquad Q_{EC} \simeq 2.65\,\mathrm{keV} \quad (2.5)$$

from which it became clear that the Q-value was higher then expected from its first measurements. This made them change their initial approach and they also started measuring the IBEC spectrum of ^{163}Ho [70]. They indeed performed the measurement of the IBEC photon spectrum of ^{163}Ho in the region 5p-3s with a Si(Li) detector in air, and what they got is a new upper limit for the electron neutrino mass [70, 3]:

$$m_{\nu_e} \leq 225\,\mathrm{eV}\ (95\%\,\mathrm{C.L.})\ . \quad (2.6)$$

Today this value is still the lowest upper limit on the electron neutrino mass obtained with experimental techniques based on the EC decay of ^{163}Ho. However, Riisager described this result [48] as questionable for a number of reasons, among which the strong dependence of the measurement on the

Q-value given in [52] was also listed, and in the following years he developed the theoretical framework discussed in sec. 1.2.5.
The KEK-collaboration in Japan also decided to follow the approach proposed in [64] for the measurement of the electron neutrino mass. Using a M X-ray spectrum from EC in ^{163}Ho combined with M X-ray fluorescence of ^{163}Dy they could get the following results for Q-value and electron neutrino mass [71]:

$$Q_{EC} = 2.710^{+0.100}_{-0.500}\,\text{keV} \qquad m_{\nu_e} = 110^{+350}_{-110}\,\text{eV} \ . \tag{2.7}$$

With the presently available technology of low-temperature MMCs, it is finally possible to access the total energy of the EC decay process of ^{163}Ho by means of a calorimetric measurement. The main goal of this thesis work is to present and show the feasibility of a novel method for the study of the excited states and de-excitation processes of ^{163}Dy* following the electron capture decay of ^{163}Ho. This is pursued by performing a coincidence measurement between the non-radiative and radiative events of the ^{163}Ho decay, which for the first time gives access to the radiative component of the spectrum while getting the non-radiative one at the same time, and allows so to better characterize the structures of the calorimetric energy spectrum of ^{163}Ho electron capture with the final aim of measuring the electron neutrino mass.
At this purpose, ^{163}Ho-implanted MMCs, discussed in further detail later in sec. 3.1, are prepared in such a way that the non-radiative energy is measured in the MMCs themselves, but the X-ray photons can, in principle, escape the detectors and be measured by other nearby, non-implanted MMCs specifically designed for this, having a high energy resolution $\Delta E_{FWHM} < 10$ eV. This can happen thanks to the fact that on these implanted detectors, unlike the ones described in sec. 3.1, an absorber layer of only 300 nm of Au was deposited on top of the implanted ^{163}Ho atoms. This allows to measure simultaneously the energy released in the source and the one escaping due to the photons, which are then stopped in the designed high-resolution MMCs placed in front of the source. The actual detection setup is described in sec. 3.4.
The difficulties of such a measurement mainly originate from the need for building a reliable experimental setup and from the low branching ratio for the emission of X-rays [40], even though a coincidence measurement performed with high resolution detectors (from both the source and the X-ray detection sides) will lead to a precise identification of the ^{163}Ho events.

Chapter 3

The experimental setup

In this chapter the working principles of low-temperature metallic magnetic calorimeters and the SQUID read-out are discussed. Details about the detectors employed for this work are given in sec. 3.2.1 and sec. 3.2.2, along with a brief description of the used cryostat in sec. 3.3. The whole experimental setup is shown and described in sec. 3.4, followed by a description of the data acquisition system in sec. 3.5.

3.1 MMCs - Metallic Magnetic Calorimeters

In order to reach the sub-eV sensitivity on m_{ν_e} with ^{163}Ho-based experiments a detector energy resolution $\Delta E_{\mathrm{FWHM}} < 3$ eV as well as a very good time resolution are required, as explained in sec. 2.1.

In the context of the ECHo experiment, as well as for the measurements discussed in this thesis work, cryogenic Metallic Magnetic Calorimeters (MMCs) [58], operated at temperatures in the mK range, are used. This choice is based on the excellent energy resolution of $\Delta E_{\mathrm{FWHM}} = 1.6$ eV [72] and an unprecedented rise-time of $\tau_{rise} = 90$ ns at 30 mK [73] achieved so far with the MMCs[1]. A sketch of the general structure of an MMC is given in fig. 3.1 along with the typical signal shape.

The working principle of these thermal detectors is a calorimetric principle, that means the energy ΔE_{EC} deposited by the particles emitted in the de-excitation process of ^{163}Dy induces a rise in temperature ΔT in the detector

[1] MMCs showed such a performance in their main application field of detection of soft X-rays. A similar performance can be expected for calorimetric electron capture spectroscopy.

which is proportional to this energy:

$$\mathrm{E}_{EC} \propto \Delta\mathrm{T} \propto \frac{\Delta\mathrm{E}}{\mathrm{C}_{tot}}, \tag{3.1}$$

where C_{tot} is the total heat capacity of the detector. After the initial temperature rise, the detector slowly relaxes back to the temperature of the thermal bath, with a relaxation time τ_{rel} defined by the weak thermal link of thermal conductance G according to:

$$\tau_{rel} \approx \frac{\mathrm{C}_{tot}}{\mathrm{G}} \quad . \tag{3.2}$$

For a paramagnetic sensor material, the fundamental energy resolution of the detector is defined by the energy fluctuations between the thermal system composing the detector and, under the assumption that the heat capacity of the spin system C_{spin} equals the one of the electron system C_e, is given by [74]:

$$\Delta\mathrm{E}_{\mathrm{FWHM}} \simeq 2.36 \sqrt{4k_{\mathrm{B}}\,\mathrm{C}_{abs}\,\mathrm{T}^2} \left(\frac{\tau_{rise}}{\tau}\right)^{\frac{1}{4}} \quad . \tag{3.3}$$

3.1.1 Geometry of an MMC

To make sure that a calorimetric measurement is performed, i. e. all the energy released in the EC decay of ^{163}Ho is measured in the detector independently of the decay channel, the ^{163}Ho source is embedded in the detector and surrounded by an amount of absorber material such that the absorption efficiency is as close as possible to 100%. To realize this, the absorber thickness should be enough to cover at least seven times the attenuation lenght λ of the least stopped de-excitation product. An absorber material commonly employed in MMCs is gold, in which, for energies below $\mathrm{E}_{EC} \leq 3$ keV, the least stopped radiation is photons having energies just below the MIV threshold of gold, namely $\mathrm{E}^{\mathrm{Au}}_{\mathrm{MIV}} = 2205.7$ eV [75]. The corresponding attenuation length for these photons is $\lambda = 0.56\,\mu$m.
A suitable geometry for such an absorber consists of a first planar layer of about $5\,\mu$m of gold, on whose surface the ^{163}Ho source is deposited (taking care of not covering the area along the borders, as shown in fig. 3.1), and a second absorber layer on top having the same size of the first one, in a so-called 4π geometry.
The thermal sensor that reads out the temperature rise in the absorber is a dilute paramagnetic alloy of erbium in gold (a few hundred ppm), placed in a stable magnetic field B ($\sim$ mT) which polarizes the spins in the sensor material. An analysis of the properties of Au:Er is given in the appendix 4.1.1.

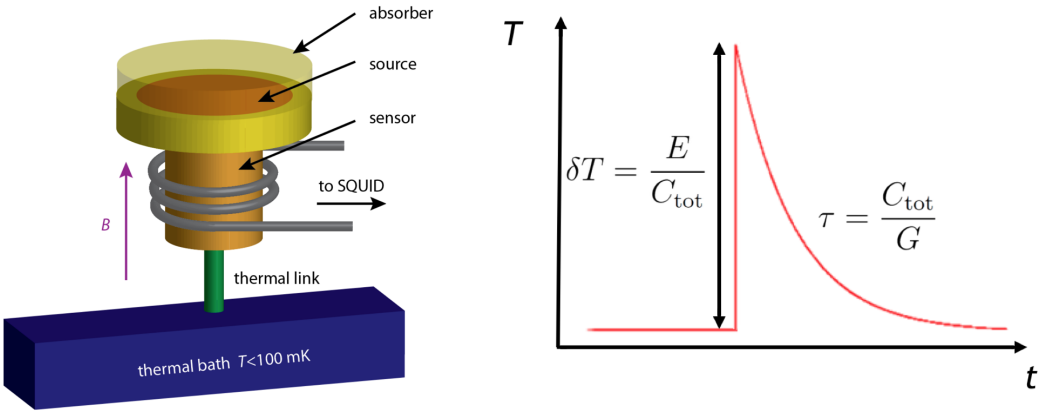

Figure 3.1: Left: the schematics of an MMC for calorimetric measurements. The absorber with the embedded radioactive source is closely connected to the Au:Er sensor, in turn weakly connected to a thermal bath. The sensor is placed in a weak magnetic field B and surrounded by a superconducting loop, which is connected to the read-out SQUID. Left: the typical signal shape of an MMC.

The main reason for using Au:Er as a sensor material is that its magnetization M shows a very marked dependence on temperature, when the operational temperature is below T $\leq$ 100 mK. The change in magnetization in the sensor due to the change of temperature is in turn read-out by a closed superconducting pick-up coil put in the vicinity of the sensor. In fact, the change in magnetization causes a change of magnetic flux in the superconducting loop, and the resulting induced current is read out by a SQUID[2] whose input coil is directly connected to the pick-up coil. This way, the signal resulting from the change of flux in the SQUID is still proportional to the absorbed energy:

$$\Delta\Phi_S \propto \frac{\partial \mathrm{M}}{\partial \mathrm{T}} \Delta \mathrm{T} \approx \frac{\partial \mathrm{M}}{\partial \mathrm{T}} \frac{\Delta \mathrm{E}_{EC}}{\mathrm{C}_{tot}} \quad . \tag{3.4}$$

MMCs can be reliably produced by micro-fabrication techniques, in a reproducible way. A sketch design of a detector (or detector pixel pair), arranged in a fully gradiometric set-up, and employed for this work, is given in fig. 3.2, along with a schematics of the read-out principle. The picture on the left shows a sketch of the main layers of two pixels: the read-out structures which transfer the flux change to the SQUID, made out of Nb, are represented by the black lines and grey round plane, and are fabricated in two different layers; the Au:Er sensor is depicted in orange; in yellow the gold stems, which thermally connect the sensors to the absorbers, also shown in yellow.

[2]Superconducting QUantum Interference Device

Read-out working principle

The magnetization of the sensor is detected as a change of flux in a superconducting pick-up coil, whose design exists in different possible geometries [76]. The geometry of the detectors used for this work has the so-colled *sandwich* design, which is shown in fig. 3.2 (left). The black and blue arrows represent respectively the persistent current and a signal induced in the detector. The layer with the Nb spiral is connected to the upper Nb plain surface in such a way the sensor between this two layers is superconducting-screened (and "*sandwiched*"). The Au:Er sensor material is deposited on top of the spiral coils, which are connected in parallel to the input coil of a dc-SQUID. Au:Er can be deposited on one or both pick-up coils. If only one is covered the detector is sensitive to absolute temperature changes of the substrate and the magnetization of the sensor material can be measured to characterize the detector. By covering both coils, the magnetization signal of one sensor compensates the signal of the second sensor for a common temperature change. This makes the operation of the detector generally more stable against temperature fluctuations of the substrate and doubles the detection area at the cost of slightly increased noise, as the noise of both sensors couples incoherently into the common read-out SQUID.

The sandwich-structure, which includes the pick-up coils, is not only used to detect the change in magnetization in the sensor, but also serves to generate the magnetic field that polarizes the sensor material. This is achieved by feeding a persistent (or *field*) current I_f of several mA into the strip/coils, as shown in fig. 3.3. For graphic reasons, the meander design is used here, but the working principle is analogue for the sandwich design.

An additional path is added to the meander which is not shown in fig. 3.2. This part forms a nose which is positioned at a suitable distance from the main meander structures forming the two nodes, and is put in close contact to a resistive Au:Pd heater which works as a "switch" for the persistent current. The field generating current I_f is first injected into the field current leads, as shown in fig. 3.2 (a). Due to Kirchhoff's law for superconducting circuits the current is divided according to the inductances of the possible paths. Therefore, most of the current goes through the shorter path of the nose. A current of a few mA is then sent to the heater (fig. 3.2 (b)), so that the power dissipated is enough to increase the temperature of the nearby environment to a temperature larger than the superconducting transition temperature (or critical temperature) of the meander material, typically Nb. This way, the part being close to the heater becomes normal-conducting. The superconducting loop is now open and the magnetic flux through the area formed by the meander is now allowed to change. The new value is defined by the injected field current. At this point the heater current is removed, so

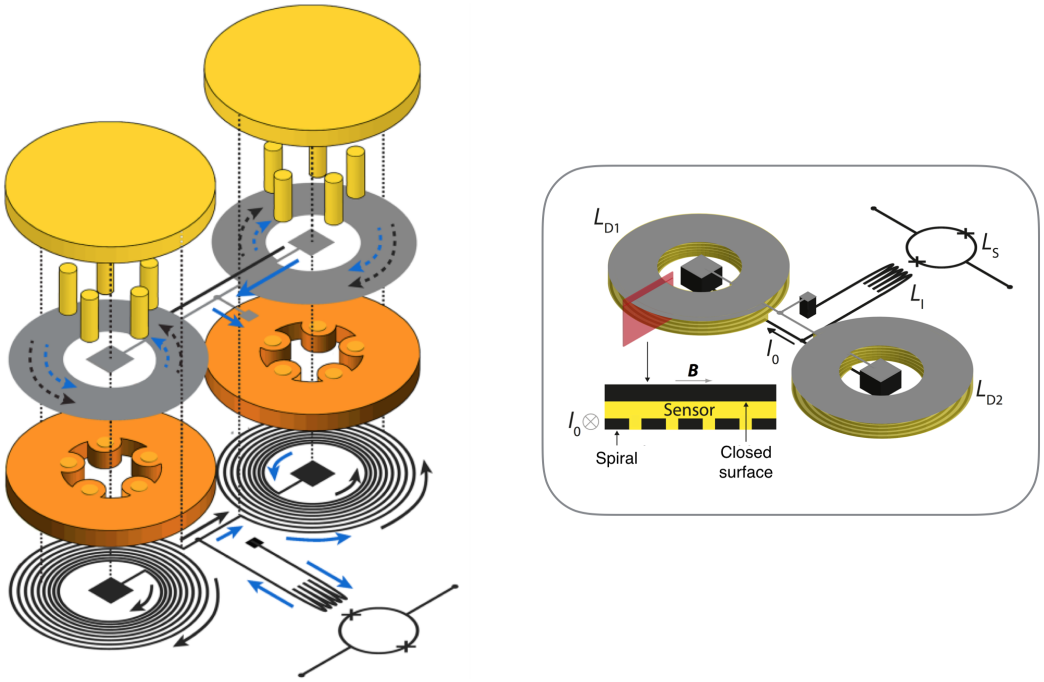

Figure 3.2: Left: diagram of a *sandwich*-designed MMC. The "sandwiched" Au:Er sensor is shown in orange, the two Nb layers are depicted in black (pick-up spiral coils and SQUID input coil) and grey (closed surface above the sensor), while the gold ^{163}Ho-implanted absorber and the stems are depicted in yellow. Right: overview schematics of the detector read-out, with a cross-section of the sandwich structure. The $\otimes$ symbol shows the verse of the persistent current indicated in the picture as I_0. The inductances of the two detectors, the SQUID input coil and the SQUID are labeled as L_{D1} and L_{D2}, L_I and L_S respectively.

that the meander path close to the heater becomes superconducting again and the superconducting loop is closed again, as shown in fig. 3.2 (c).

The persistent current which is flowing through the meander at the end of this procedure is:

$$I'_f = I_f \frac{2\,L_m}{2\,L_m + L_h} \tag{3.5}$$

where L_m and L_h are the inductances of the meanders and of the short path to the heater respectively. Usually, $L_h \ll L_m$ and the assumption that $I'_f \approx I_f$ can be made.

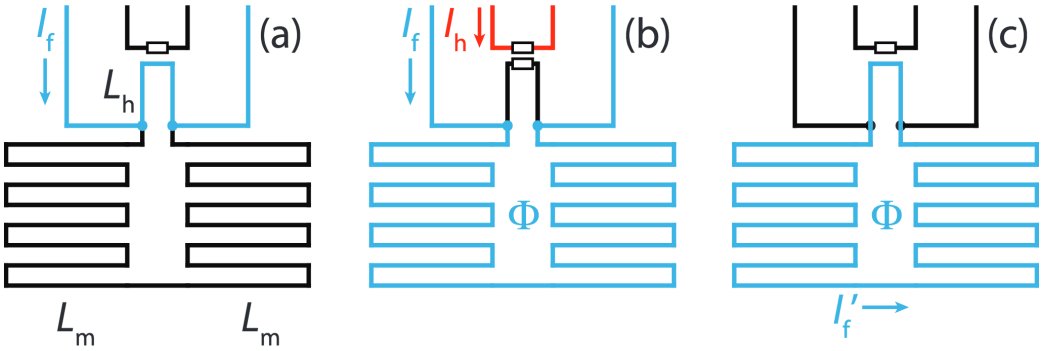

Figure 3.3: The schematic of the injection of a persistent current into a meander-shaped pick-up coil. The different steps are explained in the text.

3.1.2 SQUID read-out

The magnetization change ΔM in the paramagnetic sensor of the MMCs generates the screening currents in the superconducting loop, formed by the two pick-up coils and the input coil of the dc-SQUID. A SQUID (Superconducting QUantum Interference Device) is a low-noise and low-temperature operating superconducting magnetometer. It can be described as an extremely sensitive magnetic flux-to-voltage converter. The very small currents induced by the change of magnetization of the sensor flowing through the input coil generate a flux in the SQUID loop which leads to a change of voltage across the SQUID itself.
In fig. 3.4 the schematics of a dc-SQUID (a) and its characteristic I-U (b) and Φ-U (c) curves are shown. A dc-SQUID consists of a superconducting loop interrupted by two Josephson junctions, i.e. two weak links made of a thin insulating layer (∼ nm), usually a metal oxide, placed between two superconducting leads. The SQUID has two identical Josephson junctions a and b, having both a critical current I_c, the maximum super-current through the device is shown to be $\mathrm{I} = 2\mathrm{I}_c$, and is limited by the phase shifts of the macroscopic wave function at each junction δ_a and δ_b as follows:

$$\mathrm{I} = \mathrm{I}_c(\sin\delta_a + \sin\delta_b) = 2\,\mathrm{I}_c\cos\left(\frac{\delta_a - \delta_b}{2}\right)\sin\left(\frac{\delta_a + \delta_b}{2}\right). \qquad (3.6)$$

The first consequence of the coherent motion of Cooper pairs in closed superconducting loop is the quantization of the magnetic flux into integer multiples of the magnetic flux quantum $\Phi_0 = \frac{h}{2e} \approx 2.07\,\mathrm{Wb}$. Cooper pairs can tunnel through a Josephson junction without any voltage drop up to a critical current I_c, and when this is exceeded a super-current $\mathrm{I} = \mathrm{I}_c$ flows in the loop carried by tunneling quasiparticles, inducing a voltage drop over the junc-

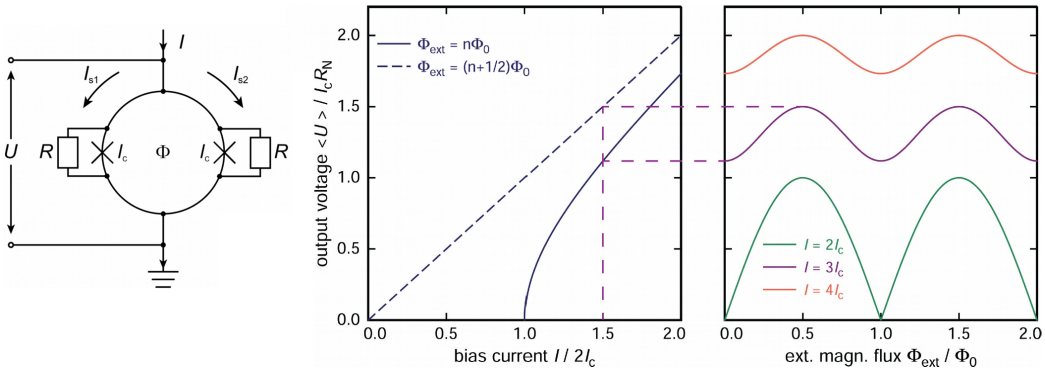

Figure 3.4: Left: schematics of a dc-SQUID, mostly self-explaining. The superconducting loop is represented as a circle with the two "X" being the Josephson junctions. The two resistances connected at the sides of the loop are shunt resistors. The splitting of the super-current I entering the SQUID is also shown. Center and right: I-U and Φ-U characteristics of a dc-SQUID. The I-U characteristics is shown for the two cases $\Phi = n\Phi_0$ and $\Phi = (n + 1/2)\,\Phi_0$, where Φ_0 is the magnetic flux quantum. The Φ-U characteristics is shown for three different bias currents I, equal to multiples of the SQUID critical current I_c, and shows the sinusoidal trend expected from eq. 3.10.

tion. Also, even though flux quanta can enter and leave the loop through the junctions, the circular (or screening) current in the loop has to fulfill the magnetic flux quantization condition on the phase difference $(\delta_a - \delta_b)$, which can be calculated through the integral of the vector potential $\vec{A}$ over the closed path $\vec{s}$ along the SQUID loop:

$$(\delta_a - \delta_b) = \frac{2e}{\hbar} \oint \vec{A}\, d\vec{s} = \frac{2e\,\Phi}{\hbar} = \pi \frac{\Phi}{\Phi_0} \quad . \tag{3.7}$$

If now eq. 3.7 is inserted into eq. 3.6 one gets

$$I = 2\,I_c \sin\left(\frac{\delta_a + \delta_b}{2}\right) \cos\left(\pi \frac{\Phi}{\Phi_0}\right) := I_{max} \cos\left(\pi \frac{\Phi}{\Phi_0}\right) \quad , \tag{3.8}$$

and defining the maximum super-current I_{max} as

$$I_{max} := 2\,I_c \sin\left(\frac{\delta_a + \delta_b}{2}\right) \tag{3.9}$$

one can find an expression for the flux dependence of I. Also, the phase $(\delta_a + \delta_b)$ changes the amplitude of I with changing magnetic field, even though the effect of this dependence is much weaker than the one on the phase difference $(\delta_a - \delta_b)$, and can thus be neglected for small flux variations (of a few Φ_0). This behavior is also called "quantum interference", as the dependence

of I on the magnetic flux shows an interference pattern. The voltage drop of a dc-SQUID is generated due to quasi-particle tunneling, by feeding a bias current $I_b \geq I_{max}$ into the SQUID so that it stays in a resistive operating range. If a constant, normal-conducting resistance R_{SQ} is assumed for the SQUID, the corresponding voltage drop is:

$$U(\Phi) = R_{SQ}\left[I_b - I_{max}\cos\left(\pi\frac{\Phi}{\Phi_0}\right)\right]. \tag{3.10}$$

In order to prevent hysteretic behaviors, a shunt resistor is connected in parallel with each Josephson junction, as shown in fig. 3.4 (a).
Since the voltage response of the SQUID to a flux change is clearly non-linear for flux changes larger than $\Delta\Phi \sim \Phi_0/4$, the implementation of a linearization circuit is crucial for a precise detection of variations in magnetic flux. This is usually realized via a feedback circuit, also known as Flux Locked Loop (FLL) circuit, which allows the SQUID to remain at the same working point (or magnetic flux level) while the current flowing in the input coil generates a different flux coupled to the dc-SQUID.
Figure 3.5 shows a 2-stage SQUID setup in FLL configuration. The dc-SQUID reads the change of flux induced by the change in magnetization in the detector sensor, and the change of voltage across the front-end SQUID is amplified by a second SQUID array. The voltage drop of the amplifier SQUID is measured with a differential amplifier A where it is compared to the bias voltage U_b previously adjusted to set the SQUID working point. This is chosen in such a way that the voltage drop per flux change $\partial U/\partial\Phi$ is the largest one. The output signal of the amplifier goes through a voltage integrator, whose output U_{out} across a feedback resistor R_{fb} leads to a feedback current signal according to $I_{fb} = U_{out/R_{fb}}$. The feedback current is then sent to the feedback coil coupled to the SQUID to generate the compensating flux. The output voltage U_{out} represents the final read-out signal, its proportionality to the feedback flux being:

$$\Delta\Phi_{fb} = \frac{M_{fb}\,U_{out}}{R_{fb}} = -\Delta\Phi \tag{3.11}$$

where M_{fb} represents the mutual inductance between the feedback coil and the SQUID.
The presence of the SQUID array reduces the effect of the noise due to the room temperature electronics. A SQUID array essentially consists of n, in principle, identical dc-SQUIDs connected in series, represented in fig. 3.5 as a single loop labeled as "SQ2". The number of dc-SQUIDs in the array can be 14 or 16. If all the SQUIDs in the array are set at the same working point and exposed to the same flux (achievable with a common input coil), they

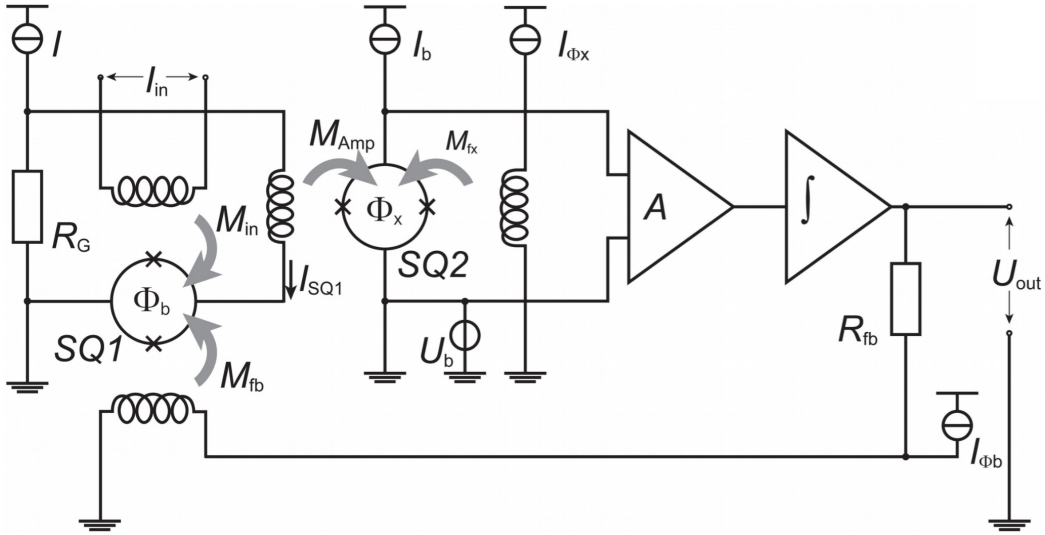

Figure 3.5: The circuitry of a 2-stage SQUID setup. In the actual experimental setup a 16-SQUID array is used instead of the second-stage amplifier SQUID "SQ2" included in this picture. The whole schematics are described in the text.

behave as a single SQUID yet showing a larger voltage oscillation in their Φ-U characteristic. In this schematics, the flux change in the first stage (or front-end) SQUID "SQ1" creates a voltage signal that is turned into a current signal through the gain resistor R_G. This current then induces a flux signal $\Delta\Phi_2 = M_{amp}\,\Delta I_{SQ1}$ into the second stage (or amplifier) SQUID "SQ2" via the input coil connected in series to SQ1 and in close contact with SQ2 itself. An aspect to be taken into account is that, while the voltage drop at the ends of the array scales with n as the input signal couples coherently, the total noise instead only scales with $\sqrt{n}$ because of the noise of the single SQUID adding incoherently to the noise of the others. In this work, for the read-out of the two channels of the ^{163}Ho implanted D14E an integrated 2-stage SQUID chip with two read-out channels was used, each channel consisting of a second-order gradiometric front-end SQUID and a 14-SQUID array. The 32 pixels of the maXs-30 are read out by eight 4-channels front-end SQUID chips which transfer their signal to sixteen 2-channels 16-SQUID array chips.

3.2 Setup for the X-ray coincidence measurement

For the measurement discussed in this thesis, an array of 16 detector pixel was employed (which from now on is addressed by the name of the corresponding

design "D14E"). It was specifically designed for the detection of soft X-rays up to 20 keV, namely the maXs-20 detectors[3], and it was ion-implanted with ^{163}Ho at ISOLDE[4] (CERN) after the first gold absorber layer was deposited and its performance was tested. For the detection of the X-rays coming from the EC decay of ^{163}Ho a maXs-30 detector chip was employed, consisting of a 64 pixel matrix of 32 channels able to detect X-rays of energies up to 30 keV. The project of development and optimization of the maXs-30 is still ongoing and represents the main subject of Daniel Hengstler's doctoral thesis work, which will be published in 2017 [4]. Both the detector chips were designed and microfabricated at the Kirchhoff Institute for Physics in Heidelberg.

3.2.1 The ^{163}Ho-implanted D14E

Figure 3.6 (left) shows a sketch of the D14E chip, and a zoom on the last pixel pair of the detector array (right). The 16 pixel array is labeled as a), where the top yellow layer represents the upper gold absorber. The transparency of the layers in fig. 3.6 (right) allows to see, below the $250 \times 250 \times 5\,\mu$m gold absorber b), the sensor c) and the superconducting pick-up coil.

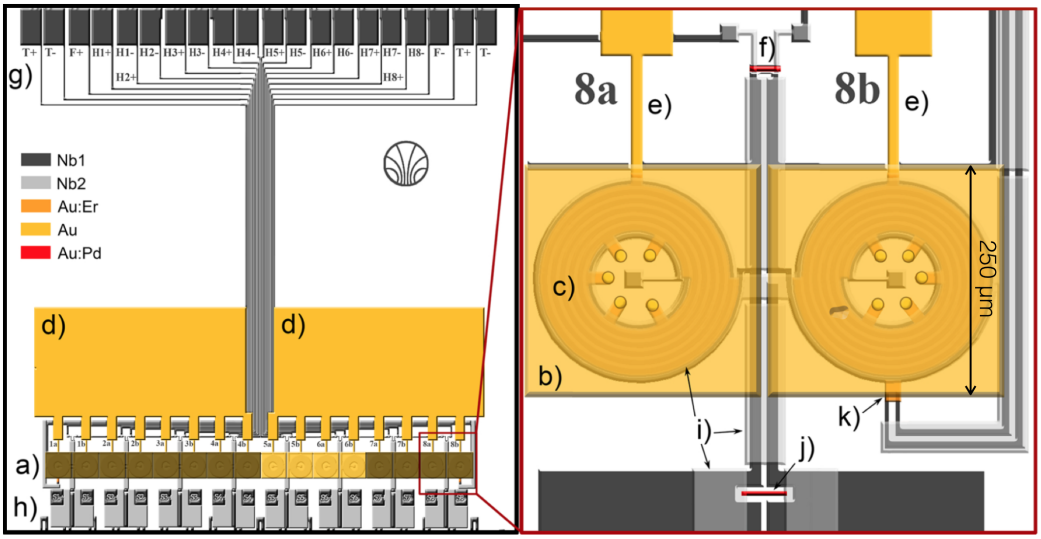

Figure 3.6: Diagram of the ^{163}Ho-implanted D14E chip used for this thesis work. The chip contains a 8-channels array, each channel consisting of two MMC detector pixels. The dark area in the array is the one covered with the absorber mask, which prevents X-rays to escape the unread channels. On the right a zoom on one detector is shown. More details about the picture are given in the text.

[3]Microcalorimeter arrays for high-resolution X-ray spectroscopy up to 20 keV
[4]Isotope Separation OnLine DEvice

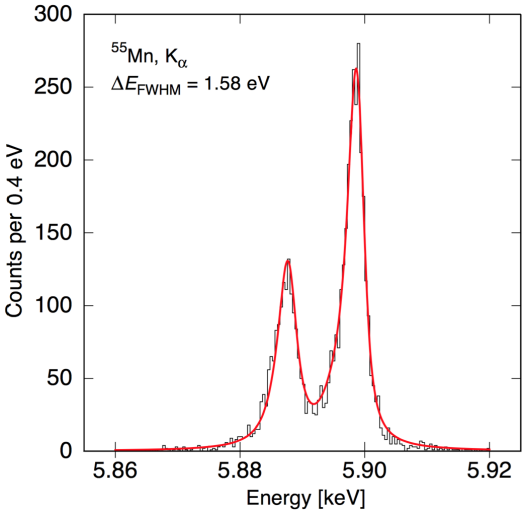

Figure 3.7: Energy resolution of the non-implanted D14E, corresponding to 1.6 eV at detected energies of 6 keV.

The sensor is connected through a gold thermal link e) to the on-chip thermal bath d). The heater is labeled as f) and the bonding pads for the introduction of the field (+F,-F) and heater (+H_n,-H_n) currents and for the connection to the SQUID read-out as g) and h) respectively. The upper Nb layer is indicated as i), while j) is a Au:Pd resistor connecting two bonding pads for the connection to the input coil of the SQUID, which together with the inductivity of the pick-up coil and of the input-coil of the SQUID forms a low-pass filter against high-frequency noise. This way one can reduce the eddy currents induced by the dc-SQUID in the sensor. The label k) instead indicates a normal-conducting sensor contact, accessible from the bonding pads g) (+T,-T) through which it is possible to generate well-defined temperature pulses without making use of the heater. The ^{163}Ho was then implanted on top of each absorber on a reduced area, thanks to a precisely structured, thick photoresist layer which also had the function to protect the chip surface against the implantation. After the implantation, the chip was covered with a 200 nm thick gold layer to protect the ^{163}Ho ions against oxidation. As discussed in sec. 3.1, this is not thick enough to stop the X-rays coming from the de-excitation of the ^{163}Dy*, therefore pixels processed until this stage could be used as ^{163}Ho X-ray source. For this experiment two channels (namely channel 5 and 6) corresponding to four implanted absorbers were intentionally left at this stage in such a way the radiative component of the EC decay of ^{163}Ho could escape the detectors, but not the non-radiative one, while the other twelve absorbers were covered with an additional 5 μm layer of gold for future calorimetric measurements. Figure 3.6 shows the pixel array partially covered by a dark layer, which represents the mask prepared for structuring the second gold layer on the remaining absorbers. The best

performance obtained by a D14E detector was a rise time of 300 ns, defined by the thermal link between absorber and sensor, and a very good energy resolution of $\Delta E_{FWHM} = 1.6\,eV$ at the energy of 6 keV [73], corresponding to the K_α line of ^{55}Mn in fig. 3.7.

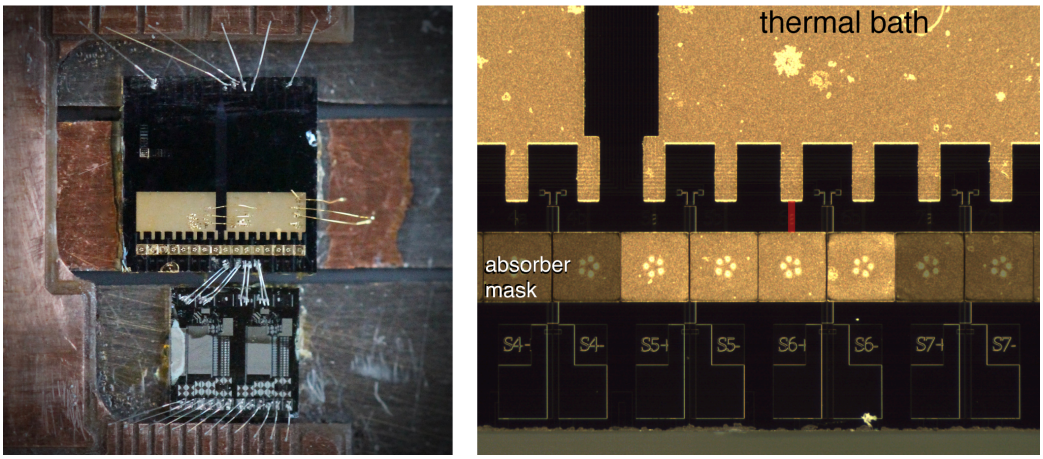

Figure 3.8: The D14E arranged on its experimental holder. The Al-bonds to the circuit board and to its read-out chip are also visible, as well as the thermal Au-bonds connecting the thermal bath to the copper holder. On the left a close-up of the active channels is shown. For clarity, one of the links thermally connecting the sensor to the thermal bath is highlighted in red.

3.2.2 The maXs-30 for the detection of X-rays

Figure 3.9 (left) shows the maXs-30 design and detector (right) with a close-up on the absorber pixels on the top-left corner. The 64-pixel matrix is depicted in yellow, while the black structures along the four sides of the chip are the bonding pads for the connections to the front-end SQUID read-out and for the field- and heater-lines. The matrix can be ideally divided into four quarters as shown in fig. 3.10. In each of these four quarters the detectors share the connections for the field- and heater-currents.
Each pixel is $(500 \times 500)\,\mu m$ in surface, so that the side of the full square matrix is ~ 4 mm. The basic structure of the single pixel is the same as described in sec. 3.1 but, unlike the D14E, the maXs-30 read-out structure was designed to have meander-shaped pick-up coils. The gold absorber is $30\,\mu m$ thick, for a quantum efficiency of $\sim 100\%$ for X-ray having energies of 20 keV and $\sim 80\%$ for X-rays of 30 keV. The best measured baseline energy resolution of the maXs-30 is $\Delta E_{FWHM} = 7.9\,eV$ [4].

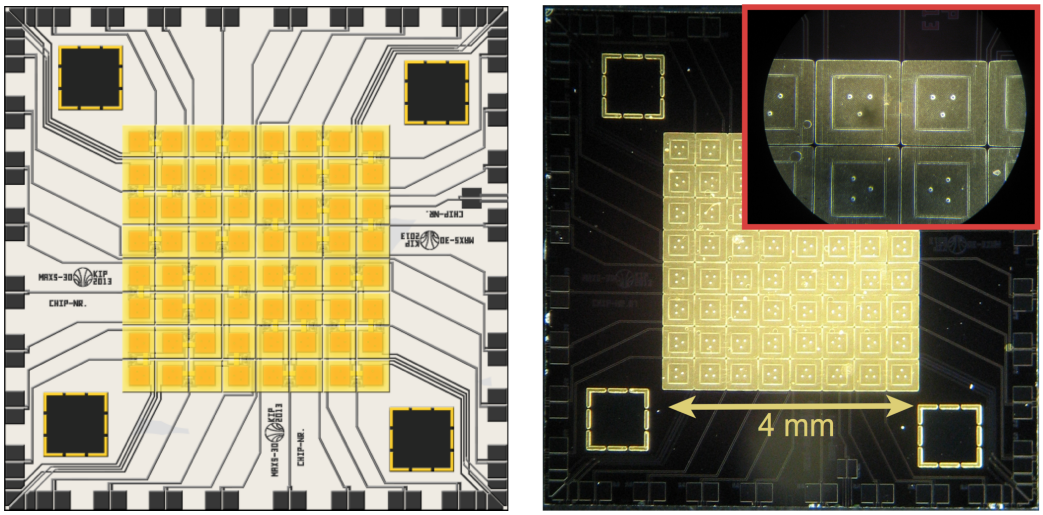

Figure 3.9: A diagram of the maXs-30 chip next to a microscope picture of the real chip, with a close-up on the absorber pixels.

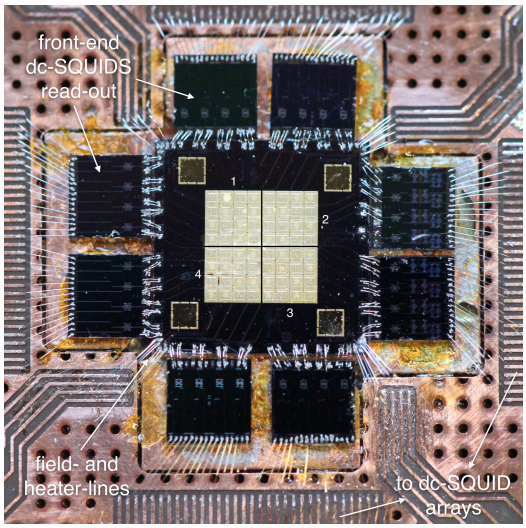

Figure 3.10: A picture of the maXs-30 on its experimental copper holder, surrounded by the read-out front-end SQUIDs. The two black lines drown on the pixel matrix divide it in four quarters, according to the areas covered by each of the four field- and heater-lines.

3.3 The cryostat

The MMCs and their SQUID read-out need to be operated at cryogenic temperatures, for measuring periods which can possibly range from days to months. The D14E, the maXs-30 and their SQUIDs were operated in a dry ^{3}He/^{4}He BlueFors dilution refrigerator, which has a base temperature of 10 mK at the mixing chamber. The main feature of this cryostat is a copper arm connected to the mixing chamber, which provides at its front part an experimental platform suited for the operation of 32 MMC channels. In

addition, three more read-out channels are located directly at the mixing chamber. The coincident X-ray measurement was set up at the front part of this arm.

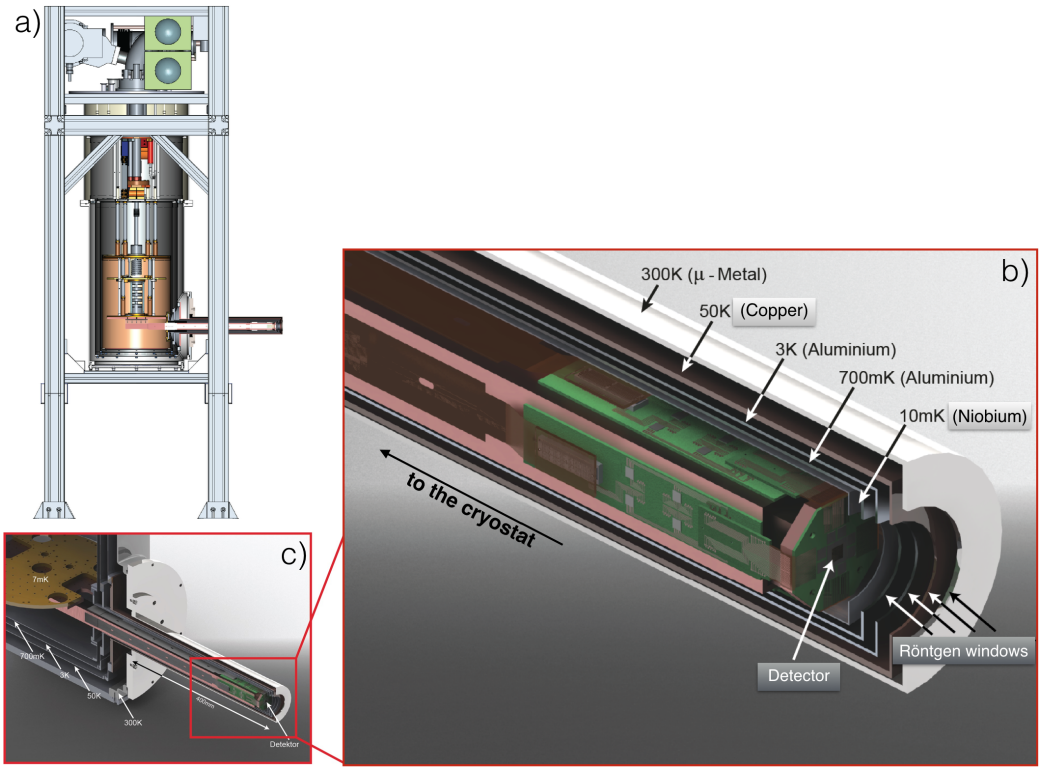

Figure 3.11: Outline of the cryostat which hosted the experimental setup used in this thesis work. In fig. a) a longitudinal cross-section of the whole cryostat, showing the inner experimental platform, the shielding layers and the arm is given. Fig. b) shows a zoom onto the front part of the copper arm and indicates the temperatures corresponding to the volumes delimited by the different shields, and the shield materials. Fig. c) is a close-up on the part of the cryostat where the arm is mounted. More details about the pictures are given in the text.

The cooling of the cryostat to ~ 4 K is achieved by the use of a pulse-tube cooler. Fig. 3.11 a) shows an outline of the cross-section of this cryostat. A dilution unit cools the experimental platform down to mK. The zoom given in fig. 3.11 b) shows the copper arm (in pink) inside its several shields (the outer layers). The copper holder of the maXs-30, with a rough diagram for the detector itself drown on top of it, and its read-out amplifier SQUIDs circuit boards are depicted in green, while the stripes connecting the detector to its read-out and then the read-out to the connections inside the cryostat leading to the outer room-temperature electronics are shown in grey/brown. The

arm is superconducting-shielded against external magnetic fields. The different shields, corresponding to different temperature stages, are also shown in fig. 3.11, and carefully arranged such that there is no contact among them. Another aspect to be noticed is that the arm allows the use of external radioactive sources through its series of Röntgen windows placed at the front of each shield. This turned out to be an important feature for this experiment, as it allowed the calibration of the detectors, and their testing, in a cryogenic environment with strong radioactive sources which could simply be removed afterwards.

3.4 Setup geometry and measurement

In order to measure the X-ray component of the calorimetric energy spectrum of ^{163}Ho EC decay, the D14E (i.e. the ^{163}Ho-implanted chip presented in sec. 3.2.1) was glued to a copper platform, together with the 2-stage integrated SQUID read-out chip, as shown in fig. 3.12 b). Before the gluing, the platform was covered with $\sim$ 300 nm of Nb, in order to provide a superconducting shielding against magnetic Johnson noise due to the electrons in copper. The copper platform for the D14E was designed to have the same size and shape of the maXs-30 platform, in such a way that these two could be put in a configuration with the two detectors facing each other. Two 1 mm wide slits were cut into the D14E platform, one separating the detector from the read-out chip, the other one (the one below the detector) was instead used for previous tests. The presence of the slit between the two chips reduces the thermal contact between them. The circuit board was designed in such a way that at least two of the holes for the screws were left free, allowing the fastening of the two platforms. The wires needed to operate the detectors were soldered on this circuit board and secured along the copper arm, to make sure there was no contact to the thermal shielding once the cryostat is closed.
The two "stripes" on the experimental platform to the sides of the detector, were intentionally not covered with Nb to allow the connection between the on-chip thermal bath and the copper of the platform through gold bonding wires. Figure 3.12 a) shows the maXs-30 on its holder, at the extremity of the arm. Besides the maXs-30 chip, other eight chips with four front-end SQUIDs each are glued to the copper platform. The electrical connections are done using aluminum bonding wires. The four green stripes drive the connections from the front-end read-out to the amplifier SQUIDs circuit boards mounted on the four sides of the arm, as shown in fig. 3.13 and in fig. 3.12 c), in which the circuit boards are covered by their protective masks.

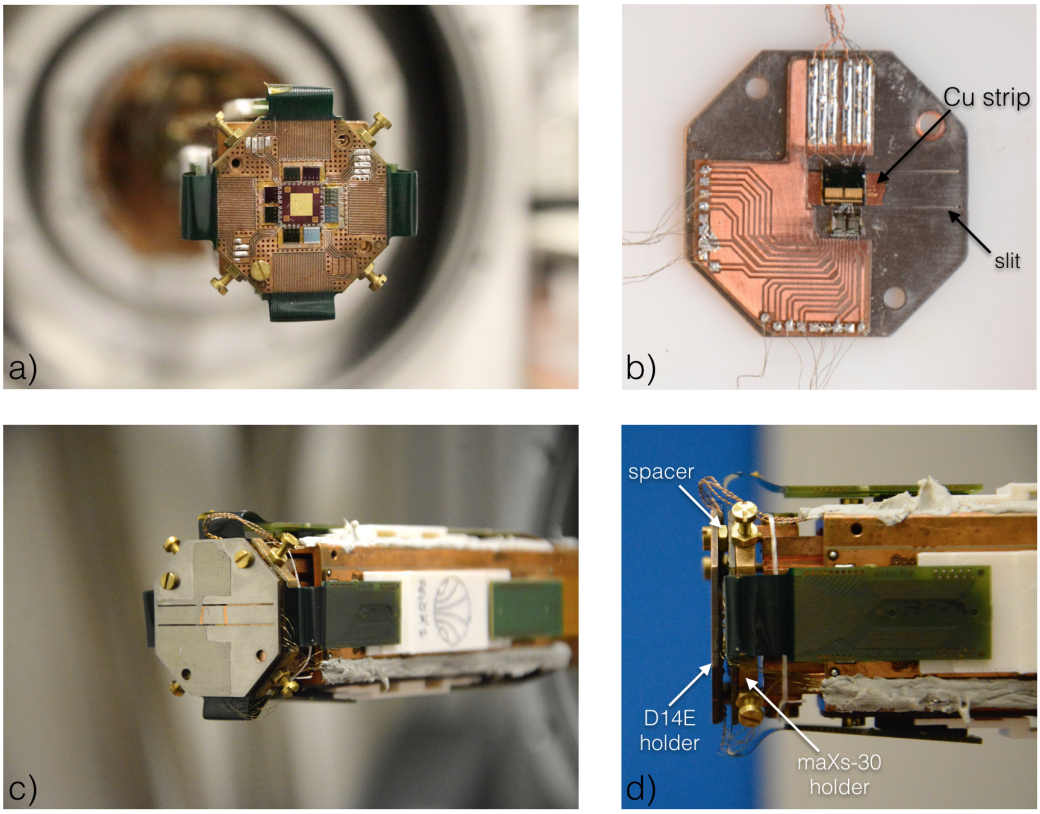

Figure 3.12: These photographies of the experimental setup show a) the maXs-30 on its holder, b) the D14E glued to a copper platform, together with the 2-stage integrated SQUID read-out chip, c) the green stripes driving the connections from the front-end read-out to the amplifier SQUIDs circuit boards, and d) a close-up on the spacing between the maXs-30 and the D14E.

In fig. 3.12 c) and d) one can see the D14E holder mounted in front of the maXs-30 holder. The screws and the separators/nuts, apart from fixing the two platforms to each other, also act as thermal contacts for the D14E to the cryostat arm. The position of the D14E on its platform was chosen in such a way that the active channels could correspond to the center of the maXs-30 pixel matrix, in order to maximize the solid angle covered by the maXs-30.
A schematics of the two detector platforms put in front of each other is given in fig. 3.14. The distance between the two detectors should be as small as possible to maximize the solid angle, provided that there is no physical contact. The two possible options shown in fig. 3.14 b) were defined by the size of the spacers and the available space inside the cryostat arm, and from the minimum achievable distance between the experimental holders, in order for the bonding wires of the two detectors not to touch each other. Taking

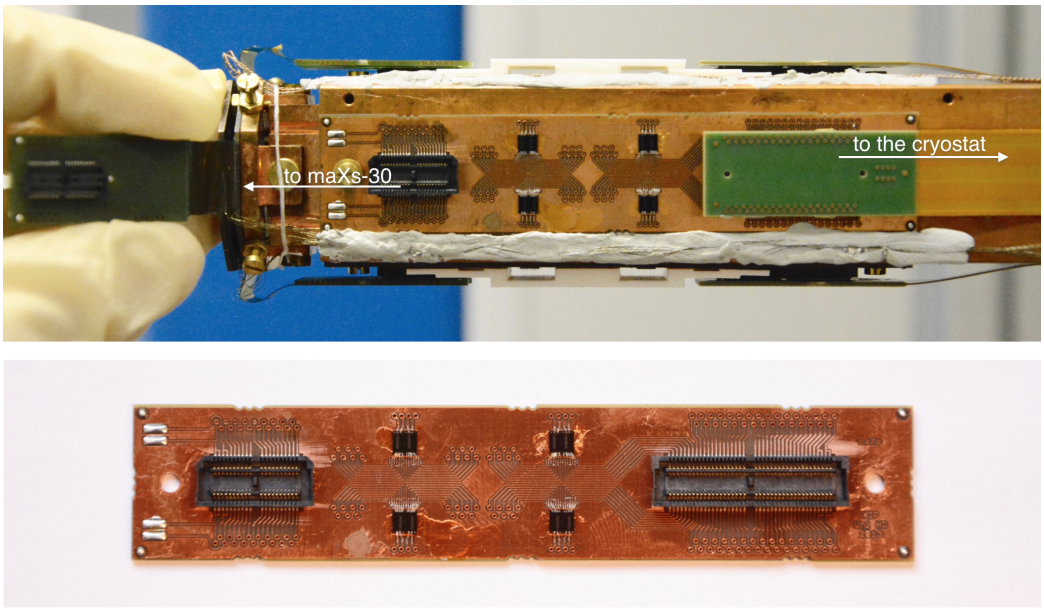

Figure 3.13: The amplifier SQUID read-out for the maXs-30. The SQUID array chips are connected to the front-end read-out of the maXs-30 in a 2-stage SQUID configuration, as described in sec. 3.1.2. On top, the arrays mounted on the cryostat are shown. In the bottom picture the single circuit board can be seen.

into account these factors, it was possible to choose between 1.2 mm or 2.4 mm distance, namely the thickness or twice the thickness of the single spacer. The solid angle covered by the maXs-30 for the detection of the X-rays coming from the D14E ^{163}Ho-implanted absorbers depends on the distance between the two detectors, according to

$$\Omega_{\mathrm{maXs}} = 4 \arctan\left(\frac{\alpha\beta}{2\mathrm{d}\sqrt{4\mathrm{d}^2+\alpha^2+\beta^2}}\right), \tag{3.12}$$

where $\alpha = \beta$ are the sides of the maXs-30 pixel matrix, and d is the distance between the two detectors, as shown in the sketch in fig. 3.15. With $\alpha = 4$ mm, $\mathrm{d}_1 = 1.2$ mm and $\mathrm{d}_2 = 2.4$ mm, defining Ω as the total solid angle, one can find that the maXs-30 covers the following solid angles for the two detector distances:

$$\Omega_{\mathrm{maXs}}(\mathrm{d}_1) \simeq 26.3\%\,\Omega \qquad \Omega_{\mathrm{maXs}}(\mathrm{d}_2) \simeq 13.4\%\,\Omega \ . \tag{3.13}$$

If three weeks of data taking are assumed, and a branching ratio of $\sim 10^{-3}$ for the X-ray emission is considered [40], about 500 X-rays events are expected in case only one spacer is used, while about 250 events are expected in the

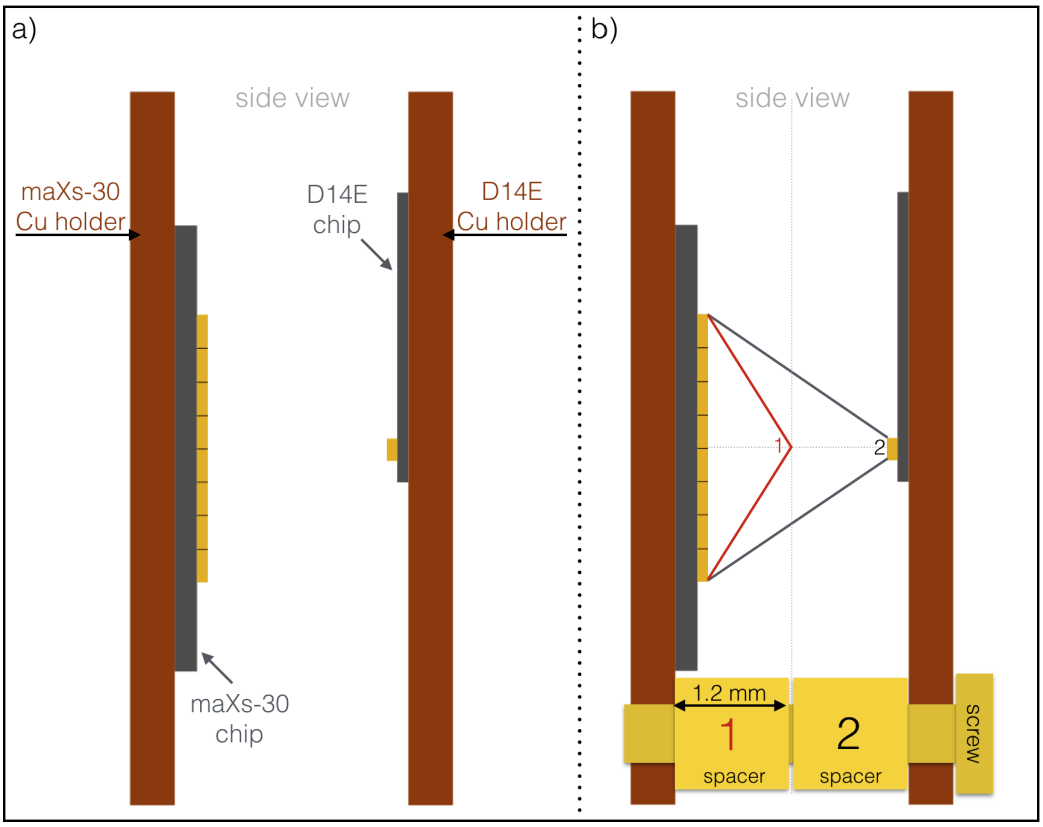

Figure 3.14: Schematics of the positioning of the D14E and the maXs-30.

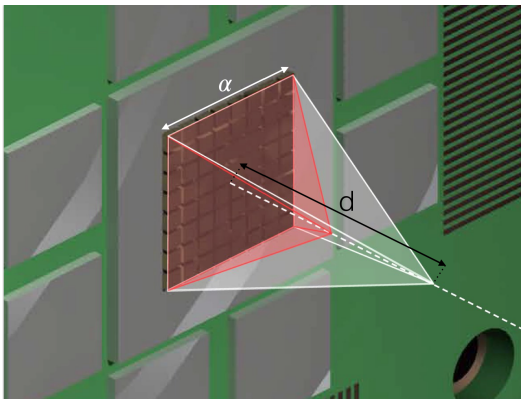

Figure 3.15: Sketch of the solid angle covered by the maXs-30 pixel matrix, as derived in eq. 3.13.

case of two spacers. For the present experimental setup it was finally possible to place only one spacer between the detector holders.

3.5 The Data Acquisition

Data was first collected in a 13 days cryostat run, during which a "long-term" measurement of the source chip was taken. Afterwards, an attempt to a coincidence measurement was made, during which several issues concerning the maXs-30 arose: due to thermal stress, three of the four field- and heater-lines connections were lost, leaving only half of the detector available for a measurement; of the remaining eight channels, again, the connections of only four of them survived the thermal stress, which is likely caused by small adjustment movements of the connectors during the cooling down of the cryostat; the noise level of these last channels only allowed trigger thresholds at the edge (or slightly above) of the energy of the MI line of ^{163}Ho.
The positive side about these aspects is that they can be improved in the short-term, with the design of new, more stable connectors for the cryostat, and with the production and testing of new maXs-30 chips and read-out, other than further searches for the optimal read-out settings. The setup placed at the end of the arm also suffered from temperature instabilities, for which a deeper investigation is needed.
However, the acquisition time dedicated to the spectrum of ^{163}Ho was fruitful. After several trials, it was possible to freeze-in a 30 mA field current in one of the four available pixels of the D14E, which for the M1 line showed pulses of about 350 mV at a temperature of about 15 mK. The analysis of this data is discussed in chap. 4.
The data acquisition system employed for the measurement, named PAQS (Parallel AcQuisition System), was developed by D. Hengstler [4] and is schematized in a simplified way in fig. 3.16. The voltage signals coming from the SQUID electronics are given as input to and processed by two 16-channel Struck SIS 3316 ADC modules. The online access to the data and the definition of the acquisition settings are available when the PAQS Launcher is started, which in turn starts the three following programs: the PAQS Acquisition Server, the PAQS Fitter and the PAQS GUI[5].
The Acquisition Server (AS) includes the ADC Interface, a virtual class containing all the ADC functions which were customized for the particular ADC device used in this case. The data flows from the ADC to the Interface, which can also get control input messages from the ADC itself, and get/send control messages from/to the GUI. Through the AS the raw data is both stored and sent to the Fitter.
The Fitter is started by the Launcher as many times as the number of read-out detector pixels. It contains an Averager, for performing the average of

[5]Graphic User Interface

a chosen set of good pulses and so to get an average sample pulse, in turn used by the virtual Fitter for the online fitting of the data. A Fast Fourier Transform (FFT) is also included in the Fitter, which allows a noise check for each pixel. A Fit File with the online fit data is written at this stage and stored by the Fitter, which also sends the data to the GUI Communication port. The GUI finally allows the user to interact with the read-out hardware, e.g. tuning the settings for the read-out, and to get an online preliminary data processing.
The synchronization of the D14E with the maXs-30 channels is doable offline thanks to a newly introduced high-resolution time-stamp assigned and stored into the Fit File for each pulse. A time window of the order of the detector rise-time is chosen in order to evaluate during the offline data analysis whether two events happened in coincidence or not.

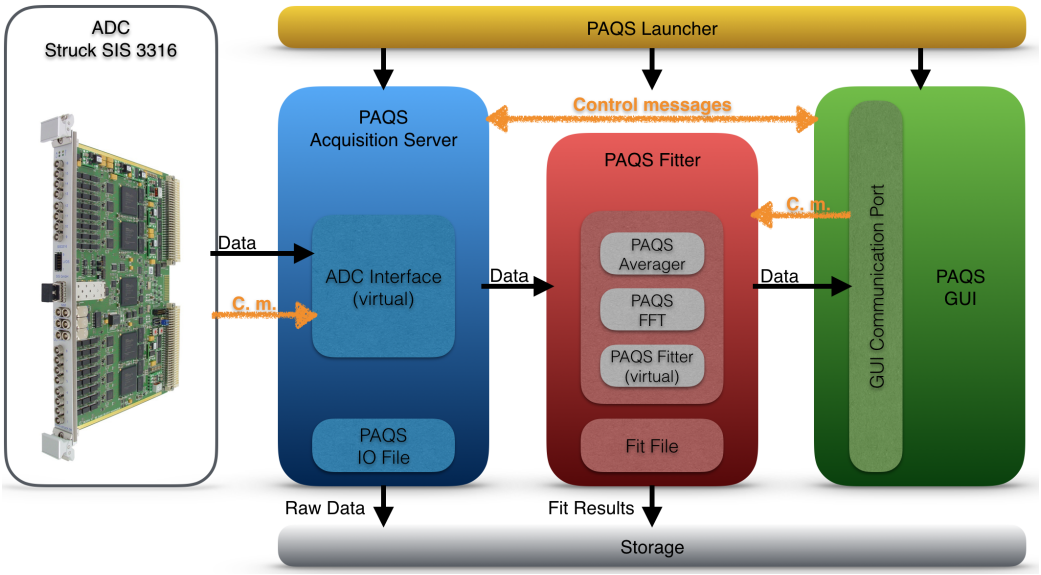

Figure 3.16: Diagram of the data-flow and data acquisition system. Courtesy of D. Hengstler [4].

Chapter 4

Results and discussion

4.1 Measurement of ^{163}Ho spectrum

The data discussed in this thesis was collected over 13 days within a cryostat run of about one month. During this run, one of the four available pixels with ^{163}Ho-implanted absorber was measured. The ^{163}Ho-source activity was 0.5 Bq.

4.1.1 Analysis

A total of 9 data files were acquired during the run, each file containing 60000 raw pulses. One of these data sets was analyzed, with the main results of the analysis discussed in the following.
A field current of $I_f = 30$ mA was frozen into the detector at an operating temperature $T_{op} \simeq 15$ mK. The temperature measured at the mixing chamber was $T_{mix} \simeq 12$ mK. At this temperature and for the used field current a pulse height of 360 mV was observed for the MI-line pulses. Only negative pulses were observable, meaning that the current was probably frozen in only one of the detector pixels.
Even though a pre-trigger offset (PTO) oscillation of about 1 mV was observed due to temperature instability of the detector platform positoned in front of the copper arm, the pulse shape was regular and did not change for different PTO ranges, as shown in fig. 4.1. The pulse shape of the average signal corresponding to an event of the NI-line was compared to the pulse shape of the average signal corresponding to an event of the MI-line, within a stable PTO range, and they also did not differ and showed an identical rise- and decay-time, as one can see from fig. 4.2, where the two pulses are shown for the two time windows of -4 - 8 and -0.6 - 0.6 μs. Nevertheless, a PTO cut was applied to the major jumps. A clear reason to explain the observed

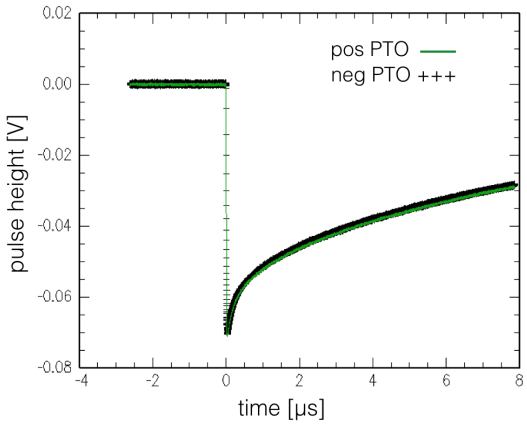

Figure 4.1: Comparison of two average N1-line pulses, picked from pulse groups in which the PTO had a positive or a negative value. Despite the PTO instability, the pulse shape did not change.

temperature oscillation could not be found yet, and further investigation in this direction is planned for the near future.
From fig. 4.2 (right) it is possible to see that the rise-time of the detector was $\leq$ 100 ns, in agreement with what expected according to the thermal link connecting the absorber to the sensor. The decay of a typical pulse is also characterized by a *nose*, corresponding to the "short" decay time of the pulse, due to the flow of the energy to the gold nuclei, and a "long" decay time showing the time necessary to the thermodynamical systems composing the MMC to reach the equilibrium base temperature.

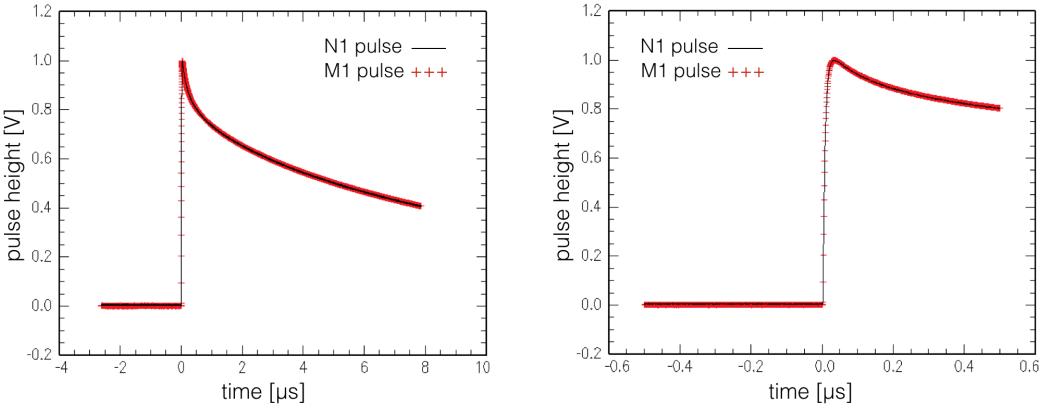

Figure 4.2: Left: comparison of the normalized average pulse shape for the MI and NI lines. The two shapes perfectly overlap. Right: close-up of the picture on the left, showing a zoom of the pulse shape into the rise-time interval. The pulse polarity was inverted here for plotting the averaged pulses.

A basic cut to the χ^2 was applied to the data, followed by a temperature-instability correction based on a linear fit of the distribution of the pulse amplitude of the MI-line pulses as a function of the PTO.

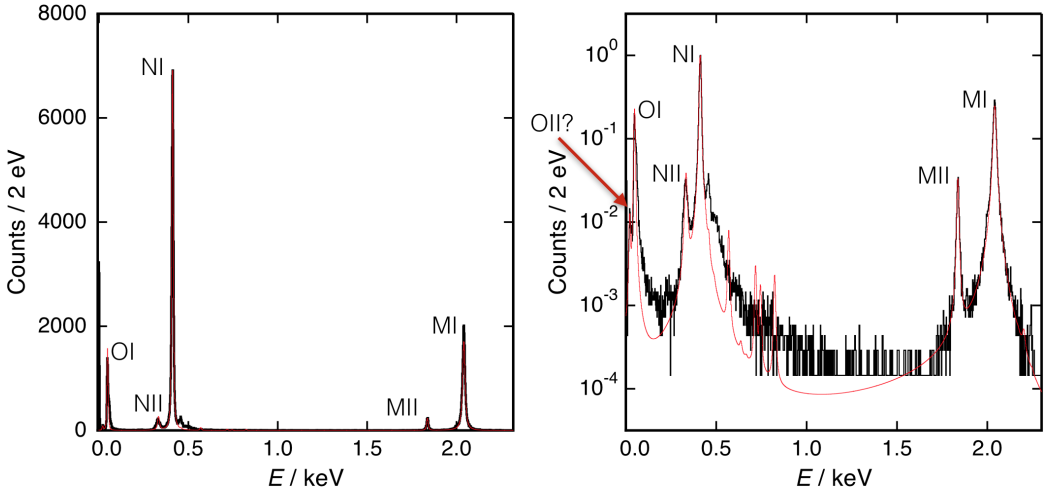

Figure 4.3: Left: ^{163}Ho spectrum obtained by the analysis of two of the collected data sets (black line), showing a good agreement with the simulated calorimetric spectrum theoretically predicted by Fässler (red line), for which a detector resolution of 7 eV was used. Right: logarithmic plot of the same spectrum. A peak at ∼21 eV can be seen, which is likely to be the previously unobserved OII-line.

The baseline resolution extracted with a gaussian fit of the distribution of the amplitudes of the untriggered detector output, chosen in a region where the PTO did not vary significantly, and shifted to 0 V for graphical convenience, is shown in fig. 4.4 (left). The amplitude distribution of the baselines was then fitted to a gaussian curve from which an energy resolution of $\Delta E^{b}_{\mathrm{FWHM}} = 1.1$ eV was extracted. The energy scale was defined via the calibration based on the analysis of the pulse amplitude for the different lines of the ^{163}Ho spectrum. The energy resolution for the signal was estimated at the NI-line, as shown in fig. 4.4 (right). The line shape is described by the Voigt function, the convolution between a gaussian and a Lorentzian function. The FWHM of the gaussian detector response can be extracted by knowing the intrinsic line width of the NI-line from the FWHM of the experimental data. From the fit, the FWHM of the measured NI-line is 11 eV and considering an intrinsic width of the NI-line of 5.4 eV one obtains a FWHM for the detector response of about 9 eV. The degradation of the energy resolution of the detector with respect to the baseline resolution could be due to slow temperature fluctuations of the experimental platform. More investigations are still required to clarify this point.

Also, the detector response to the deposited energy was linear up to the M-lines, as one can see from the linearity plot in fig. 4.5, where the the measured peak energies for each line are plotted against the theoretical energies,

and the quadratic non-linearity of the detector (red dotted line) is barely distinguishable from the plane bisector.
The spectrum of ^{163}Ho obtained from the analyzed data is shown in fig. 4.3. The linear (left) and the logarithmic (right) spectra are compared to the theoretical prediction of the spectral shape by Fässler [44], for which a detector resolution of 7 eV was assumed, and both show a good agreement with the first-order excitation lines. A deeper analysis of the collected data is currently ongoing, and it will shed light on these aspects. A further discussion of this results is only possible after a proper evaluation of the background level. The close-ups on the O-, N- and M-lines of the logarithmic plot of the measured spectrum are shown in fig. 4.6, fig. 4.7 respectively. From this pictures one can see how the theory can well reproduce the data at the one-hole peaks. On one hand, the data and the theory do not match for higher-order excitations, on the other hand, a peak with energy of 21 eV can be seen in the energy interval below the OI-line, which represents the first experimental observation of the OII-line. An excess of counts can be seen above the OI-line, maybe due to second order processes [45, 46, 44], as for the NI-line, which presents an excess structure at its high energy tale, as already pointed out in sec. 2.1.2.

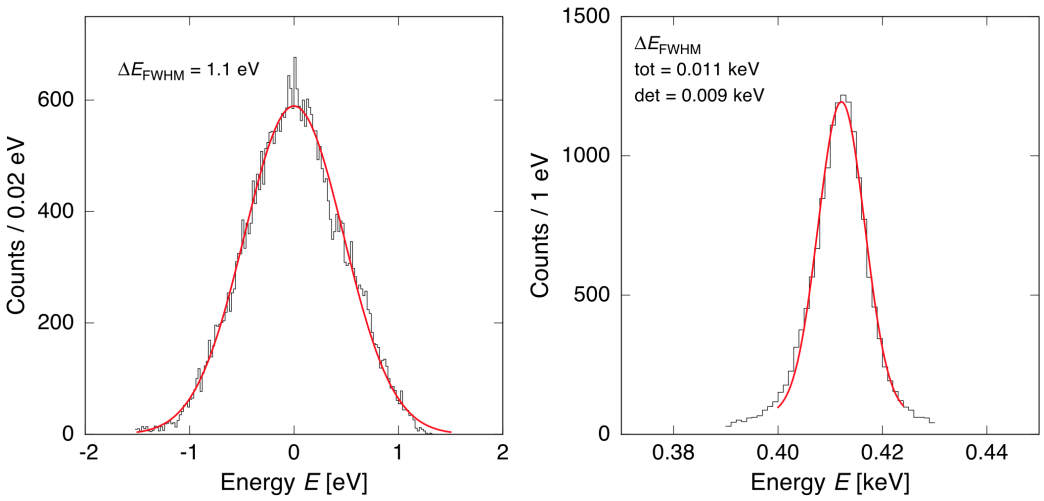

Figure 4.4: Left: amplitude distribution of the pulse baseline (black) fitted to a gaussian curve (red), from which an energy resolution $\Delta E^{b}_{FWHM} = 1.1$ eV was extracted. The PTO instability is here visible from the two separate peaks of the distribution around zero. Right: detector energy resolution calculated from the measured width of the NI line. The natural line shape is approximated to a gaussian, in order to implement a gaussian fit to the line. This way, an energy resolution of $\Delta E_{FWHM} = 9$ eV was extracted.

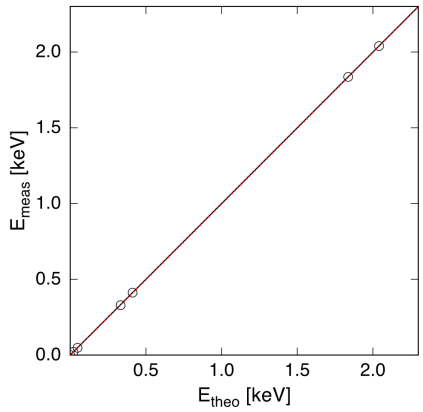

Figure 4.5: Linearity response of the detector in the ^{163}Ho spectrum energy range. The measured energies for the different lines are plotted against the theoretical energies. The quadratic fit (red) represents the non-linear behavior of the detector and is barely distinguishable from the plane bisector (black line).

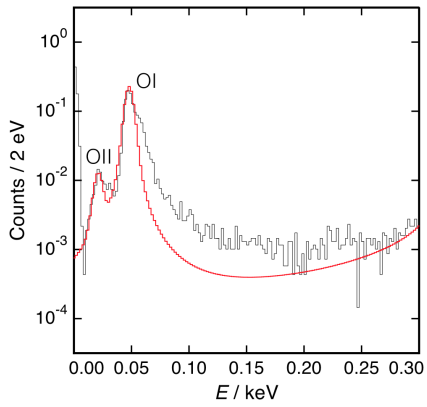

Figure 4.6: Zoom into the O-line region of the EC decay energy spectrum of ^{163}Ho . The OII-line might be here visible for the first time.

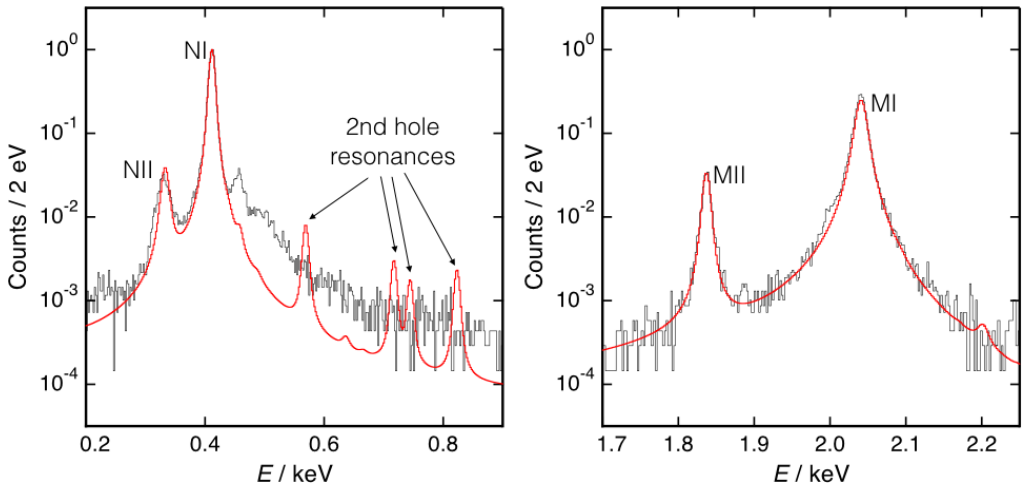

Figure 4.7: Zoom into the N-line region (left) and M-line region (right) of the EC decay energy spectrum of ^{163}Ho . The structure at the NI-line high energy tail which is not understood yet, also appears here. The second-hole excitations predicted by the theory are not visible. The origin of the small structure appearing at the lower energy slope of the MI-line could not be understood, on the other hand the expected excess of events at the MI peak is visible.

Conclusions

This thesis discussed for the first time a novel experimental approach to study the de-excitation modes of ^{163}Dy after electron capture in ^{163}Ho. The method proposed in this thesis consists of a coincidence measurement between X-ray events, emitted by a ^{163}Ho source placed about 100 nm below the surface of a high energy resolution detector, and the events occurring in the detector implanted with the ^{163}Ho source. The analysis of the two spectra as well as the analysis, for the coincident events, of the spectrum showing event per event the summed energy will provide theorists new interesting data which might shed light on the de-excitation process of ^{163}Dy.

For the detectors with the ^{163}Ho source two MMCs of the design maXs-20 have been used. Each of these detectors has two gold absorbers connected to a Au:Er paramagnetic sensor, in turn read out by a spiral-shaped pick-up coil. On each absorber ^{163}Ho was implanted at ISOLDE. After the implantation, 100 nm of Au were deposited on the absorber surface to protect the ^{163}Ho. This gold layer allows with good probability the escape of photons in the range between 1.3 keV and 2 keV where the emission due to fluorescence, as expected for the radiative de-excitation of ^{163}Dy, is higher. For the measurement of the X-ray spectrum a 2D array of the design maXs-30 was used. This array is characterized by 8×8 absorbers covering a surface of 4×4 mm^2. For the experimental setup developed in this thesis, the solid angle covered by the maXs-30 detector with respect to the position of the source was $\sim 26\%$ of the total solid angle.

During the first tests the detector containing the source was characterized. In particular, ^{163}Ho spectra from one of the four pixels were measured. The ^{163}Ho activity was 0.5 Bq. The detector was operated at 15 mK on a experimental platform positioned at the end of a copper arm connected to the mixing chamber of a commercial dilution refrigerator. The experimental platform for the source detector was designed to be coupled to the experimental platform of the maXs-30, in a way that between the source detector and the maXs-30 itself the distance resulted to be minimal.

A sub-set of the data acquired during 13 measuring days was analyzed in this

thesis. The energy resolution of the source detector was $\Delta E_{FWHM} \sim 8$ eV. This allowed for the first time to resolve, with a calorimetric measurement, the OII-line corresponding to the capture of $5p_{1/2}$ electrons. The peak energy of the line is $E_{OII} = 21$ eV, which is lower than the binding energy of the 5p1/2 electron in ^{163}Dy, as expected due to the presence of the one 4f electron in ^{163}Dy after the decay.
Due to the low activity of the source and to the fact that only a small fraction of the 64 pixels of the maXs-30 were actually working, the coincidence measurement was not possible. A ^{163}Ho activity of the order of 10 Bq would be required to perform such an experiment.
The success of the first measurement of the ^{163}Ho spectrum from the source detector positioned in front of the maXs-30 array demonstrated the suitability of the developed detector setup to perform the coincidence measurement of the X-ray spectrum following the electron capture process in ^{163}Ho. In the next future MMC detectors with higher activity will be prepared. These detectors could simply replace the present source detector and being used in the developed detector setup. A better understanding of the de-excitation processes in ^{163}Dy will be of great importance to reduce systematic uncertainties in the analysis of the endpoint region of the ^{163}Ho spectrum in order to search for deviations due to a finite neutrino mass at a sub-eV level.

Appendix: physical properties of the sensor material Au:Er

This summary of the physical properties of the sensor material Au:Er is primarily based upon and partly reproduced from the explanations in [77, 78, 58] and is added for the convenience of the reader. Other sources are cited throughout the text.

Properties of Erbium in Gold

Erbium in low concentrations forms a solid solution with gold [79]. Erbium in the 3+ state substitutes for Au at regular fcc lattice sites giving three of its electrons to the conduction band. The Er^{3+} ion has the electron configuration $[Kr]4d^{10}4f^{11}5s^25p^6$. The paramagnetic behavior results from the partially filled $4f$ shell, having a radius of only about 0.3 Å and located deep inside the outer $5s$ and $5p$ shells. For comparison, the ionic radius of Er^{3+} is about 1 Å, as is depicted in figure 4.8. Because of this the influence of the crystal field is greatly reduced and the magnetic moment can be calculated from the orbital angular momentum $\boldsymbol{L}$, the spin angular momentum $\boldsymbol{S}$ and the total angular momentum $\boldsymbol{J}$, which are derived according to Hund's rules. To a good approximation the admixture of excited electronic states can be neglected and the magnetic moment $\boldsymbol{\mu}$ can be written as

$$\boldsymbol{\mu} = g_J \boldsymbol{J} \tag{4.1}$$

with the Landé factor

$$g_J = 1 + \frac{J(J+1) + S(S+1) - L(L+1)}{2J(J+1)} \quad . \tag{4.2}$$

For Er^{3+}, $L = 6$, $S = {}^3/_2$, $J = {}^{15}/_2$ and $g_J = {}^6/_5$. In dilute Au:Er samples the magnetization can indeed be characterized by (4.1) at temperatures

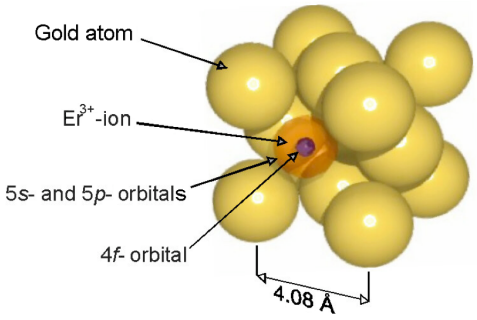

Figure 4.8: Schematic of a lattice section of the Au:Er-alloy. The Er^{3+}-ions take regular sites within the Au-lattice. The only partially filled Er $4f$-shell lies deep within the ion.

above about 100 K [80]. At lower temperatures it is necessary to include crystal field effects in the description. The crystal field with fcc symmetry lifts the sixteen-fold degeneracy of the Er^{3+} ground state, splitting it into a series of multiplets (one Γ_6 and one Γ_7 doublet and three Γ_8 quartets). The lowest lying multiplet is a Γ_7 Kramers doublet. At sufficiently low temperatures and low magnetic fields the behavior of erbium in gold can be approximated as a two level system with effective spin $\tilde{S} = {}^1/_2$ with an isotropic g factor of $\tilde{g} = {}^{34}/_5$. This theoretical value has been confirmed by several ESR experiments (see, for example [81]). The magnitude of the energy splitting between the ground state doublet and the first excited multiplet (Γ_8 quartet) has been reported in different experiments [82, 83, 80, 84] to be between 11 K and 19 K.

Figure 4.9 shows the magnetic susceptibility of Au doped with 600 ppm Er in the temperature range between 100 µK and 300 K. The data have been obtained in three different experiments [85, 78]. While the data at high temperatures ($T > 100$ K) are in good agreement with the Curie law for $J = {}^{15}/_2$ and $g_J = {}^6/_5$ there is an increasing deviation from the high temperature approximation below 100 K. This is a result of the depopulation of the multiplets with higher energies. At temperatures below about 1.5 K the data follow a Curie law once again, but with a reduced Curie constant in agreement with the effective spin $\tilde{S} = {}^1/_2$ and g factor $\tilde{g} = 6.8$ for the ground state doublet. At temperatures below 50 mK and in low magnetic fields such that saturation is unimportant ($\tilde{g}\mu_B B < k_B T$), the susceptibility becomes much less temperature dependent. This is a result of the influence of the exchange interaction between the magnetic moments. Finally, at a temperature of about 0.9 mK a maximum in the magnetic susceptibility of the 600 ppm sample is observed, which is the result of a transition to a spin glass state.

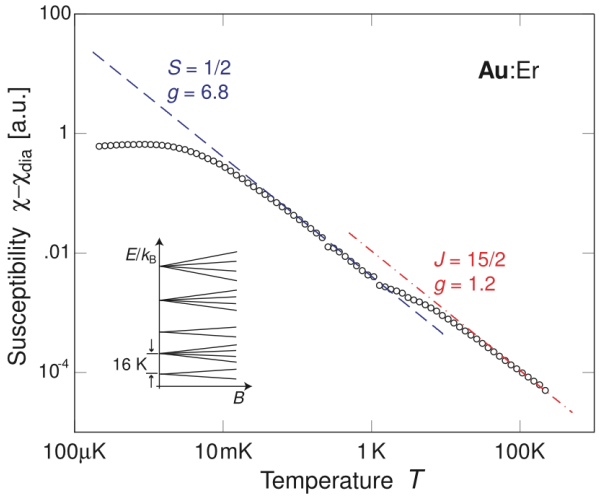

Figure 4.9: Paramagnetic contribution to the magnetic susceptibility of Au containing 600 ppm Er as a function of temperature. The *two straight lines* represent the Curie susceptibility assuming Er^{+3} ions in the Γ_7-groundstate doublet and Er^{+3} ions without crystal field splitting [78].

Thermodynamic characterization of non-interacting magnetic moments

The magnetization of the Au:Er alloy, due to the properties of the Er^{3+}-ions, can be used as a temperature information. And since the magnetization is a thermodynamic equilibrium property it can be accurately described theoretically. Starting from a suitable thermodynamic potential, like the free energy, with its full differential

$$\mathrm{d}F = -S\,\mathrm{d}T - VM\mathrm{d}B - \underbrace{p\,\mathrm{d}V}_{=0} \ , \tag{4.3}$$

and the volume change $\mathrm{d}V$ being negligibly small, the free energy F in statistical physics can be found to be

$$F = -Nk_\mathrm{B}T\ln z \ , \tag{4.4}$$

being a function of the number of magnetic moments N, the Boltzmann constant $k_\mathrm{B} = 1.381 \cdot 10^{-23}\,{}^\mathrm{J}/_\mathrm{K}$ and the canonical partition function:

$$z = \sum_i \mathrm{e}^{-\frac{E_i}{k_\mathrm{B}T}} \ , \tag{4.5}$$

with E_i being the energy eigenstates available to one magnetic moment. This preparatory work (eq. 4.3-4.5) can now be used to calculate the properties necessary to estimate the performance as a thermometer of our system,

namely the heat capacity C, the magnetization M and its change with temperature ${}^{\partial M}/_{\partial T}$:

$$C = \frac{N}{k_\mathrm{B} T^2} \left\{ \left\langle E^2 \right\rangle - \left\langle E \right\rangle^2 \right\} \ , \tag{4.6}$$

$$M = -\frac{N}{V} \left\langle \frac{\partial E}{\partial B} \right\rangle \ , \tag{4.7}$$

$$\frac{\partial M}{\partial T} = \frac{N}{V k_\mathrm{B} T^2} \left\{ \left\langle E \, \frac{\partial E}{\partial B} \right\rangle - \left\langle E \right\rangle \left\langle \frac{\partial E}{\partial B} \right\rangle \right\} \ . \tag{4.8}$$

This general theory on magnetic moments will now be applied to the case of ${}^{3+}$Er ions in gold. In the previous section 4.1.1 it was shown that at low temperatures only two alignments are possible for the magnetic moments of the ions in an external magnetic field B. The matching energy eigenvalues are

$$E_{m_{\tilde{\mathrm{S}}}} = m_{\tilde{\mathrm{S}}} \tilde{g} \mu_\mathrm{B} B \ , \tag{4.9}$$

with $m_{\tilde{\mathrm{S}}} = \pm {}^1/_2$ being the z-component of the quasi-spin, $\tilde{g} = 6.8$ the effective isotropic Landé factor of the Γ_7 Kramers doublet, $\mu_\mathrm{B} = 9.274 \cdot 10^{-24}\,\mathrm{Am}^2$ the Bohr magneton and B the absolute value of the magnetic field. Now the properties from eq. 4.6–4.8 can be calculated, leading to the well established Schottky anomaly

$$C_\mathrm{Z} = N k_\mathrm{B} \left(\frac{E}{k_\mathrm{B} T} \right)^2 \frac{\mathrm{e}^{E/k_\mathrm{B} T}}{(\mathrm{e}^{E/k_\mathrm{B} T} + 1)^2} \tag{4.10}$$

for the heat capacity that is depicted in fig. 4.10 and shows a characteristic maximum if the thermal energy $k_\mathrm{B} T$ is about half the energy splitting $\Delta E = g_{\tilde{S}} \mu_\mathrm{B} B$.
Calculating the magnetization of the Au:Er alloy in a similar fashion results in

$$M = \frac{N}{V} \tilde{S} \tilde{g} \mu_\mathrm{B} \mathcal{B}_{\tilde{S}}(h) \tag{4.11}$$

with the Brillouin function

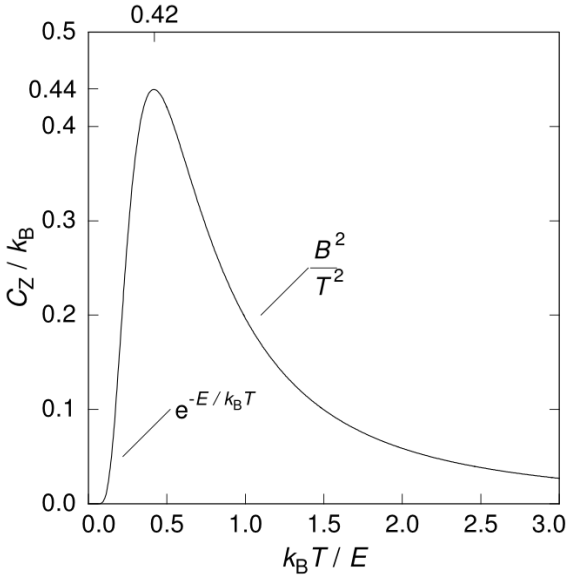

Figure 4.10: Heat capacity C of a two-level system with an energy splitting of $\Delta E = \tilde{g}\mu_{\mathrm{B}}B$ as a function of the reduced temperature ${}^{k_{\mathrm{B}}T}/_{\Delta E}$. The approximations for $T \ll {}^{E}/_{k_{\mathrm{B}}}$ and $T \gg {}^{E}/_{k_{\mathrm{B}}}$ are also shown.

$$\mathcal{B}_{\tilde{S}} = \frac{2\tilde{S}+1}{2\tilde{S}} \coth\left[\frac{(2\tilde{S}+1)h}{2\tilde{S}}\right] - \frac{1}{2\tilde{S}} \coth\left[\frac{h}{2\tilde{S}}\right] \tag{4.12}$$

and its argument

$$h = \frac{\tilde{S}\tilde{g}\mu_{\mathrm{B}}B}{k_{\mathrm{B}}T} \quad . \tag{4.13}$$

Fig. 4.11 depicts the Brillouin function in the appropriate case of $\tilde{S} = {}^{1}/_{2}$ that shows the qualitative shape of the magnetization. The maximum value is defined by the density of magnetic ions ${}^{N}/_{V}$ and the maximum z component of the magnetic moment $\tilde{S}\tilde{g}\mu_{\mathrm{B}}$. The field and temperature dependence enters through the argument of the Brillouin function in the ratio ${}^{B}/_{T}$. At low temperatures and respectively high fields ($h \gg 1$) the magnetization saturates because all magnetic moments are aligned with the external field, while in the opposite case ($h \ll 1$) the magnetization enters a quasi linear regime known as Curie's law.

Thermodynamic characterization of interacting magnetic moments

While the assumption of non-interacting spins is sufficient for a qualitative description of the magnetic behavior of Au:Er, it is inadequate for a quantita-

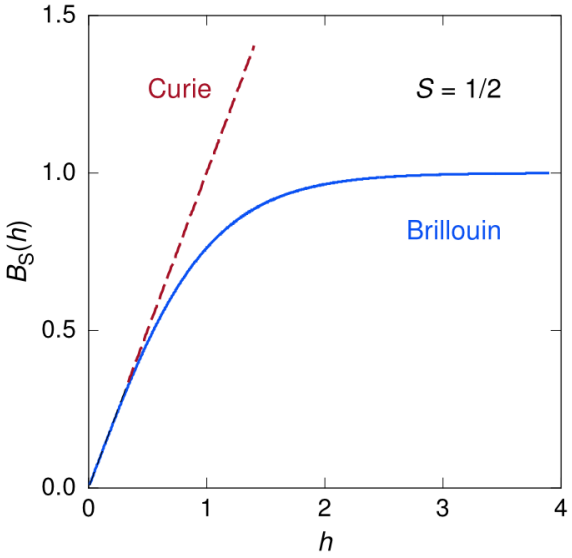

Figure 4.11: Brillouin function $\mathcal{B}_{1/2}(h)$ with the Curie approximation for $h \ll 1$. It shows the qualitative progression of the magnetization in a $\tilde{S} = {}^1/_2$ system in the approximation of non-interacting magnetic moments.

tive analysis. To calculate the magnetic response of Au:Er both the magnetic dipole-dipole interaction and the indirect exchange interaction between the spins must be taken into account.

Dipole-dipole interaction

The interaction of two paramagnetic ions at the positions $\boldsymbol{r}_i$ and $\boldsymbol{r}_j$ through their respective magnetic moment $\boldsymbol{\mu}_{i/j}$ enters the system's Hamiltonian with the following additional term:

$$H_{ij}^{\text{dipole}} = \frac{\mu_0}{4\pi}\frac{1}{r_{ij}^3}\left\{\boldsymbol{\mu}_i \cdot \boldsymbol{\mu}_j - 3(\boldsymbol{\mu}_i \cdot \hat{\boldsymbol{r}}_{ij})(\boldsymbol{\mu}_j \cdot \hat{\boldsymbol{r}}_{ij})\right\} \quad . \tag{4.14}$$

The quantity $\hat{\boldsymbol{r}}_{ij}$ represents the unit vector in the direction $\boldsymbol{r}_i - \boldsymbol{r}_j$ and r_{ij} the distance between the magnetic moments.
Because of the isotropy of the Γ_7 ground state doublet, the dipole-dipole interaction can be expressed in terms of the effective spins $\widetilde{\boldsymbol{S}}_i$ and $\widetilde{\boldsymbol{S}}_j$

$$H_{ij}^{\text{dipole}} = \Gamma_{\text{dipole}}\frac{1}{(2k_{\text{F}}r_{ij})^3}\left\{\widetilde{\boldsymbol{S}}_i \cdot \widetilde{\boldsymbol{S}}_j - 3\left(\widetilde{\boldsymbol{S}}_i \cdot \hat{\boldsymbol{r}}_{ij}\right)\left(\widetilde{\boldsymbol{S}}_j \cdot \hat{\boldsymbol{r}}_{ij}\right)\right\} \tag{4.15}$$

with prefactor $\Gamma_{\text{dipole}} = ({}^{\mu_0}/_{4\pi})\,(\tilde{g}\mu_{\text{B}})^2\,(2k_{\text{F}})^3$ and $k_{\text{F}} = 1.2 \cdot 10^{10}\,\text{m}^{-1}$ being the Fermi wave vector of the gold conduction electrons[1].

[1]The Fermi wave vector has been introduced artificially here to simplify the quantitative comparison with the indirect exchange interaction discussed later.

RKKY interaction

The exchange interaction of the localized $4f$ electrons of the erbium ions with the gold conduction electrons gives rise to an additional interaction between the erbium ions, the indirect exchange or Ruderman-Kittel-Kasuya-Yosida (RKKY) interaction. Expressed in terms of the effective spin, the RKKY interaction between two erbium spins can be written as

$$H_{ij}^{\mathrm{RKKY}} = \Gamma_{\mathrm{RKKY}} \, (\widetilde{\boldsymbol{S}}_i \cdot \widetilde{\boldsymbol{S}}_j) \, F(2k_{\mathrm{F}} r_{ij}) \tag{4.16}$$

with the function $F(2k_{\mathrm{F}} r_{ij})$ being

$$F(2k_{\mathrm{F}} r_{ij}) = \frac{1}{(2k_{\mathrm{F}} r_{ij})^3} \left[\cos(2k_{\mathrm{F}} r_{ij}) - \frac{1}{2k_{\mathrm{F}} r_{ij}} \sin(2k_{\mathrm{F}} r_{ij}) \right] \tag{4.17}$$

and prefactor Γ_{RKKY} given by

$$\Gamma_{\mathrm{RKKY}} = \mathcal{J}^2 \, \frac{4 V_0^2 m_{\mathrm{e}}^* k_{\mathrm{F}}^4}{\hbar^2 (2\pi)^3} \, \frac{\widetilde{g}^2 (g_J - 1)^2}{g_J^2}. \tag{4.18}$$

Here $\mathcal{J}$ denotes the coupling energy between the localized spins and the conduction electrons, V_0 is the volume of the elementary cell and m_{e}^* is the effective mass of the conduction electrons. The expression for the RKKY interaction given above is derived under the assumption that the mean free path of the electrons is larger than the mean distance between the localized erbium ions. In principle, it is possible that the RKKY interaction is reduced due to a finite coherence length λ of the spin polarization of the conduction electrons. In this case an additional factor $\mathrm{e}^{-r/\lambda}$ would appear in (4.16). However, for Au:Er with suitable erbium concentrations for its main application in low temperature metallic magnetic calorimeters (MMCs), the mean free path of the conduction electrons is always much larger than the mean separation of the erbium ions[2]. The fact that both the dipole-dipole interaction and the RKKY interaction are proportional to $1/r_{ij}^3$ allows us to compare their relative strength by a dimensionless parameter which is defined as the ratio of the two pre-factors

$$\alpha = \frac{\Gamma_{\mathrm{RKKY}}}{\Gamma_{\mathrm{dipole}}} \ . \tag{4.19}$$

[2]In measurements of the residual resistivity of dilute $\mathrm{Au}_{1-x}\mathrm{Er}_x$ alloys $\varrho = x\, 6.7 \times 10^{-6}\,\Omega\,\mathrm{m}$ was found [86, 87], and one can conclude that the mean free path of the conduction electrons is about 4000 Å for an erbium concentration of $x = 300\,\mathrm{ppm}$.

Using this parameter α the coupling energy $\mathcal{J}$ can be expressed as[3]

$$\mathcal{J} \simeq \sqrt{\alpha}\, 0.145 \text{ eV} \ . \tag{4.20}$$

Numerical calculation of the thermodynamical properties

A determination of the heat capacity and magnetization of a system of randomly distributed, interacting erbium spins requires a numerical calculation. There is a number of ways to perform this kind of calculation in the framework of a mean-field approximation. The method that requires the least amount of CPU time assumes the specific form of the mean field distribution that has been derived by Walker and Walstedt [88, 89] for magnetic moments randomly distributed in a continuous medium. These authors showed that this analytic representation of the mean field distribution agrees well with numerically calculated mean field distributions.

An alternative approach is to write down the Hamiltonian for a cluster of interacting, randomly distributed spins on the Au lattice and obtain the eigenvalues of the cluster. This process is repeated for a large number of configurations of randomly positioned spins with the heat capacity and magnetization obtained by averaging. Since this process delivers the more accurate results and is currently used to determine the Au:Er behaviour theoretically it will be explained in more detail in the following.

The basis for this approach is a cubic lattice segment of the gold fcc-lattice, typically with an edge length of ten to twenty lattice constants, depending on the simulated spin concentration. Additionally, quasi-periodic boundary conditions are assumed, repeating the cube four times in every direction in space. On this lattice segment $n = \text{const}$ spins are randomly distributed. For each configuration the Hamiltonian matrix is constructed. It includes the interaction of the magnetic moments with the external magnetic field (Zeeman interaction) and the dipole-dipole and RKKY interaction in between spin pairs.

In the basis $\mid S_1, S_2, \ldots, S_{n_{\max}} \rangle$ with the spin eigenvalues $S_i \in \{|\uparrow\rangle, |\downarrow\rangle\}$ and $\boldsymbol{B} = (0, 0, B_z)$, the Hamiltonian of two spins $\boldsymbol{S}_1$ und $\boldsymbol{S}_2$ at positions $\boldsymbol{r}_1$ und

[3]The value of $\mathcal{J}$ given by (4.20) refers to the definition of the exchange energy between a localized spin $\boldsymbol{S}$ and a free electron $\boldsymbol{s}$ being $H = \mathcal{J}\boldsymbol{s} \cdot \boldsymbol{S}$. The definition $H = 2\mathcal{J}\boldsymbol{s} \cdot \boldsymbol{S}$ is often found in literature, leading to values of the parameter $\mathcal{J}$ smaller by a factor of two.

$\boldsymbol{r}_2$ takes the following form:

$$\mathcal{H} = \mathcal{H}^{\text{Zeeman}} + \mathcal{H}^{\text{dipole}} + \mathcal{H}^{\text{RKKY}}, \text{ with} \tag{4.21}$$

$$\mathcal{H}^{\text{Zeeman}} = -\tilde{g}\mu_{\text{B}}(S_{z\,1} + S_{z\,2})B_z \ , \tag{4.22}$$

$$\mathcal{H}^{\text{dipole}} = \frac{\mu_0}{4\pi}\frac{(\tilde{g}\mu_{\text{B}})^2}{r^3}\Big(\begin{array}{lll} -(3\,\cos^2\theta - 1) & (\ S_{z\,1}S_{z\,2} & \ ) \\ +1\!/\!_4\,(3\cos^2\theta - 1) & (\ S_{+\,1}S_{-\,2} \ + \ S_{-\,1}S_{+\,2} & \ ) \\ -3\!/\!_2\,\sin\theta\cos\theta & (\ S_{z\,1}S_{+\,2} \ + \ S_{z\,2}S_{+\,1} & \ ) \\ -3\!/\!_2\,\sin\theta\cos\theta & (\ S_{z\,1}S_{-\,2} \ + \ S_{z\,2}S_{-\,1} & \ ) \\ -3\!/\!_4\,\sin^2\theta & (\ S_{+\,1}S_{+\,2} & \ ) \\ -3\!/\!_4\,\sin^2\theta & (\ S_{-\,1}S_{-\,2} & \ ) \end{array}\Big) \ , \tag{4.23}$$

$$\mathcal{H}^{\text{RKKY}} = \alpha\,\frac{\mu_0}{4\pi}(\tilde{g}\mu_{\text{B}})^2\,(2k_F)^3\Big(S_{z\,1}S_{z\,2} \ + \ \frac{1}{2}(S_{+\,1}S_{-\,2} + S_{-\,1}S_{+\,2})\Big)\,F(\rho) \tag{4.24}$$

and

$$F(\rho) = \rho^{-3}\left(\cos(\rho) - \frac{\sin(\rho)}{\rho}\right) \ , \rho = 2k_{\text{F}}r \ . \tag{4.25}$$

In this context θ is the angle between $\mathbf{B}$ and $\hat{\mathbf{r}} = \frac{\mathbf{r}_2 - \mathbf{r}_1}{|\mathbf{r}_2 - \mathbf{r}_1|}$. S_+ and S_- are the usual raising and lowering operators. The Hamiltonian matrix has the rank 2^n and therefore 2^{2n} elements. For reasons of clarity and comprehension the shown Hamiltonian is limited to two interacting magnetic moments:

$$\mathcal{H} = \begin{pmatrix} |\uparrow\uparrow\rangle & |\uparrow\downarrow\rangle & |\downarrow\uparrow\rangle & |\downarrow\downarrow\rangle \\ -D_2 + \frac{1}{4}R + 2Z & -D_1 & -D_1 & -D_3 \\ -D_1 & +D_2 - \frac{1}{4}R & +D_2 + \frac{1}{2}R & +D_1 \\ -D_1 & +D_2 + \frac{1}{2}R & +D_2 - \frac{1}{4}R & +D_1 \\ -D_3 & +D_1 & +D_1 & -D_2 + \frac{1}{4}R - 2Z \end{pmatrix} \tag{4.26}$$

with the variables

$$\underbrace{Z = -\frac{1}{2}\tilde{g}\mu_{\text{B}}B_{\text{z}}}_{\text{Zeeman}} \ , \qquad \underbrace{R = \alpha\,\frac{\mu_0}{4\pi}(\tilde{g}\mu_{\text{B}})^2(2k_{\text{F}})^3\,\text{F}(\rho)}_{\text{RKKY}} \text{, and}$$

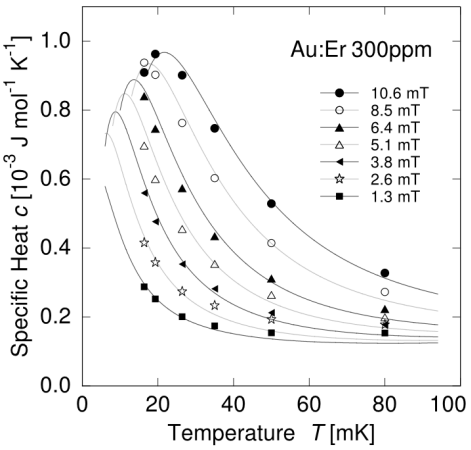

Figure 4.12: Specific heat of Au:Er with 300 ppm enriched ^{166}Er as a function of temperature at different applied magnetic fields. The *solid lines* are calculated numerically with a interaction parameter $\alpha = 5$ [90].

$$\left.\begin{aligned} D_1 &= \frac{3}{4}\frac{\mu_0}{4\pi}\frac{\tilde{g}\mu_\mathrm{B}}{r^3}\cos\theta\sin\theta, D_2 = \frac{1}{4}\frac{\mu_0}{4\pi}\frac{\tilde{g}\mu_\mathrm{B}}{r^3}(3\cos^2\theta - 1) \\ D_3 &= \frac{3}{4}\frac{\mu_0}{4\pi}\frac{\tilde{g}\mu_\mathrm{B}}{r^3}\sin^2\theta \end{aligned}\right\} \mathrm{dipole-dipole}$$

The parameters of the Monte-Carlo style simulation are chosen in the following way: $n = 6$ was chosen based on the minor improvement in accuracy for $n > 6$ and the available computation time. The lattice size was adjusted between 10 and 40 lattice constants to cover the usually used concentrations below 5000 ppm. These n spins are then randomly distributed across the lattice. Since the sensor material is normally available in a polycrystalline form also the orientation of the magnetic field is not previously defined and is chosen randomly and the angle θ is calculated accordingly for each pair of spins. Based on this randomly chosen configuration the Hamiltonian matrix is constructed for different values of the external magnetic field and the energy eigenvalues are calculated by numerically diagonalizing the matrix. With the energy eigenvalues the thermodynamic properties C, M, and $^{\partial M}/_{\partial T}$ can be calculated at any given temperature according to eq. 4.6–4.8. These calculation is repeated a large number of times and the results then averaged to get the final predictions for the thermodynamic properties. For the extreme cases, namely temperatures below 20 mK and concentrations above 1000 ppm the number of repetitions needs to be at least 10^4 to get stable results.
As an example we show in Fig. 4.12 the specific heat of an Au:Er sample having a concentration of 300 ppm of 97.8% enriched ^{166}Er. The temperature of the maximum in the specific heat depends on the magnitude of the external magnetic field as expected for a Schottky anomaly. However, the maximum is about twice as wide as for a non-interacting spin system. Calculations based

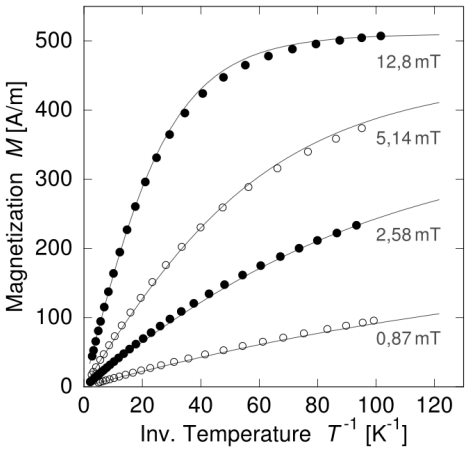

Figure 4.13: Magnetization of Au:Er with 300 ppm enriched ^{166}Er as a function of $^1/_T$ at different applied magnetic fields. The *solid lines* are calculated numerically with a interaction parameter $\alpha = 5$ [90].

on averaging over spin clusters provide a quantitative agreement assuming an interaction parameter α of 5. Although the calculated curves depend rather strongly on the choice of α, the value of $\alpha = 5$ should be viewed as an upper bound for the following two reasons. Firstly, the presence of ^{167}Er in the enriched sample leads to a slight additional broadening of the curve because of the hyperfine contribution of this isotope. Secondly, additional broadening results from a variation of the applied magnetic field, of about 10 to 15%, over the sample due to the geometry of the field coil.

The magnetization is plotted as a function of $^1/_T$ in Fig. 4.13 at several different magnetic fields for the 300 ppm sample. As in the case of the specific heat, the magnetization deviates for the behavior of isolated spins. The deviation is primarily due to the interaction between the magnetic moments, but a small contribution is also present due to the two reasons discussed above for the heat capacity. Again the data can be described satisfactorily by assuming an interaction parameter of $\alpha = 5$.

The magnetic properties of a weakly interacting spin system is perhaps most easily characterized in terms of the temperature dependence of the susceptibility given by the Curie-Weiss law, $\chi = {}^{\lambda}/_{(T+\theta)}$. The Curie constant λ is proportional to the concentration of the spins, as is the Weiss constant θ, which is a measure of strength of the interactions. For the Au:Er system, $\lambda = x\,5.3\,\mathrm{K}$ and $\theta = \alpha\,x\,1.1\,\mathrm{K}$, where x is the concentration of erbium ions.

Response Time

Au:Er can be used as temperature sensor in several ways, one of which is the use in low temperature detectors as proposed by Bandler et al. [91]. For this application not only the resolving power in temperature is important,

but also the response time since it directly influences the count rate of the detector.
The rise time is influenced by two factors. Firstly the heat needs to get to the temperature sensor and secondly the heat needs to influence the spins and create the magnetic signal.
In a usual setup for soft X-ray detection the temperature sensor is connected to a particle absorber made of electroplated pure gold with dimensions of $250\,\mu\text{m} \times 250\,\mu\text{m} \times 5\,\mu\text{m}$ with a residual resistivity ratio of ${}^{R_{300\,\text{K}}}/_{R_{4\,\text{K}}} \approx 15$. In such an absorber the thermalization process is governed by the thermal diffusion within the absorber since the down conversion to thermal energies is completed on the order of $\sim 0.5\,\text{ns}$ within a volume of a few cubic micrometers [90, 92]. The time scale for the diffusion process is mainly determined by the geometry of the absorber and the presence of defects such as grain boundaries and dislocations. If we assume the before mentioned geometry, the thermalization time, using the Wiedemann–Franz law, can be estimated to be on the order of 10 ns.
The time for the heat to flow from the absorber into the sensor is more difficult to estimate since this depends very much on the nature of the thermal connection between the two components. For sputter deposited or electroplated gold absorbers, as used in micro-fabricated detectors, the thermal contact is sufficiently strong that no degradation of the response time of the magnetic calorimeters due to the presence of the interface is observable.
Finally, the energy is shared with the magnetic moments in the sensor material giving rise of the signal. The response time of the spins is determined by the electron-spin relaxation time τ, which is described by the Korringa relation $\tau = {}^{\kappa}/_{T}$, where κ denotes the Korringa constant. For Au:Er the Korringa constant has been determined in ESR measurements at 1 K to be $\kappa = 7 \times 10^{-9}\,\text{Ks}$ [82]. This value of κ yields a spin-electron relaxation time of the order of 100 ns at the usual operation temperatures below 100 mK.
Therefore the electron-spin relaxation is the dominating factor in the response time of metallic magnetic calorimeters based on the sensor material Au:Er. This has successfully been shown in [76] where rise times as low as $\tau = 90\,\text{ns}$ have been observed and is shown in fig. 4.14 reproduced from the same source.
While this balance between heat diffusion and electron-spin relaxation works out well for small detectors for soft X-ray spectroscopy, it is off in case of larger detectors for hard X-ray or γ-ray spectroscopy. For detectors like maXs-200, described in [93, 94], with absorber dimensions of $2000\,\mu\text{m} \times 500\,\mu\text{m} \times 200\,\mu\text{m}$ the heat diffusion within the absorber is the governing factor in the response time. Depending on the interaction site in the absorber the heat can reach the sensor with different time patterns and create different detector responses [94]. These different pulse shapes will complicate

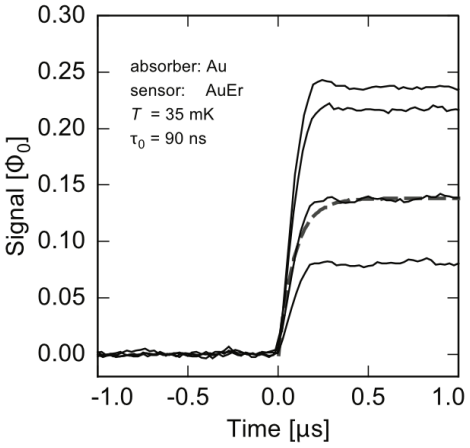

Figure 4.14: Detector signals in units of magnetic flux in the SQUID during the first micro-second after the absorption of X-rays of different energy in an MMC designed for soft X-ray spectroscopy [76]. The observed rise time $\tau = 90\,\mathrm{ns}$ is in agreement with what predicted by the Korringa relation described in the text.

the analysis and degrade the detector resolution. Therefore it is helpful to weaken the link between absorber and Au:Er sensor to allow the absorber to thermalize internally before allowing the heat to flow to the sensor creating consistent pulse shapes independent of the interaction site within the absorber.

Influence of Nuclear Spins

In the design of a magnetic calorimeter the possible influence of nuclear spins has to be considered. In the case of Au:Er there are two ways in which nuclei can affect the performance of the calorimeter. Firstly, the isotope ^{167}Er with nuclear spin $I = {}^{7}/_{2}$ influences the magnetization and the heat capacity due to its hyperfine interaction with the $4f$ electrons. Secondly, and more subtle, the 100% abundant ^{198}Au nuclei with small magnetic moment but large quadrupole moment may contribute to the specific heat if the nuclei reside at positions where the electric field gradient is of non-cubic symmetry. The hyperfine contribution of the erbium isotope ^{167}Er, if used in its natural abundance of 23 %, significantly reduces the magnetization signal and increases the specific heat of the sensor material. But since presently all metallic magnetic calorimeters use Au:Er that is depleted in ^{167}Er, it has no visible effect on the thermodynamic properties of the sensor material. The influence of ^{167}Er has nonetheless been investigated in [82] and its effect on metallic magnetic calorimeters has been summarized in e.g. [58].
Nuclei of the host metal can also influence the performance of an MMC. The ^{198}Au nuclei have spin $I = {}^{3}/_{2}$, a quadrupole moment of 0.547 barn and a magnetic moment sufficiently small to be neglected. In pure gold no contribution of the nuclear spins to the specific heat is expected at low fields, since the electric field of cubic symmetry does not lift the degeneracy

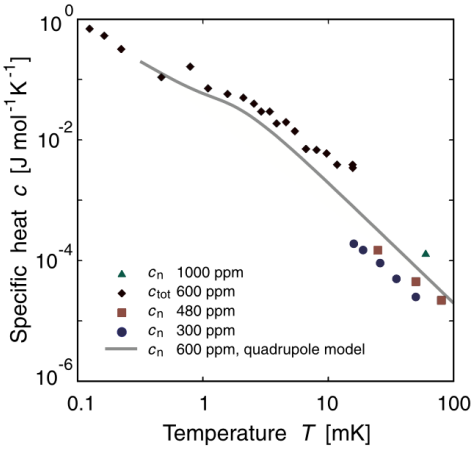

Figure 4.15: Contribution of the Au nuclei to the specific heat of Au:Er samples with different concentrations. The *solid line* represents a theoretical curve assuming a quadrupole splitting of 70 MHz for Au nuclei, which are nearest neighbors of Er. Here c_{tot} denotes the total specific heat and c_{n} the contribution of just the Au nuclei to the specific heat [90].

of the nuclear levels. However, for Au nuclei in the vicinity of an Er^{3+} ion the electric field gradient can be substantial and can split the nuclear levels. This results in an additional heat capacity. Fig. 4.15 shows the measured heat capacity of the Au nuclei as a function of temperatures for samples with different erbium concentrations. The data below 10 mK for the sample with 600 ppm is the total specific heat since at such low temperatures the contribution of the Au nuclei is substantially larger than that of all other degrees of freedom. The figure also shows a theoretical curve calculated assuming a quadrupole splitting of 70 MHz for Au nuclei in the immediate vicinity of erbium ions, the splitting decreasing for nuclei at larger distances in a manner similar to that measured in other dilute alloys such as Cu:Pt [95], Cu:Pd [96], and Gd:Au [97].

This unwanted contribution to the specific heat can only be eliminated by using a host material which has a nuclear spin $I \leq {}^1/_2$. At first glance it would appear desirable to use silver as a host material rather than gold since the two isotopes of silver (^{107}Ag and ^{109}Ag) both have nuclear spin $I = {}^1/_2$. However, the exchange energy $\mathcal{J}$ is 1.6 larger in silver than in gold as determined by ESR measurements[81]. Since the interaction parameter α is quadratic in the exchange energy $\alpha \propto \mathcal{J}^2$, as shown in [98] where $\alpha = 15$ was found, silver is not as attractive as a host material for a magnetic sensor. Just recently the interest in Ag:Er as sensor material has increased regardless, since MMCs have been used at even lower temperatures on the order of $T = 10$ mK where the additional specific heat in Au:Er might outweigh the stronger RKKY-interaction in Ag:Er.

Excess $^1/_f$-noise and AC-susceptibility

While investigating the noise behavior of metallic magnetic calorimeters with Au:Er as sensor material an excess noise contribution has been observed. The contribution was empirically found to be independent of temperature between 4.2 K and 20 mK and its noise power is proportional to the concentration of erbium ions in the sensor. It can be described by attributing a fluctuating magnetic moment with a spectral noise density of $S_m \simeq 0.1\,{}^{\mu_\mathrm{B}^2}/_{f^\eta}$ to each erbium ion, where μ_B is the Bohr magneton, f is the frequency and the exponent η takes values between 0.8 and 1 [99, 76]. The same behavior was also found in detectors based on the sensor material Ag:Er [98].
Similar behavior was found in several spin glasses (e.g. [100, 101]) and agreed with the fluctuation-dissipation theorem [102, 103] by comparing ac-susceptibility measurements with equilibrium magnetic noise of the same sample. But the amplitude of the $^1/_f$-noise decreased quickly for $T > T_\mathrm{c}$, where T_c is the transition temperature to the spin glass state, until not distinguishable from the background noise.
Au:Er also undergoes a transition to a spin glass but up to two orders of magnitude below the temperatures metallic magnetic calorimeters are usually operated at (see sec. 4.1.1). Therefore the $^1/_f$-noise should not be observable if explained by the same underlying cause. Recent investigations [104, 105] nonetheless found that the $^1/_f$-noise found in metallic magnetic calorimeters is in fact caused by the fluctuation-dissipation theorem, also by comparing the ac-susceptibility with equilibrium magnetic noise in a temperature range between 20 mK and 1 K for two Au:$\mathrm{Er}_{255\,\mathrm{ppm}}$ and Au:$\mathrm{Er}_{845\,\mathrm{ppm}}$ samples.

Bibliography

[1] K. Abe et al. (Super-Kamiokande Collaboration). "Solar neutrino results in Super-Kamiokande-III". In: *Phys. Rev. D* 83 (2011).

[2] B. Aharmim et al. (SNO Collaboration). "Combined analysis of all three phases of solar neutrino data from the Sudbury Neutrino Observatory". In: *Phys. Rev. C* 88 (2013).

[3] P. T. Springer, C. L. Bennett, P. A. Baisden. "Measurement of the neutrino mass using the inner Bremsstrahlung emitted in the electron-capture decay of ^{163}Ho ". In: *Phys. Rev. A* 35 (1987), pp. 679–689.

[4] D. Hengstler. "Doctoral Dissertation - *unpublished* - Low Temperature Physics group at Kirchhoff Institut für Physik, Heidelberg". In: (2017).

[5] W. Pauli. "On the earlier and more recent history of the neutrino". In: *Cambridge Monogr. Part. Phys. Nucl. Phys. Cosmol.* 14 (2000), pp. 1–22.

[6] J. Chadwick. "Possible existence of a neutron". In: *Nature* 129 (1932), p. 312.

[7] E. Fermi. "Tentativo di una teoria dell'emissione dei raggi "beta"". In: *La Ricerca Scientifica* Anno IV, Vol. II, N. 12 (1933).

[8] F. Perrin. In: *Comptes Rendus* 197 (1933), p. 1625.

[9] E. Fermi. "Versuch einer Theorie der β-Strahlen. I". In: *Zeitschrift für Physik* 88 (1933), pp. 161–177.

[10] E. Fermi. "Tentativo di una teoria dei raggi β". In: *Il Nuovo Cimento* 11 (1934), p. 1.

[11] F. Reines et al. "Detection of the free antineutrino". In: *Phys. Rev.* 117 (1960), p. 159.

[12] D. Decamp et al. (ALEPH Collaboration). "Determination of the number of light neutrino species". In: *Phys. Lett. B* 231 (1989), pp. 519–529.

[13] S. Weinberg. “A model of leptons”. In: *Phys. Rev. Lett.* 19 (1967), p. 1264.

[14] A. Salam. “Proc. of the 8th Nobel Symposium on "Elementary Particle Theory, Relativistic Groups and Analyticity" year 1968”. In: (1969), 367–377, edited by N. Svartholm.

[15] P. W. Higgs. “Broken symmetries, massless particles and gauge fields”. In: *Phys. Lett.* 12 (1964), pp. 132–133.

[16] F. Englert, R. Brout. “Broken symmetry and the mass of gauge vector mesons”. In: *Phys. Rev. Lett.* 13 (1964), p. 321.

[17] Y. Fukuda et al. (Super-Kamiokande Collaboration). “Evidence for oscillations of atmospheric neutrinos”. In: *Phys. Rev. Lett.* 81 (1998), p. 1562.

[18] B. T. Cleveland, T. Daily, R. Davis et al. “Measurement of the solar electron neutrino flux with the Homestake chlorine detector”. In: *The Astrophysical Journal* 496 (1998), pp. 505–526.

[19] Q. R. Ahmad et al. (SNO Collaboration). “Measurement of the rate of $\nu_e + d \rightarrow \mathrm{p} + \mathrm{p} + e^-$ interactions produced by ^{8}B solar neutrinos at the Sudbury Neutrino Observatory”. In: *Phys. Rev. Lett.* 87 (2001).

[20] Q. R. Ahmad et al. “Direct evidence for neutrino flavor transformation from neutral-current interactions in the Sudbury Neutrino Observatory”. In: *Phys. Rev. Lett.* 89 (2002).

[21] L. Wolfenstein. “Neutrino oscillations in matter”. In: *Phys. Rev. D* 17 (1978), p. 2369.

[22] S. P. Mikheev, A. Yu. Smirnov. “Resonance amplification of oscillations in matter and spectroscopy of solar neutrinos”. In: *Sov. J. Nucl. Phys.* 42 (1985), pp. 913–917.

[23] S. P. Mikheev, A. Yu. Smirnov. “Resonant amplification of ν oscillations in matter and solar-neutrino spectroscopy”. In: *Il Nuovo Cimento C* 9 (1986), pp. 17–26.

[24] T. Asaka, M. Shaposhnikov. “The nuMSM, dark matter and baryon asymmetry of the universe”. In: *Phys. Lett. B* 620 (2005), pp. 17–26.

[25] T. Asaka, S. Blanchet, M. Shaposhnikov. “The nuMSM, dark matter and neutrino masses”. In: *Phys. Lett. B* 631 (2005), pp. 151–156.

[26] F. Capozzi et al. “Neutrino masses and mixings: status of known and unknown 3ν parameters”. In: *Nucl. Phys. B* 00 (2016), pp. 1–14.

[27] I. Esteban et al. “Updated fit to three neutrino mixing: exploring the accelerator-reactor complementarity”. In: *arXiv:1611.01514 [hep-ph]* (2016).

[28] G. Steigman, D. N. Schramm, J. E. Gunn. “Cosmological limits to the number of massive leptons”. In: *Phys. Lett. B* 66 (1977), pp. 202–204.

[29] C. Patrignani et al., K. A. Olive (rev.) “Particle Data Group - Sum of neutrino masses”. In: *Chin. Phys. C* 40 (2016), p. 100001.

[30] M. Lattanzi (on behalf of the Planck collaboration). “Planck 2015 constraints on neutrino physics”. In: *Journal of Physics: Conference Series* 718 (2016).

[31] E. Majorana. “Teoria simmetrica dell’elettrone e del positrone”. In: *Il Nuovo Cimento* 14 (1937), pp. 171–184.

[32] A. Gando et al. (KamLAND-Zen Collaboration). “Search for Majorana neutrinos near the inverted mass hierarchy region with KamLAND-Zen”. In: *Phys. Rev. Lett.* 117 (2016).

[33] L. Winslow, R. Simpson. “Characterizing quantum-dot-doped liquid scintillator for applications to neutrino detectors”. In: *JINST* 7 (2012).

[34] C. Pagliaroli, F. Rossi-Torres, F. Vissani. “Neutrino mass bounds in the standard scenario for supernova electronic antineutrino emission”. In: *J. Astropart. Phys.* 33 (2010), pp. 287–291.

[35] V. Drexlin G.and Hannen, S. Martens, and C. Weinheimer. “Current direct neutrino mass experiments”. In: *Adv. in HEP* 2013 (2013), p. 39.

[36] C. Kraus et al. “Final results from phase II of the Mainz neutrino mass search in tritium β-decay”. In: *EPJC* 40 (2005).

[37] N. Aseev et al. “Upper limit on the electron antineutrino mass from the Troitsk experiment”. In: *Phys. Rev. D* 84 (2011).

[38] J. Angrik, T. Armbrust, A. Beglarian et al. “KATRIN design report 2004”. In: *Forschungszentrum Karlsruhe GmbH* (2005). URL: `https://publikationen.bibliothek.kit.edu/270060419`.

[39] A. De Rujúla. “Two old ways to measure the electron-neutrino mass”. In: *arXiv:1305.4857 [hep-ph]* (2013).

[40] E. J. McGuire. “Atomic M-shell Coster-Kronig, Auger and radiative rates, and fluorescence yields for Ca-Th”. In: *Phys. Rev. A* 6 (1972), p. 851.

[41] A. De Rújula, M. Lusignoli. “Calorimetric measurements of ^{163}Ho decay as tools to determine the electron neutrino mass”. In: *Phys. Lett. B* 118 (1982), pp. 429–434.

[42] P. A. Baisden et al. “Measurement of the half-life of ^{163}Ho ”. In: *Phys. Rev. C* 28 (1983), p. 337.

[43] S. Eliseev et al. “Direct measurement of the mass difference of ^{163}Ho and ^{163}Dy solves the Q-value puzzle for the neutrino mass determination”. In: *Phys. Rev. Lett.* 115 (2015).

[44] A. Faessler, F. Šmikovic. “Improved description of one- and two-hole excitations after electron capture in ^{163}Ho and the determination of the neutrino mass”. In: *Phys. Rev. C* 91 (2015).

[45] R. G. H. Robertson. “Examination of the calorimetric spectrum to determine the neutrino mass in low-energy electron capture decay”. In: *Phys. Rev. C* 91 (2015), p. 035504.

[46] A. De Rújula, M. Lusignoli. “The calorimetric spectrum of the electron-capture decay of ^{163}Ho. The spectral endpoint region”. In: *M. J. High Energ. Phys.* (2016).

[47] C. Hassel. “Doctoral Dissertation - *unpublished* - Low Temperature Physics group at Kirchhoff Institut für Physik, Heidelberg”. PhD thesis. 2018.

[48] K. Riisager. “On low-energy nuclear electron capture”. In: *J. Physics G* 14 (1988).

[49] E. Laegsgaard, J. U. Andersen, G. J. Beyer et al. “The capture ratio N/M in the EC beta decay of ^{163}Ho ”. In: *O. Keppler, ed., Proceedings of the 7-th International Conference on Atomic Masses and Fundamental Constants AMCO-7, nr. 26, in THD Schriftenreihe Wissenschaft und Technik* (1984), pp. 652–658.

[50] F. Hartmann, R. Naumann. “High temperature gas proportional detector techniques and application to the neutrino mass limit using ^{163}Ho ”. In: *Nucl. Inst. and Meth. in Phys. Res. A* 313 (1992), pp. 237–260.

[51] F. Gatti et al. “Calorimetric measurement of the ^{163}Ho spectrum by means of a cryogenic detector”. In: *Phys. Lett. B* 398 (1997), pp. 415–419.

[52] F. X. Hartmann, R. A. Naumann. “Observation of N and M orbital electron capture in the decay of ^{163}Ho ”. In: *Phys. Rev. C* 31 (1985), pp. 1594–1596.

[53] L. Gastaldo, K. Blaum, A. Doerr et al. “The Electron Capture ^{163}Ho experiment ECHo”. In: *J. of Low Temp. Phys.* (2014), pp. 1–9.

[54] B. Alpert et al. “HOLMES - The electron capture decay of ^{163}Ho to measure the electron neutrino mass with sub-eV sensitivity”. In: *EPJC* 75 (2015), p. 112.

[55] J. W. Engle, E. R. Birnbaum, H. R Trellue et al. “^{163}Ho for microcalorimetric electron capture spectroscopy to measure the mass of the neutrino”. In: *The future of neutrino mass measurements: terrestrial, astrophysical, and cosmological measurements in the next decade. Highlights of the νMass 2013 Workshop* (2013), pp. 54–57.

[56] M. Croce, E. Bond, A. Hoover et al. “Integration of radioactive material with microcalorimetric detectors”. In: *J. of Low Temp. Phys.* (2013), pp. 1–6.

[57] J. Fowler et al. “Microcalorimeter pulse analysis at very high count rates”. In: *15th Workshop on Low Temperature Detectors* (2013). URL: `http://conference.ipac.caltech.edu/ltd-15/`.

[58] Andreas Fleischmann, Christian Enss, and George M. Seidel. “Metallic Magnetic Calorimeters”. In: *Cryogenic particle detection*. Ed. by Christian Enss. Topics in Applied Physics 99. Springer Berlin Heidelberg, 2005. Chap. 4, pp. 151–216.

[59] J. Repp et al. “PENTATRAP: a novel cryogenic multi-Penning-trap experiment for high-precision mass measurements on highly charged ions”. In: *Appl. Phys. B* 107 (2012), pp. 983–996.

[60] C. Hassel et al. “Recent results for the ECHo experiment”. In: *J. Low Temp. Phys.* 184 (2016), pp. 910–921.

[61] A. Faessler et al. “Determination of the neutrino mass by electron capture in ^{163}Ho and the role of the three-hole states in ^{163}Dy ”. In: *Phys. Rev. C* 91 (2015).

[62] P. C.-O. Ranitzsch. “Doctoral Dissertation - *Development and characterization of metallic magnetic calorimeters for the calorimetric measurement of the electron capture spectrum of ^{163}Ho for the purpose of neutrino mass determination* - Low Temperature Physics group at Kirchhoff Institut für Physik, Heidelberg”. In: (2014).

[63] P. C.-O. Ranitzsch et al. “Development of metallic magnetic calorimeters for high precision measurements of calorimetric ^{187}Re and ^{163}Ho spectra”. In: *J. Low Temp. Phys.* 167 (2012).

[64] A. De Rújula. “A new way to measure neutrino masses”. In: *Nucl. Phys. B* 188 (1981), pp. 414–458.

[65] S. Yasumi and H. Maezawa (editors). "Study of the mass of the electron neutrino in Japan". In: *Nat. Lab. HEP, KEK Report 95-17* (1996).

[66] J. U. Andersen et al. "A limit on the mass of the electron neutrino: the case of ^{163}Ho ". In: *Phys. Lett. B* 113 (1982), pp. 72–76.

[67] B. Jonson et al. "Determination of the electron-neutrino mass from experiments on electron-capture beta decay". In: *Nucl. Phys. A* 396 (1983), pp. 479–493.

[68] K. Riisager et al. "The internal Bremsstrahlung spectra from the EC beta decay of ^{193}Pt and ^{163}Ho ". In: *Physica Scripta* 31 (1985), pp. 321–327.

[69] C. L. Bennett et al. "The X-ray spectrum following ^{163}Ho M electron capture". In: *Phys. Lett. B* 107 (1981), pp. 19–22.

[70] C. L. Bennett - V. Barger, D. Cline (ed.) "Neutrino mass and low energy weak interactions (Telemark)". In: (1984), p. 28.

[71] S. Yasumi et al. "The mass of the electron-neutrino from electron capture in ^{163}Ho ". In: *Phys. Lett. B* 334 (1994), pp. 229–233.

[72] J.-P. Porst et al. "Characterization and performance of magnetic calorimeters for applications in X-ray spectroscopy". In: *J. of Low Temp. Phys.* 176 (2014), pp. 617–623.

[73] M. Krantz. *Masterarbeit - Entwicklung, Mikrofabrikation und Charakterisierung von metallischen magnetischen Kalorimetern für die hochauflösende Röntgenspektroskopie hochgeladener Ionen - Low Temperature Physics group at Kirchhoff Institut für Physik, Heidelberg*. 2013.

[74] A. Fleischmann. "Magnetische Mikrokalorimeter: Hochauflösende Röntgenspektroscopie mit energiedispersiven Detektoren". PhD thesis. 2003. URL: `https://www.kip.uni-heidelberg.de/tt-detektoren/dissertationen`.

[75] J. Hubbel, S. Seltzer. *Tables of X-ray mass attenuation coefficients and mass enegy-absorption coefficients*. URL: `http://physics.nist.gov/xaamdi`.

[76] A. Fleischmann et al. "Metallic magnetic calorimeters". In: *AIP Conference Proceedings* 1185.1 (2009), pp. 571–578. DOI: `10.1063/1.3292407`.

[77] Jan Schönefeld. "Entwicklung eines mikrostrukturierten magnetischen Tieftemperatur-Kalorimeters zum hochauflösenden Nachweis von einzelnen Röntgenquanten". PhD thesis. Heidelberg University, 2000.

[78] Andreas Fleischmann. "Magnetische Mikrokalorimeter: Hochauflösende Röntgenspektroskopie mit energiedispersiven Detektoren". PhD thesis. Heidelberg University, 2003.

[79] P.E. Rider, K.A. Geschneider Jr., and O.D. McMaster. "Gold-rich rare-earth-gold solid solutions". In: *Transactions of the Metallurgical Society of AIME* 233 (Aug. 1965), pp. 1488–1496.

[80] Gwyn Williams and L. L. Hirst. "Crystal-Field Effects in Solid Solutions of Rare Earths in Noble Metals". In: *Physical Review* 185 (2 Sept. 1969), pp. 407–415. DOI: 10.1103/PhysRev.185.407.

[81] L. J. Tao et al. "Hyperfine Splitting of Er and Yb Resonances in Au: A Separation between the Atomic and Covalent Contributions to the Exchange Integral". In: *Physical Review B* 4 (1 July 1971), pp. 5–9. DOI: 10.1103/PhysRevB.4.5.

[82] M. E. Sjøstrand and G. Seidel. "Hyperfine resonance properties of Er^{3+} in Au". In: *Physical Review B* 11 (9 May 1975), pp. 3292–3297. DOI: 10.1103/PhysRevB.11.3292.

[83] D. Davidov et al. "Crystalline-Field Effects in the Electron-Spin Resonance of Rare Earths in the Noble Metals". In: *Physical Review B* 8 (8 Oct. 1973), pp. 3563–3568. DOI: 10.1103/PhysRevB.8.3563.

[84] W. Hahn, M. Loewenhaupt, and B. Frick. "Crystal field excitations in dilute rare earth noble metal alloys". In: *Physica B: Condensed Matter* 180–181, Part 1 (1992), pp. 176–178. ISSN: 0921-4526. DOI: 10.1016/0921-4526(92)90698-R.

[85] Thomas Herrmannsdörfer, Reinhard König, and Christian Enss. "Properties of Er-doped Au at ultralow temperatures". In: *Physica B: Condensed Matter* 284–288, Part 2 (2000), pp. 1698–1699. DOI: 10.1016/S0921-4526(99)02942-7.

[86] S. Arajs and G.R. Dunmyre. "A search for low-temperature anomalies in the electrical resistivity of dilute gold-erbium alloys". In: *Journal of the Less Common Metals* 10.3 (1966), pp. 220–224. ISSN: 0022-5088. DOI: 10.1016/0022-5088(66)90113-5.

[87] L. Roger Edwards and Sam Legvold. "Electrical Resistivity of Some Dilute Gold-Rare-Earth Alloys". In: *Journal of Applied Physics* 39.7 (1968), pp. 3250–3252. DOI: 10.1063/1.1656764.

[88] L. R. Walker and R. E. Walstedt. "Computer Model of Metallic Spin-Glasses". In: *Physical Review Letters* 38 (9 Feb. 1977), pp. 514–518. DOI: 10.1103/PhysRevLett.38.514.

[89] L. R. Walker and R. E. Walstedt. "Computer model of metallic spin-glasses". In: *Physical Review B* 22 (8 Oct. 1980), pp. 3816–3842. DOI: 10.1103/PhysRevB.22.3816.

[90] C. Enss et al. "Metallic Magnetic Calorimeters for Particle Detection". In: *Journal of Low Temperature Physics* 121.3-4 (2000), pp. 137–176. ISSN: 0022-2291. DOI: 10.1023/A:1004863823166.

[91] S.R. Bandler et al. "Metallic magnetic bolometers for particle detection". In: *Journal of Low Temperature Physics* 93.3-4 (1993), pp. 709–714. ISSN: 0022-2291. DOI: 10.1007/BF00693500.

[92] A. Kozorezov. "Energy Down-Conversion and Thermalization in Metal Absorbers". In: *Journal of Low Temperature Physics* 167.3-4 (2012), pp. 473–484. ISSN: 0022-2291. DOI: 10.1007/s10909-011-0426-1.

[93] C. Pies et al. "maXs: Microcalorimeter Arrays for High-Resolution X-Ray Spectroscopy at GSI/FAIR". In: *Journal of Low Temperature Physics* 167.3-4 (June 2012), pp. 269–279. ISSN: 0022-2291. DOI: 10.1007/s10909-012-0557-z.

[94] Christian Pies. "maXs-200: Entwicklung und Charakterisierung eines Röntgendetektors basierend auf magnetischen Kalorimetern für die hochauflösende Spektroskopie hochgeladener Ionen". ngerman. PhD thesis. Heidelberg University, Nov. 2012.

[95] K. Konzelmann, G. Majer, and A. Seeger. "Solid Effect Between Quadrupolar Transitions in Dilute Cu-Pd Alloys". In: *Zeitschrift für Naturforschung A* 51.5/6 (1996), pp. 506–514.

[96] M. Minier and C. Minier. "Screening charge density around several $\Delta Z = -1$ impurities in copper: Nickel, palladium, platinum, and vacancy". In: *Physical Review B* 22 (1 July 1980), pp. 21–27. DOI: 10.1103/PhysRevB.22.21.

[97] B. Perscheid, H. Büchsler, and M. Forker. "Mössbauer study of the hyperfine interaction of ^{197}Au in gadolinium". In: *Physical Review B* 14 (11 Dec. 1976), pp. 4803–4807. DOI: 10.1103/PhysRevB.14.4803.

[98] Andreas Burck. "Entwicklung großflächiger mikrostrukturierter magnetischer Kalorimeter mit Au:Er- und Ag:Er-Sensoren für den energieaufgelösten Nachweis von Röntgenquanten und hochenergetischen Teilchen". ngerman. PhD thesis. Heidelberg University, 2008.

[99] Talgat Daniyarov. "Metallische magnetische Kalorimeter zum hochauflösenden Nachweis von Röntgenquanten und hochenergetischen Molekülen". ngerman. PhD thesis. Heidelberg University, 2005.

[100] W. Reim et al. “Magnetic Equilibrium Noise in Spin-Glasses: $Eu_{0.4}Sr_{0.6}S$”. In: *Physical Review Letters* 57 (7 Aug. 1986), pp. 905–908. DOI: 10.1103/PhysRevLett.57.905.

[101] P. Svedlindh et al. “Equilibrium magnetic fluctuations of a short-range Ising spin glass”. In: *Physical Review B* 40 (10 Oct. 1989), pp. 7162–7166. DOI: 10.1103/PhysRevB.40.7162.

[102] J. B. Johnson. “Thermal Agitation of Electricity in Conductors”. In: *Physical Review* 32 (1 July 1928), pp. 97–109. DOI: 10.1103/PhysRev.32.97.

[103] H. Nyquist. “Thermal Agitation of Electric Charge in Conductors”. In: *Physical Review* 32 (1 July 1928), pp. 110–113. DOI: 10.1103/PhysRev.32.110.

[104] Valentin Hoffmann. “Messung der AC-Suszeptibilität von paramagnetischem Au:Er bei Temperaturen oberhalb des Spinglas-Übergangs”. ngerman. PhD thesis. Heidelberg University, 2012.

[105] Victoria Wißdorf. “Magnetisches 1/f-Rauschen und Imaginärteil der magnetischen Suszeptibilität von Erbium dotiertem Gold bei Millikelvin Temperaturen”. ngerman. PhD thesis. Heidelberg University, 2013.

Ich versichere, dass ich diese Arbeit selbständig verfasst und keine anderen als die angegeben Quellen und Hilfsmittel benutzt habe.

Heidelberg, den 29.12.2016 .....

(Dorothea Fonnesu)